10GHz Sky Survey to probe Inflation with CMB Polarization

by

Hideki Tanimura

A THESIS SUBMITTED IN PARTIAL FULFILLMENT OF
THE REQUIREMENTS FOR THE DEGREE OF

MASTER OF SCIENCE

in

The Faculty of Graduate Studies

(Astronomy)

THE UNIVERSITY OF BRITISH COLUMBIA

(Vancouver)

April 2013

Abstract

The fluctuations in the cosmic microwave background(CMB) contain a lot of information on the history and composition of our universe. In particular, the rich detail about our early universe is included in the angular power spectra of the CMB fluctuations, which constrains the cosmological parameters in current models of the universe. The latest cosmological data strongly support an inflationary ΛCDM cosmology with a minimal six parameters to describe our universe. The next challenge in cosmology is to probe the physics of the inflationary period by looking for the signature of primordial gravitational waves in the polarized CMB.

CMB polarization was generated at last scattering by scalar and tensor perturbations in the primordial fluid. The tensor perturbations are produced by the stretching of space-time by gravitational wave fluctuations, while scalar perturbations are produced by density fluctuations in the primordial fluid. The ratio of the tensor to scalar perturbation amplitude, r, is a key tracer of the physics of the inflationary epoch, which is deeply connected to the energy scale of inflation in a standard inflationary model.

A local quadrupole anisotropy in the radiation field at the time of decoupling causes the linear polarization in CMB through Thomson scattering by electrons. The linear polarization is described by the Stokes parameters Q and U. While Q and U are orientation dependent and hence produce a rotationally-variant polarization power spectrum, the CMB (Q,U) polarization can be decomposed into two rotationally invariant quantities, called E and B. The E- and B- modes are often described as the curl-free and divergence-free modes of the polarization respectively. The CMB B-mode is a direct tracer of the tensor perturbations caused by gravitational waves in the inflationary period of the universe. Thus, the detection of B-mode has currently been dubbed the "smoking gun" of inflation.

However, the galactic foreground emissions also have E- and B-modes polarization, and are much stronger than the CMB polarization. The dominant source of the polarized emission is galactic synchrotron emission. This emission is generated by high-energy electrons spiraling around the galactic magnetic field lines, and can be up to 75% linearly polarized, but is currently characterized with low signal/noise.

We intend to produce half-sky maps of total intensity and linear polarization at 10 GHz. This data would probe galactic synchrotron emission and also can help constrain the so-called anomalous emission. Therefore, the maps can be used with other surveys such as WMAP and Planck to subtract galactic foreground emissions and obtain more precise CMB data. In addition, the data will give us information about galactic emission components such as synchrotron, free-free, thermal dust and anomalous emission in the microwave range.

Table of Contents

List of Tables

List of Figures

List of Abbreviations

BBN	Big Bang Nucleosynthesis
CMB	cosmic microwave background
Dec	declination
DM	dispersion measure
FOV	field of view
HV	high voltage
ISM	interstellar matter
LSS	last scattering surface
NCP	north celestial pole
PSF	point spread function
R.A.	right Ascension
SHO	simple harmonic oscillator

Acknowledgements

The research topic was completely new for me and in addition, this is my first experience to study abroad. I would like to express my sincere gratitude to my supervisor, Professor. Gary Hinshaw for providing me with this precious research opportunity. I also would like to express my deepest appreciation to him for his elaborated guidance, considerable encouragement and invaluable discussion that makes me understand this challenging topic.

I am also very grateful to all the staff and students who helped my studies at UBC for their valuable cooperation in my studies.

Finally, I would like to extend my indebtedness to my wife, Hitomi, for her endless love, understanding, support, encouragement and sacrifice throughout my study. (Also to my dog, Mameta for his cute face and behavior that always relaxed me so much.)

Chapter 1

Introduction

1.1 Modern cosmology

In the last century, Einstein's theory of General Relativity enabled us to come up with a testable theory of the universe, and Hubble's observation presented the realization that the universe is expanding, and was much hotter and denser. The idea of an expanding universe, called the Big Bang theory, is supported by three observational results: Hubble's observed expansion, light element abundances which implies primodial nucleosynthesis, and the cosmic microwave background left over from 380,000 years after the creation of the universe (S. Dodelson, 2003). The main historical events to verify the Big Bang theory are summaried in Tab. 1.1.

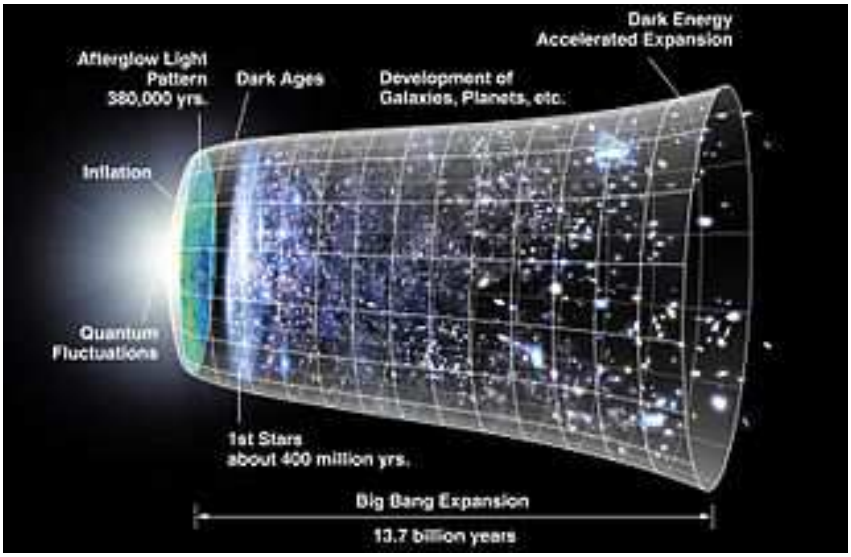

Figure 1.1: Diagram of the Universe's expansion.

1.2 Expanding universe

Modern cosmology is based on the assumption that the universe is homogeneous and isotropic on a large scale, called "Cosmological Principle". A corollary to the cosmological principle is that the laws of physics are universal. The cosmological principle is consistent with the observed isotropy of: (i) the celestial distribution of radio galaxies, which are randomly distributed across the entire sky, (ii) the large scale spatial distribution of galaxies, which form a randomly tangled

1916	General Relativity	Einstein
1922	The expanding universe solution to general relativity	Friedmann
1929	The discovery of Hubble's law	Hubble
1948	The Big Bang theory and Primodial Nucleosynthesis	Gamow, Alpher, Herman
1965	The discovery of Cosmic Microwave Background	Penzias and Wilson
1981	The depelopment of Inflationary theory	Guth, Linde
1992	The discovery of CMB anisotropy by COBE	Smoot, et al.
2003	Establishment of ΛCDM	WMAP Team

Table 1.1: History of Modern Cosmology.

web of clusters and voids up to around 400 Mpcs in width, (iii) the isotropic distribution of observed redshift in the spectra of distant galaxies, which implies an isotropic expansion of space, and (iv) the cosmic microwave background radiation, which is constant in all directions to within 1 part in 10,000.

1.2.1 Friedmann equation

The Friedmann-Robertson-Walker (FRW) metric is an exact solution of Einstein's field equations of General Relativity. It describes a homogeneous and isotropic expanding universe,

$$ds^2 = -c^2dt^2 + a^2(t)\left[\frac{dr^2}{1-Kr^2} + r^2(d\theta^2 + sin^2\theta d\phi^2)\right], \tag{1.1}$$

which implies that physical distances are related to comoving distances with time-dependent scale factor $a(t)$, where K is a constant representing the curvature of the space. The relation between the spacetime geometry and the energy-momentum is described by the Einstein's field equations,

$$R_{\mu\nu} - \frac{1}{2}g_{\mu\nu}R \ \ (+\Lambda g_{\mu\nu}) = 8\pi G T_{\mu\nu}, \tag{1.2}$$

where $G_{\mu\nu}$ is the Einstein tensor; $R_{\mu\nu}$ is the Ricci tensor, which depends on the metric and its derivatives; R is the Ricci tensor; G is Newton's constant; Λ is the cosmological constant; and $T_{\mu\nu}$ is the energy-momentum tensor. By applying Einstein's equations to the FRW metric, the Friedmann equations, which determine the evolution of the scale factor, are derived,

$$\left(\frac{\dot{a}}{a}\right)^2 = \frac{8\pi G}{3}\rho - \frac{K}{a^2} \ \ (+\frac{\Lambda}{3}) \tag{1.3}$$

$$\frac{\ddot{a}}{a} = -\frac{4\pi G}{3}(\rho + 3p) \ \ (+\frac{\Lambda}{3}). \tag{1.4}$$

where ρ is a energy density and p is a pressure. In addition, the energy-momentum convervation law in an expanding universe, $T^{\mu}_{\nu;\mu} = 0$, leads to

$$\dot{\rho} + 3\frac{\dot{a}}{a}(\rho + p) = 0, \tag{1.5}$$

which can also be obtained from the above two equations.

Without cosmological constant, Eq. 1.4 states that both the energy density and the pressure cause a deceleration in the expansion of the universe. However, according to observations, the total matter density is only one third of the critical density and a(t) is accelerating, $\ddot{a} > 0$. Thus, the cosmological constant, which was proposed by Einstein as a modification of his original

theory of general relativity to achieve a stationary universe, has been revived. As in Eq. 1.4 with cosmological constant, the cosmological constant can cause an acceleration in the expansion of the universe. Now, these equations are the basis of the standard big bang cosmological model including the current ΛCDM model.

1.2.2 The Hubble diagram

If the universe is expanding, then the galaxies should be moving away from each other. Therefore, we should see galaxies receding from us and the observed wavelength of light from the receding objects should be stretched. This stretching factor is defined as the redshift z:

$$1 + z = \frac{\lambda_{obs}}{\lambda_{emit}} \tag{1.6}$$

Hubble first found that distant galaxies are in fact receding from us. He also noticed that the velocity increases with distance as in Fig. 1.2. This is exactly what is expected in a homogeneously expanding universe, which is called Hubble's law:

$$v = H_0 d, \tag{1.7}$$

where H_0 is Hubble constant. The Hubble diagram is still the most direct evidence we have that the universe is expanding.

The redshift is derived from the expansion of the universe as follows. The geodesic equation for a light wave in the isotropic universe is given by Eq. 1.1,

$$ds^2 = -c^2 dt^2 + \frac{a^2(t) dr^2}{1 - Kr^2}. \tag{1.8}$$

Integrating over the path in both space and time that the light wave travels yields

$$\int \frac{cdt}{a(t)} = \int \frac{dr}{\sqrt{1 - Kr^2}}. \tag{1.9}$$

Suppose a crest of the light wave was emitted at t=t_1 in the past and the subsequence crest was emitted at t=$t_1 + \delta t_1$, and for an observer, the first crest was observed at t=t_0 and the subsequence crest was observed at t=$t_0 + \delta t_0$. Then, since the both crests travel through the same co-moving distance,

$$\int_{t_1}^{t_0} \frac{cdt}{a(t)} = \int_{t_1+\delta t_1}^{t_0+\delta t_0} \frac{cdt}{a(t)}. \tag{1.10}$$

Over the period of a light wave, the scale factor is essentially constant. This yields

$$\frac{\delta t_1}{a(t_1)} = \frac{\delta t_0}{a(t_0)}. \tag{1.11}$$

The wavelength at the light source and observer are given by $\lambda_1 = c\delta t_1$ and $\lambda_0 = c\delta t_0$, and the definition of the redshift is given by Eq. 1.6. Therefore, as $a(t_0) = 1$, the redshift is obtained as

$$1 + z = \frac{\lambda_0}{\lambda_1} = \frac{1}{a(t_1)}, \tag{1.12}$$

which is called "cosmological redshift". It means that the wavelength emitted at the time with the scale factor, $a(t)$, is stretched by the expansion of the space with the rate, $1/a(t)$ ($a(t) \leq 1$).

The Hubble diagram is obtained by finding the distance and the redshift of distant objects. Redshifts are obtained by observations directly, but distances are difficult. One of the most useful techniques to measure distances is to find a standard candle such as cepheid variables. As

shown in Fig. 1.2, the standard candle that is seen at largest distances is Type Ia supernovae. They can be used to extend the Hubble diagram out to very large redshifts, $z \sim 1.7$. Fig. 1.2 shows that five distance indicators agrees with one another and have converged on $H_0 = 72$ km/sec/Mpc with 5 % errors.

Fig. 1.3 is a recent Hubble diagram using distant Type Ia supernovae. The three curves depict three different possibilities: flat matter dominated; open; and flat with a cosmological constant. The high-redshift data favor a Λ-dominated universe over a matter-dominated one.

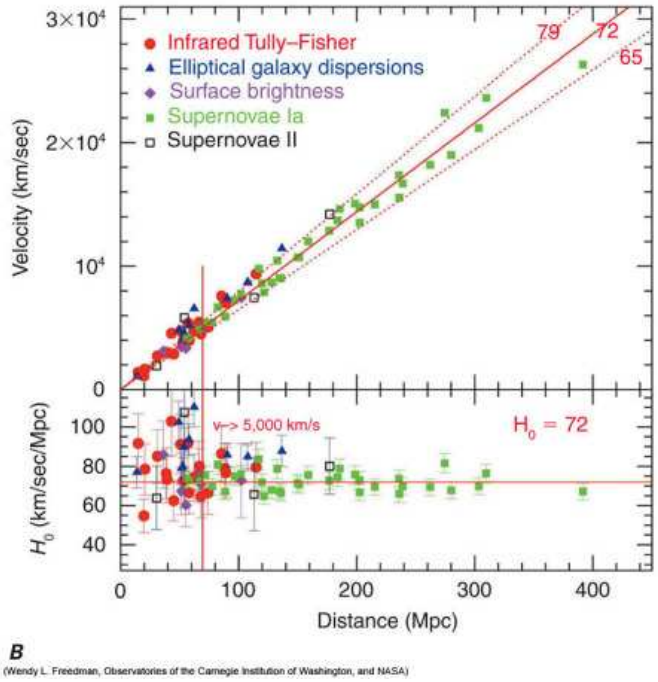

Figure 1.2: Hubble diagram from the Hubble Space Telescope Key Project based on (Freedman et al., 2001), using five different measures of distance. Bottom panel shows H_0 vs distance with the horizontal line equal to the best fit value of 72 km/s/Mpc.

1.2.3 Big Bang Nucleosynthesis

The Universe's light-element abundance is another important criterion to verify the Big Bang hypothesis. It is now considered that the elements observed in the Universe were created in either of two ways. Light elements (deuterium, helium, and lithium) were produced in the first few minutes of the Big Bang, while elements heavier than helium were produced in the interiors of stars which formed much later in the history of the Universe.

In the 1950's and 60's, it was recognized that all the heavier elements were produced either in stellar interiors or during supernova explosions. However, it was observed that almost 25% of the total matter in mass density in the universe consists of helium, and the amount was much larger than predicted by the stellar theory. A similar enigma existed for deuterium. According to the stellar theory, deuterium cannot be produced in stellar interiors; on the contrary, deuterium is destroyed inside of stars. George Gamow and his collaborators suggested the theory as to the production of light elements in the early Universe, called Big Bang Nucleosynthesis (BBN).

According to BBN, when the universe was much hotter and denser at the temperature of order an MeV/k_B, there were no neutral atoms or even bound nuclei. Any atom or nucleus produced would be immediately destroyed by vast amounts of high energy photons in such a

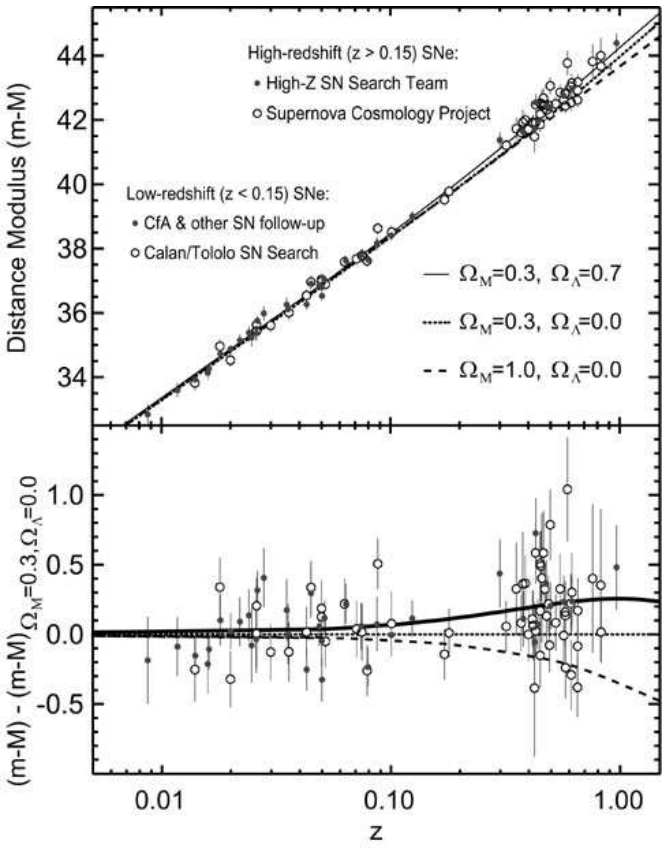

Figure 1.3: Hubble diagram from distant Type Ia supernovae (Perlmutter & Schmidt, 2003). Top panel: The Hubble diagram for high redshift SNIa from both the HZSNS (Riess et al., 1998) and the SCP (Perlmutter et al., 1999). The z < 0.15 objects for both teams are drawn from CTSS sample (Hamuy et al., 1995), so many of these objects are in common between the analyses of the two teams. It shows apparent magnitude(an indicator of the distance) vs redshift. Lines show the predictions for different energy contents in the universe, with Ω_M the ratio of energy density today in matter compared to the critical density and Ω_Λ the radio of energy density in a cosmological constant to the critical density. Bottom panel: The residual of the distances relative to a $\Omega_M = 0.3$, $\Omega_\Lambda = 0.0$ Universe. The high-redshift supernovae favor a Λ-dominated universe over a matter-dominated one.

hot environment. As the universe cooled well below the binding energies of typical nuclei, light elements began to form. Big Bang Nucleosynthesis theory predicts that roughly 25% of the matter in mass density consists of Helium, which is consistent with the observational result. It also predicts about 0.01% deuterium, and even smaller quantities of lithium. Fig. 1.4 shows the evolution of each light element with the number density of baryon/photon, $\eta = 5.1 \times 10^{-10}$.

Fig. 1.5 shows the predictions of BBN for the light element abundances and constraints on the baryon density from BBN. The theoretical predictions depend on the density of baryons at the time of nucleosynthesis, therefore, give us a way to measure the baryon density in the universe. In particular, the measurement of primordial deuterium constraints the baryon density. That result is consistent with later CMB estimates of the baryon density, although the primordial abundance of ^{7}Li inferred from observations is significantly below its expected value. Fig. 1.5 also indicates that baryons contribute only $\sim$4 % of the critical density (with h = 0.7). Since the total matter density today is estimated to about 25 %, nucleosynthesis provides a strong support for the existence of nonbaryonic dark matter.

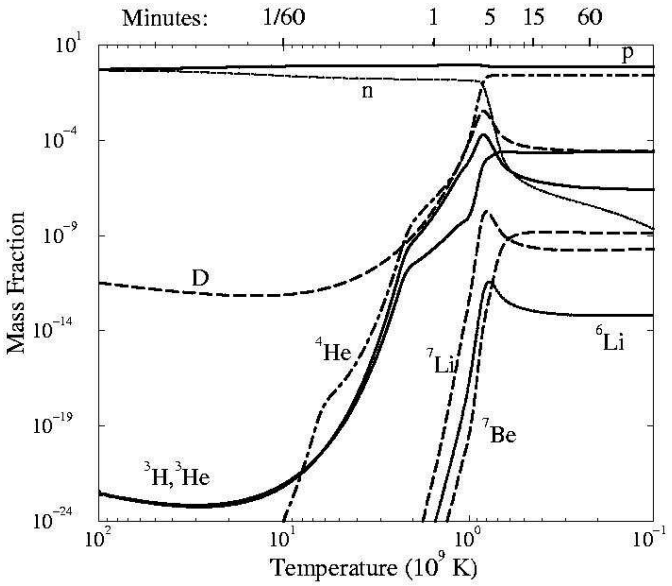

Figure 1.4: Mass fraction of nuclei as a function of temperature and time for $\eta = 5.1 \times 10^{-10}$ (Burles & Nollett & Turner, 1999).

1.2.4 Cosmic Microwave Background

The discovery of the cosmic microwave background (CMB) is a powerful test of the Big Bang theory. In the Big Bang model, the early universe was made up of a hot and interacting plasma of photons, electrons, and baryons. As the universe expanded, adiabatic cooling caused the plasma to lose energy until it became favorable for electrons to combine with protons, forming neutral hydrogen atoms. This recombination event happened when the temperature was around 3000 K and when the universe was approximately 380,000 years old. At this point, the photons no longer interacted with the electrically neutral atoms and began to travel freely through space, resulting in the decoupling of matter and radiation. The radiation coming from a spherical surface called the surface of last scattering is called "cosmic microwave background radiation". The temperature of the decoupled photons has continued to diminish ever since, because of the expansion of the universe; now down to 2.72548 ± 0.00057 (Fixsen et al., 2009). Two of the greatest successes of the Big Bang theory are its prediction of the almost perfect black body spectrum (Fig. 1.6) and its detailed prediction of the anisotropies in the cosmic microwave background (Fig. 1.7).

But, anisotropy requires a source of fluctuations. Temperature anisotropy in the CMB was first detected by COBE, then more precisely by WMAP (Fig. 1.8) and numerous other experiments. These are believed to result from inhomogeneities in the distribution of matter at the epoch of recombination, and seed the formation of galaxies and clusters. The discovery provides evidence that such density inhomogeneities existed in the early universe, perhaps caused by quantum fluctuations in the scalar field of inflation or by topological defects resulting from a phase transition (Kamionkowski & Kosowsky et al., 1999). It is now considered that gravitational collapse of these primordial density inhomogeneities formed the large-scale structures of galaxies, clusters, and superclusters.

The WMAP mission, with an angular resolution of less than 0.25 degs, measured CMB anisotropies on smaller angular scales (Fig. 1.8), while COBE, with an angular resolution of 7 degs, was sensitive only to broad fluctuations of large size. In the WMAP measurement, several acoustic peaks which COBE did not have sufficient resolution to resolve were detected (Fig. 1.9).

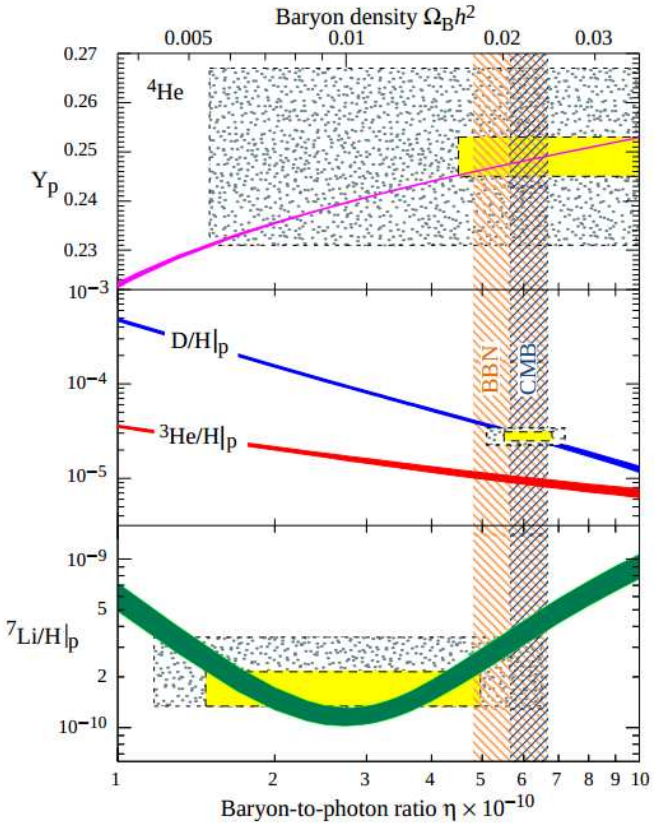

Figure 1.5: Constraints on the baryon density from Big Bang Nucleosynthesis (Sarkar et al., 2006). The abundances of ^{4}He, D, ^{3}He and ^{7}Li as predicted by the standard model of big-bang nucleosynthesis. Boxes indicate the observed light element abundances (smaller boxes: 2σ statistical errors; larger boxes: $\pm 2\sigma$ statistical and systematic errors). The narrow vertical band indicates the CMB measure of the cosmic baryon density by WMAP.

The acoustic oscillations arise because of a competition in the photon-baryon plasma in the early universe. The pressure of the photons tends to erase anisotropies, whereas the gravitational attraction of the baryons and dark matter moving at speeds much slower than light makes them tend to collapse to form dense halo. These two effects compete to create acoustic oscillations which give the microwave background its characteristic peak structure. The peaks correspond to resonances in which the photons decouple when a particular mode is at its peak amplitude.

The peaks contain interesting physical signatures as in Fig. 1.10. The angular scale of the first peak probes the curvature of the universe. The WMAP results demonstrate that the geometry of the Universe is approximately flat, rather than curved. The ratio of the odd peaks to the even peaks determines the baryon density. The third peak can be used to get information about the dark matter density. The best-fit ΛCDM parameters are summarized in Tab. 1.2.

The tail of the power spectrum gives additional infomation about the last scattering surface (LSS). Collisionless damping is caused by two effects, (i) the increasing mean free path of the photons as the primordial plasma becomes increasingly rarefied in an expanding universe (ii) the finite depth of the last scattering surface, which causes the mean free path to increase rapidly during decoupling, even while some compton scattering is still occurring. These effects contribute about equally to the suppression of anisotropies at small scales, and give rise to the characteristic exponential damping tail seen in the very small angular scale anisotropies. The thickness of the LSS refers to the fact that the decoupling of the photons and baryons does

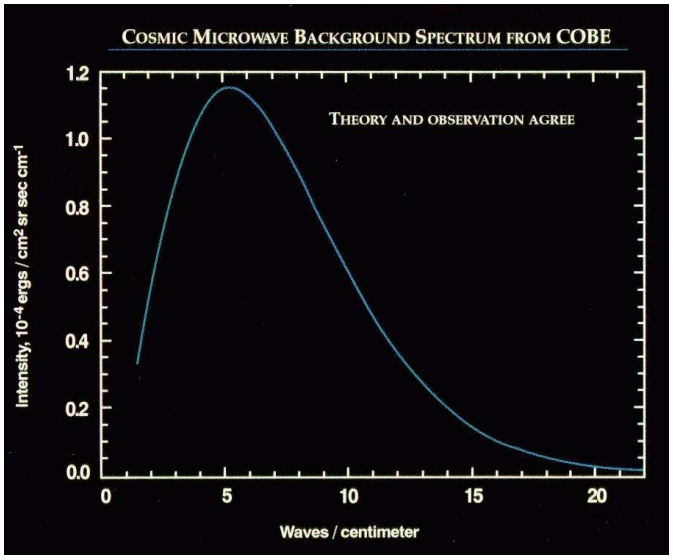

Figure 1.6: CMB Spectrum (Mather et al., 1994). The FIRAS instrument aboard COBE measured the spectrum of the CMB precisely, and found a blackbody spectrum with deviations limited to 50 ppm of the peak brightness, with a peak wavelength of 1.869 mm, corresponding to a temperature of T = 2.725 ± 0.002 K.

not happen instantaneously. The WMAP team found that decoupling took place over roughly 101,000 years (Hinshaw et al., 2012), and when it was complete, the universe was roughly 489,000 years old.

The shape of the peaks gives important information about the nature of the primordial density perturbations (Fig. 1.11). There are two fundamental types of density perturbations called adiabatic and isocurvature. Adiabatic density perturbations have the same fractional overdensity in each matter component (baryons, photons ...). With isocurvature density perturbations, the sum of the fractional overdensities is zero. Cosmic inflation predicts that the primordial perturbations are adiabatic. The CMB spectrum is able to distinguish these two from the width of the peaks in the power spectrum. Isocurvature density perturbations produce a series of peaks whose angular scales are roughly in the ratio 1:3:5:..., while adiabatic density perturbations produce peaks whose locations are in the ratio 1:2:3:... Observations are consistent with the primordial density perturbations being entirely adiabatic, providing key support for inflation.

1.3 Problems in Big Bang Cosmology

The hot Big Bang model has been very successful in predicting many phenomena observed in the universe today. The model successfully accounts for nucleosynthesis and the relative abundance of the light elements. The prediction of the cosmic microwave background radiation and the fact that the universe is expanding (i.e., The Hubble Law), both represent successful predictions of the Big Bang theory. However, this model raises new questions which it can not answer.

1.3.1 Three puzzles in Big Bang Cosmology

- Horizon Problem: Why is the universe so homogeneous and isotropic on large scales? The CMB, which fills the universe, is almost precisely the same temperature everywhere in the sky about 2.725 K. Yet, there was not enough time in the past for the photons to communicate their temperature to opposite sides of the visible universe and reach to

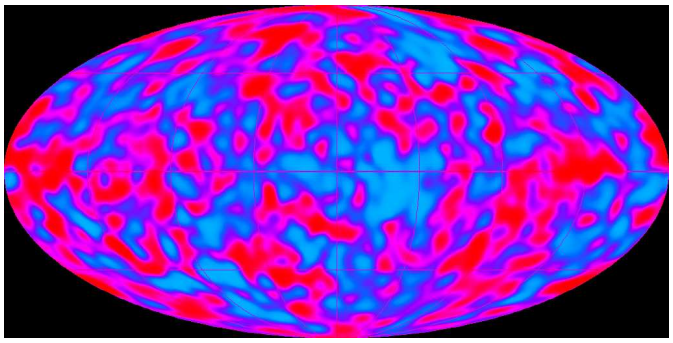

Figure 1.7: CMB fluctuation map made by the DMR instrument aboard COBE (LAMBDA). CMB fluctuations are extremely faint, only one part in 100,000 compared to the mean CMB temperature 2.73 K.

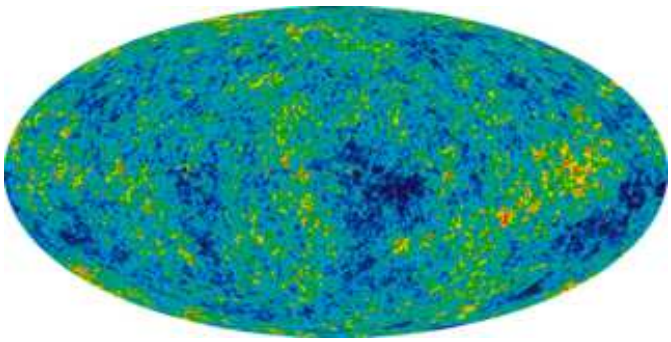

Figure 1.8: Nine year WMAP image of the CMB temperature anisotropy (LAMBDA).

thermal equilibrium. In fact, any region separated by more than 2 degrees in the sky today would have been causally disconnected at the time of decoupling in the standard model.

- Flatness Problem: The second problem is that of the Universe's peculiar spacetime geometry. WMAP has provided data that implies that the universe is geometrically nearly flat. This would seem to be in contradiction with Big Bang cosmology, which indicates that the curvature of spacetime grows with time. The flat geometry implies that the universe's critical density is at the point between eternal expansion and eventual collapse. The probability of such a situation, being at that very small point between the two alternative futures of the universe, is highly unlikely. A universe as flat as we see it today would require an extreme fine-tuning of conditions in the past. The traditional Big Bang Theory does not provide an explanation for this critically exact balance.

- Monopole Problem: At early times in the expansion ($z > 1000$), the physics of the universe is described by high energy particle theory (Watson et al., 2000). Many of these theories predict the creation of topological defects such as domain walls, strings, monopoles and textures. These defects arise when phase transitions occur in particle models. Of all these defects, monopoles are the most prevalent in particle theories. It becomes a problem in the hot Big Bang model, when one calculates the number of monopoles produced in events, such as the electroweak symmetry breaking. One finds they would be the dominant matter in the universe, but no monopole has ever been observed, directly or indirectly.

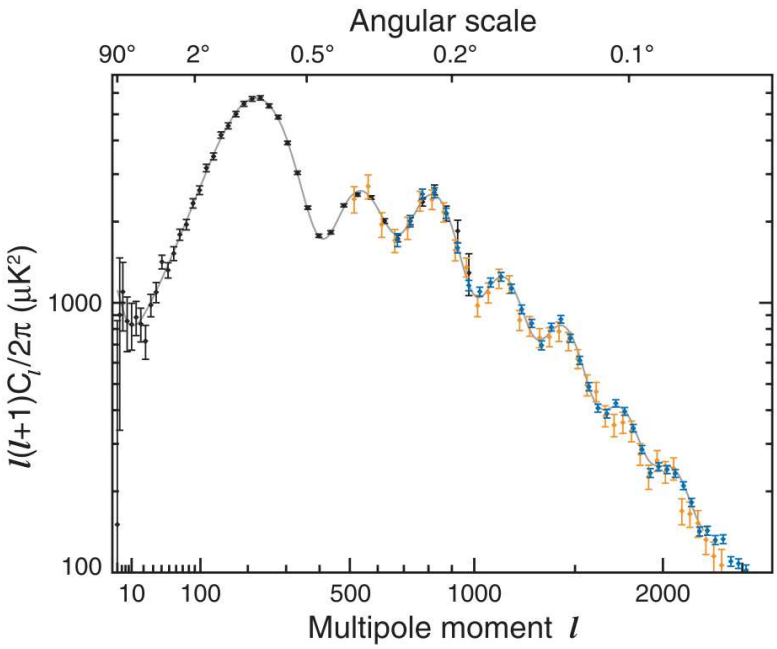

Figure 1.9: The CMB power spectrum from the WMAP (2012) in black, SPT (2011) in blue, and ACT (2011) in orange. WMAP data alone (shown in grey) is extended to the higher-resolution data (Hinshaw et al., 2012).

1.3.2 Inflation theory

Inflation Theory, developed by Alan Guth, Andrei Linde, Paul Steinhardt, and Andy Albrecht, offers solutions to these problems and several other open questions in cosmology (Guth et al., 1981). It proposes a period of exponential expansion of the universe prior to the more gradual Big Bang expansion, during which time the energy density of the universe was dominated by a cosmological constant-type of vacuum energy that later decayed to produce the matter and radiation that fills the universe today.

Inflation was both rapid and strong. It increased the linear size of the universe by more than 60 "e-folds", or a factor of $\sim 10^{26}$ in only a small fraction of a second. Inflation is now considered an extension of the Big Bang theory since it explains the above puzzles so well, while retaining the basic paradigm of a homogeneous expanding universe.

- Solution to the Horizon Problem: Since Inflation supposes a burst of exponential expansion in the early universe, it follows that distant regions were actually much closer together prior to Inflation than they would have been with only standard Big Bang expansion. Thus, such regions could have been in causal contact prior to inflation and could have attained a uniform temperature.

- Solution to the Flatness Problem: Inflation and its subsequent expansion has essentially expanded the curvature of the universe to every large radius. Just as the world appears flat to a casual observer on the surface of the ocean, for example, so does that vast extent of the possible-curved universe appear flat.

- Solution to the Monopole Problem: Inflation allows for magnetic monopoles to exist as long as they were produced prior to the period of inflation. During inflation, the density of monopoles drops exponentially, so their abundance drops to undetectable levels.

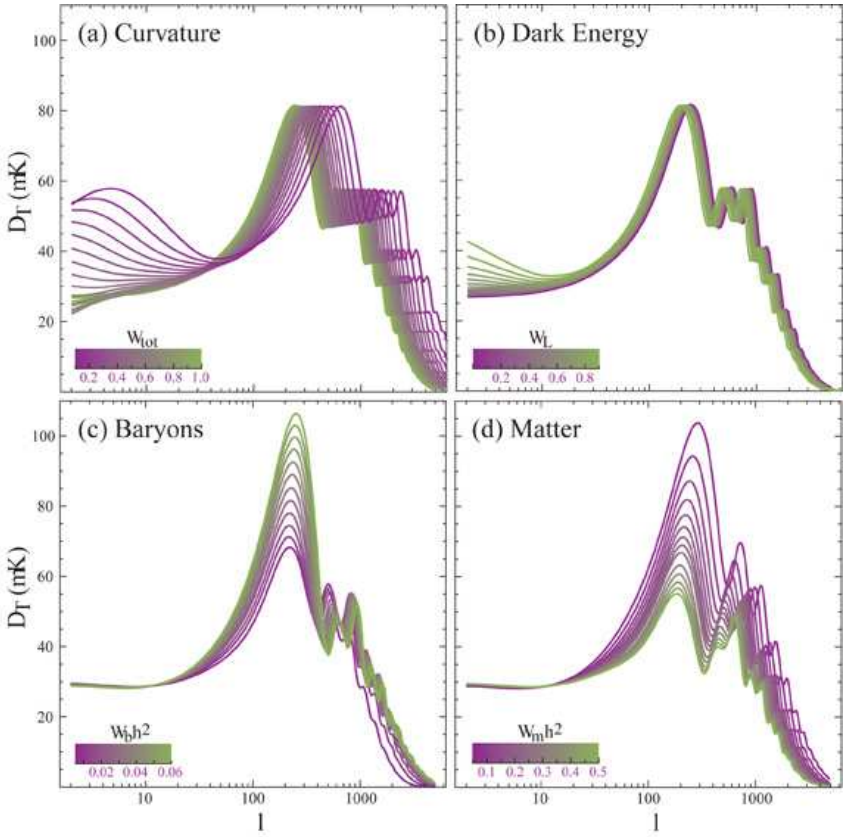

Figure 1.10: Sensitivity of the acoustic temperature spectrum to four fundamental cosmological parameters (a) the curvature as quantified by $\Omega_{\rm tot}$ (b) the dark energy as quantified by the cosmological constant Ω_Λ (w_Λ = -1) (c) the physical baryon density $\Omega_{\rm b}\ h^2$ (d) the physical matter density $\Omega_{\rm m}\ h^2$, all varied around a fiducial model of $\Omega_{\rm tot} = 1$, $\Omega_\Lambda = 0.65$, $\Omega_{\rm b}\ h^2 = 0.02$, $\Omega_{\rm m}\ h^2 = 0.147$, $n_s = 1$ (scalar spectral index), $Z_{ri} = 0$ (redshift at reionization), $E_i = 0$. (energy scale at inflation) (Hu & Dodelson et al., 2002)

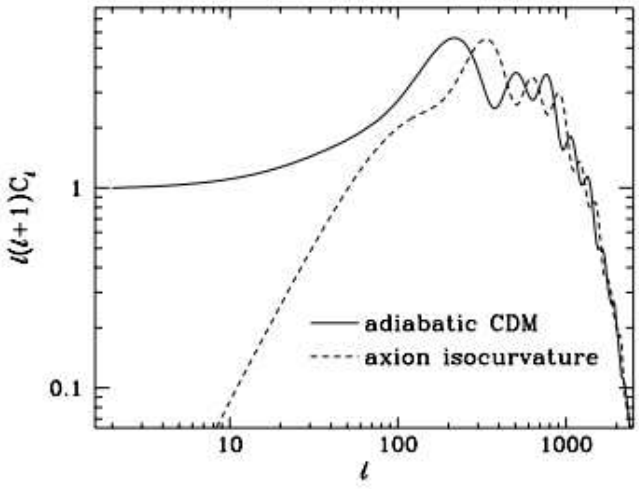

Figure 1.11: Diffusion damping in case of adiabatic and isocurvature (Hu et al., 1996).

Label	Definition	Value
$\Omega_{\rm b}$	Baryon Fraction	0.04628 ± 0.00093
$\Omega_{\rm CDM}$	Dark Matter Fraction	0.2402 ± 0.0088
Ω_Λ	Cosmological Constant	0.7135 ± 0.0095
t_0 (Gyr)	Age of Universe	13.772 ± 0.059
H_0 (km/s/Mpc)	Hubble Constant	69.32 ± 0.80
z_{eq}	Radiation to Matter Time	3293 ± 47
z_{reion}	Reionization Period	10.1 ± 1.0
τ	Optical Depth	0.081 ± 0.012
$10^9\Delta^2_R$	Scalar Amplitude	2.464 ± 0.072
n_s	Scalar Index	0.9608 ± 0.0080

Table 1.2: The current ΛCDM cosmological parameters obtained by fitting WMAP plus External Data including eCMB(ACT and SPT), BAO(6dFGRS, SDSS and WiggleZ) and H_0(HST and WFPC2) (Hinshaw et al., 2012)

Inflation also explains the origin of structure in the universe. Prior to inflation, the portion of the universe we can observe today was microscopic, and quantum fluctuation in the density of matter on these microscopic scales expanded to astronomical scales during inflation. Over the next several hundred million years, the higher density regions condensed into stars, galaxies, and clusters of galaxies.

Inflation explains a lot of features of the universe in a simple way with relatively few assumptions, and it seems to arise naturally in the context of our current theories of physics. Nonetheless, one of the most severe challenges for inflation arises from the need to fine-tune the theory.

The inflationary proposal requires a huge extrapolation of the known laws of physics. In the absence of a complete theory, a phenomenological approach has been commonly employed, where an effective potential $V(\phi)$ is postulated. The simplest inflationary scenarios consist of a single light scalar field with a canonical kinetic term, $(\nabla\phi)^2/2$, in its action. They predict the following observable characteristics.

1. Flat geometry, - the observable universe should have no spatial curvature. As we have seen, flatness has been verified at the 1% level by the location, or, better, separation, of the CMB acoustic peaks combined with some low-redshift distance information.

2. Gaussianity, - the primordial perturbations should be described by Gaussian random fields to a very high precision.

3. Scale-invariance, - to a first approximation, there should be equal power at all length-scales in the perturbation spectrum, without being skewed towards high or low wavenumbers. In terms of the parameterisation above, this corresponds to $n_s = 1$ and $n_t = 0$. However, small deviations from scale-invariance are also a typical signature of inflationary models and tell us about the dynamics of inflation.

4. Adiabaticity, - after reheating, there are no perturbations in the relative number densities of different species on super-Hubble scales (no isocurvature modes). This follows if only a single field is important during inflation.

5. Super-Hubble fluctuations, - there exist correlations between anisotropies on scales larger than the apparent causal horizon, beyond which two points could not have exchanged infor-

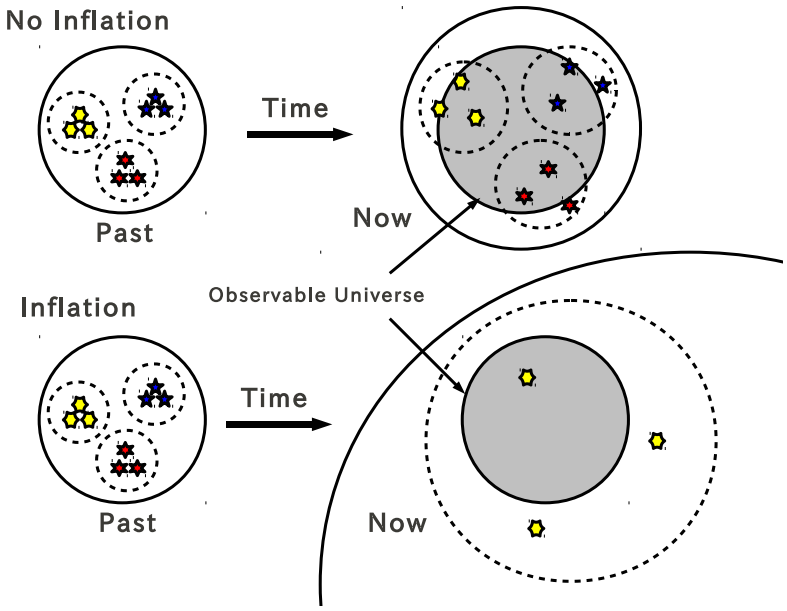

Figure 1.12: Solution to the Horizon Problem.

mation at light-speed during the history of a non-inflationary universe. This corresponds to angular separations on the sky larger than $\sim 2^{\circ}$.

6. Primordial gravitational waves, - these fluctuations also give rise to temperature and polarization anisotropies in the CMB. Tensor modes must exist; however, their predicted amplitude can vary by many orders of magnitude depending on the underlying microphysical mechanism implementing inflation.

The list 1 to 5 of the above have been tested to some degree, but the list 6 still awaits for better data. Many models of inflation have been suggested such as slow-roll inflation, hybrid inflation and eternal inflation. Which model survives or not should be verified by observations. The key is a detection of primodial B-mode polarization in CMB, which would demonstrate the energy scale of inflation. Therefore, the detection of B-mode polarization is an outstanding experimental challenge, and represents a key goal for current and future CMB experiments such as ground-based (BICEP-II, QUIJOTE, PolarBear, QUIET), balloon-borne (EBEX, Spider, PIPER) and satellite (Planck, B-Pol, litebird, CMBPol) experiments.

Chapter 2

Probing Inflation with CMB Polarization

Currently the best theory we have about the earliest moment in the history of the universe is called "Inflation". A tiny fraction of a second after the Big Bang, the universe seems to have expanded exponentially during a period of accelerated expansion. This scenario explains several important observations about flatness, isotropy and homogenity of the universe. Even though inflation conveniently explains these mysteries, we have no direct evidence that inflation really happened.

The accelarated expansion of space during inflation would have created ripples in the fabric of space: gravity waves. These gravity waves should have left a signature in the polarization of the last-scattered photons, which is called B-mode polarization. Therefore, the search for the primordial B-mode signature of inflation is often considered the "holy grail" of observational cosmology. In this chapter, we shall discuss the physics of inflation and its predicted signature in the polarization in CMB.

2.1 Inflationary cosmology

2.1.1 Solution to the horizon problem

The comoving horizon is the total portion of the universe visible to the observer, representing the sphere with radius equal to the distance the light could have traveled since the Big Bang. The comoving horizon is defined as

$$\eta = \int_0^a \frac{da'}{a'} \frac{1}{a'H(a')}, \tag{2.1}$$

where $1/aH$ is the comoving Hubble radius.

How much inflation is required to solve the horizon problem? Most inflationary models typically assume energy scales of order 10^{15} GeV or larger. An order of magnitude can be estimated by ignoring the relatively brief epoch of recent matter domination and assuming that the universe has been radiation dominated since the end of inflation. H scales as a^{-2} ($a(t) \propto t^{1/2}$) in the radiation epoch, then

$$\frac{a_0 H_0}{a_e H_e} \simeq a_e \simeq \frac{T_0}{10^{15} GeV} \simeq 10^{-28}, \tag{2.2}$$

where a_e is the scale factor at the end of inflation. This estimate implies that the comoving Hubble radius at the end of inflation was roughly 28 orders of magnitude smaller than it is today. For inflation to be valid, the comoving Hubble radius at the onset of inflation had to be

larger than the current comoving Hubble radius. It follows that during inflation, the comoving Hubble radius had to decrease by 28 orders of magnitude, as in Fig. 2.1.

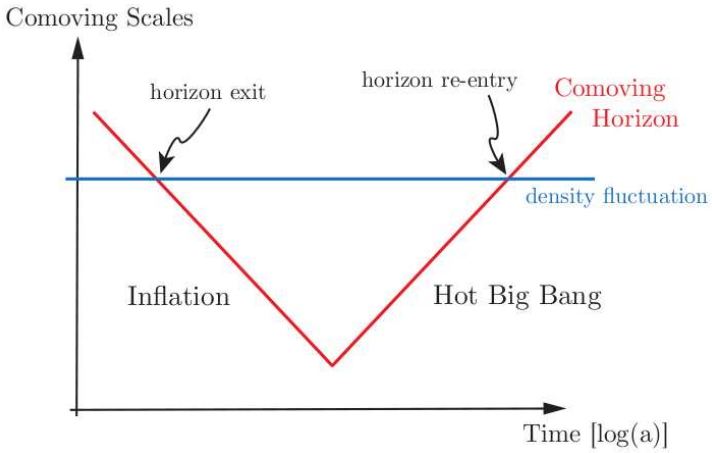

Figure 2.1: Creation and evolution of perturbations in the inflationary universe. Fluctuations are created quantum mechanically on sub-horizon scales. While comoving scales, k^{-1}, remain constant, the comoving Hubble radius during infation, $(aH)^{-1}$, shrinks and the perturbations exit the horizon. Causal physics cannot act on superhorizon perturbations and they freeze until horizon re-entry at late times (Baumann et al., 2009).

The most common way to arrange this is to construct a model where H is constant during inflation. In this case, the scaler factor evolves

$$a(t) = a_e \mathrm{e}^{H(t-t_e)}, \tag{2.3}$$

where t_e is the time at the end of inflation. The decrease in the comoving Hubble radius is due to the exponential increase in the scale factor. For the scale factor to increase by a factor of 10^{28}, the augment of the exponential must be of order $\ln(10^{28}) \sim 64$. Inflation can solve the horizon problem if the universe expands exponentially for more than 60 e-folds.

2.1.2 Negative pressure

The horizon problem can be solved by inflation, the acceleration of the universe. Based on General Relativity, the expansion of the universe is related to the stress-energy in it. What type of energy can produce the acceleration? The Einstein equations in a flat space give us

$$\left(\frac{da/dt}{a}\right)^2 = \frac{8\pi G}{3}\rho, \tag{2.4}$$

$$\frac{d^2a/dt^2}{a} + \frac{1}{2}\left(\frac{da/dt}{a}\right)^2 = -4\pi G P. \tag{2.5}$$

These two equations can be summarized as

$$\frac{d^2a/dt^2}{a} = -\frac{4\pi G}{3}(\rho + 3P) \tag{2.6}$$

For the acceleration to happen, the term in parentheses on the right must be negative, so inflation requires

$$P < -\frac{\rho}{3}. \tag{2.7}$$

Since the energy density is always positive, the pressure must be negative. It implies that inflation is not driven by ordinary matter or radiation.

2.1.3 Scalar field in cosmology

To turn on inflation, material with the unusual property of negative pressure is necessary. Such a material is a scalar field, describing scalar, spin-0, particles. Here, we will discuss inflation in terms of the scalar field.

The energy-momentum tensor for the field(ϕ) is given by

$$T^{\alpha}_{\ \beta} = g^{\mu\nu}\frac{\partial\phi}{\partial x^{\nu}}\frac{\partial\phi}{\partial x^{\beta}} - g^{\alpha}_{\ \beta}\left[\frac{1}{2}g^{\mu\nu}\frac{\partial\phi}{\partial x^{\mu}}\frac{\partial\phi}{\partial x^{\nu}} + V(\phi)\right], \tag{2.8}$$

where $V(\phi)$ is the potential of the field. We assume the energy density, ρ, is mostly homogeneous, then the field is described as

$$\phi(\vec{x},t) = \phi^{(0)}(t) + \delta\phi(\vec{x},t), \tag{2.9}$$

where $\phi^{(0)}(t)$ is a zero-order and $\delta\phi(\vec{x},t)$ is a first-order pertubation, which comes from quantum fluctuations. For the homogeneous part of the field, only time derivatives of ϕ are relevant. Then, in the zero-order part, the time-time component of T^0_0 is equal to $-\rho$, so the energy density is expressed as

$$\rho = \frac{1}{2}\left(\frac{d\phi^{(0)}}{dt}\right)^2 + V(\phi^{(0)}), \tag{2.10}$$

and the space-space component is equal to P, so the pressure is given by

$$P = \frac{1}{2}\left(\frac{d\phi^{(0)}}{dt}\right)^2 - V(\phi^{(0)}). \tag{2.11}$$

In Eq. 2.10 and Eq. 2.11, the first term of the right-hand side corresponds to the kinetic energy density of the field and the second does its potential energy density. For the pressure to be negative, the potential energy has to be larger than the kinetic energy. One example of the scalar field is Fig. 2.2, called slow-roll inflation. In this model, the potential energy is almost constant during inflation and the kinetic energy, $\dot{\phi^{(0)}}$, is almost zero, which results in the negative pressure in Eq. 2.11. This situation also leads to almost constant energy density in Eq. 2.10, then Einstein's equation for the evolution of the scalar factor becomes

$$\frac{da/dt}{a} = \sqrt{\frac{8\pi G\rho}{3}} \sim constant, \tag{2.12}$$

which naturally produces an exponential expansion as in Eq. 2.3.

To determine the evolution of $\phi^{(0)}$ when the field is not trapped, we return to the Einstein equations, Eq. 2.4 and Eq. 2.5. If the dominant component in the universe is ϕ, then the energy density on the right-hand side becomes $(d\phi^{(0)}/dt)^2 + V$. Differentiating the equation leads to the evolution equation for a homogeneous scalar field in an expanding universe,

$$\frac{d^2\phi^{(0)}}{dt^2} + 3H\frac{d\phi^{(0)}}{dt} + \frac{dV}{d\phi} = 0. \tag{2.13}$$

2.1.4 Slow-roll Inflation

Most models of inflation are slow-roll models, in which the zero-order field, and hence the Hubble rate, vary slowly. First, we will rearrange Eq. 2.10 and Eq. 2.11 into

$$H^2 = \frac{1}{3M_{pl}^2}\left(\frac{1}{2}(\dot{\phi}^{(0)})^2 + V(\phi^{(0)})\right) \tag{2.14}$$

$$\frac{\ddot{a}}{a} = -\frac{1}{3M_{pl}^2}\left((\dot{\phi}^{(0)})^2 - V(\phi^{(0)})\right) \tag{2.15}$$

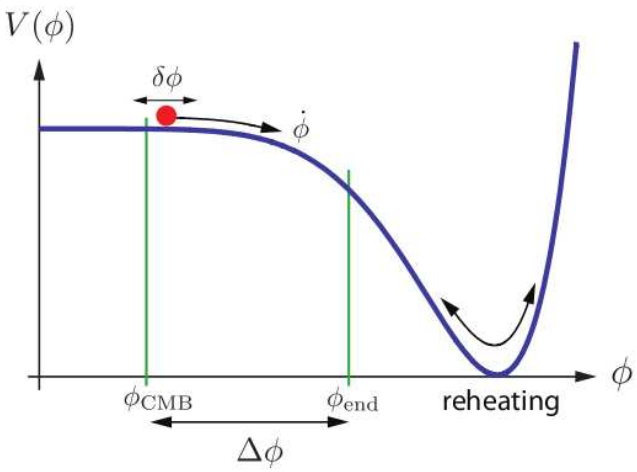

Figure 2.2: Scalar field potential of slow-roll inflation. The expansion happens when the field potential $V(\phi^{(0)})$ dominates over its kinetic energy $(1/2)(\dot{\phi^{(0)}})^2$. The primordial perturbation $\delta\phi(\vec{x},t)$ is created by quantum fluctuations. After the end of inflation, reheating occurs, which makes the universe hot (Baumann et al., 2009).

where M_{pl} is the Planck mass, $M_{pl} = (8\pi G)^{-1/2} = 2.436 \times 10^{18}$ GeV.

The standard approximation technique for analyzing inflation is the slow-roll approximation. During slow-roll, the potential energy of the field dominates over the kinetic energy. This approximation throws away $\ddot{\phi}$ and $(\dot{\phi}^{(0)})^2$, leaving

$$H^2 \simeq \frac{V(\phi^{(0)})}{3M_{pl}^2} \tag{2.16}$$

$$3H\dot{\phi}^{(0)} \simeq -V'(\phi^{(0)}) \tag{2.17}$$

For this appoximation to be valid, it is necessary for two conditions to be held,

$$\epsilon(\phi^{(0)}) << 1, \qquad |\eta(\phi^{(0)})| << 1, \tag{2.18}$$

where the slow-roll parameters ϵ and η are defined as

$$\epsilon \equiv \frac{\dot{H}}{H^2} = 4\pi G\frac{\dot{\phi}^2}{H^2} \simeq \frac{M_{pl}^2}{2}\frac{V'}{V}, \qquad |\eta| \simeq M_{pl}^2\left|\frac{V''}{V}\right|. \tag{2.19}$$

Once these constraints are satisfied, the inflationary process happens generally for a wide class of models.

2.1.5 Tensor perturbations

Scalar perturbations couple to the density of matter and radiation, and they are responsible for most of the inhomogeneities and anisotropies in the universe. In addition to the scalar perturbations, inflation also generates tensor perturbations in the gravitational metric, so-called gravity waves. During inflation, the universe primarily consists of a uniform scalar field and a uniform background metric. Against the background, the field fluctuate quantum mechanically. The quantum mechanical fluctuations during inflation are responsible for the variations around the smooth background. These are not coupled to the density and so are not responsible for the large-scale structure of the universe, but they induce fluctuations in the CMB.

The 'simple' way to calculate the quantum fluctuations in the metric is to quantize the field with an analogy to a simple harmonic oscillator(SHO). The simple harmonic oscillator with unit mass and frequency ω is governed by the equation

$$\frac{d^2x}{dt^2} + \omega^2 x = 0. \tag{2.20}$$

Upon the quantization, x becomes a quantum operator

$$\hat{x} = v(\omega, t)\hat{a} + v^*(\omega, t)\hat{a}^\dagger, \tag{2.21}$$

where $\hat{a}$ is a quantum operator and v is a solution to Eq. 2.20, $v \propto \mathrm{e}^{-i\omega t}$. The operator $\hat{a}$ annihilates the vacuum state, $\hat{a}|0>= 0$, in which there are no particles, and also satisfies the commutation relation

$$[\hat{a}, \hat{a}^\dagger] \equiv \hat{a}\hat{a}^\dagger - \hat{a}^\dagger\hat{a} = 1, \tag{2.22}$$

which gives the variance

$$\langle|\hat{x}^2|\rangle \equiv \hat{x}^\dagger\hat{x} = |v(\omega, t)|^2. \tag{2.23}$$

Tensor pertubations are characterized by a metric with $g_{00} = 1$, zero space-time components $g_{0i} = 0$, and spatial elements

$$g_{ij} = a^2 \begin{pmatrix} 1 + h_+ & h_\times & 0 \\ h_\times & 1 - h_+ & 0 \\ 0 & 0 & 1 \end{pmatrix}.$$

The perturbations to the metric are described by two functions h_+ and $h_\times$ (Fig. 2.3). Here, we have chosen the perturbations to be in the x-y plane, which corresponds to choosing the z axis to be in the direction of the wavevector $\vec{k}$. For the tensor perturbations, the Einstein equations leads to

$$h''_\alpha + 2\left(\frac{a'}{a}\right)h'_\alpha + k^2 h_\alpha = 0, \tag{2.24}$$

where $\alpha = +, \times$, and primes denote derivatives with respect to conformal time η. Eq. 2.24 is a wave equation for gravitational wave. The second term is the damping term coming from the expansion of the universe.

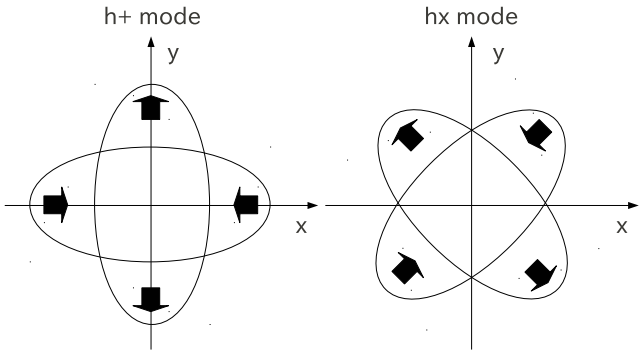

Figure 2.3: Quadrupole anisotropy induced by gravitational waves (S. Dodelson, 2003).

Fig. 2.4 shows the evolution of h_α for three different wavelength modes. The large scale mode with $k\eta = 10$ remains constant at early times when its wavelength is larger than the horizon, $k\eta < 1$. Once its wavelength becomes comparable to the horizon, $k\eta \sim 1$, the solution oscillates several times until the present epoch, and the amplitude begins to die off. For the small scale mode with $k\eta_0 = 1000$, the horizon entry occurs much earlier and its amplitude is extremely small at decoupling ($\eta/\eta_0 \simeq 0.02$). Therefore, anisotropies on small angular scales will not be affected by gravitational waves. Only the large-scale anisotropies are affected.

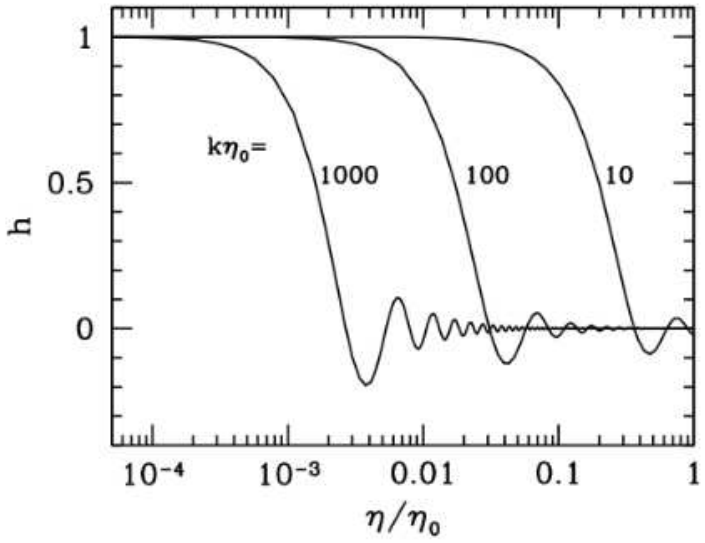

Figure 2.4: Evolution of gravitational waves as a function of conformal time. Three different modes are shown, labelled by their wavenumbers. Smaller scale modes decay earlier (S. Dodelson, 2003).

Returning to the Eq. 2.24, we define

$$\tilde{h} \equiv \frac{ah}{\sqrt{16\pi G}} \tag{2.25}$$

to transform this equation into the form of SHO, which gives us

$$\tilde{h}'' + \left(k^2 - \frac{a''}{a}\right)\tilde{h} = 0. \tag{2.26}$$

This equation has no damping term, so an expression for the quantum operator is immediately given as

$$\hat{\tilde{h}}(\vec{k},\eta) = v(k,\eta)\hat{a}_{\vec{k}} + v^*(k,\eta)\hat{a}^\dagger_{\vec{k}}, \tag{2.27}$$

which follows

$$v'' + \left(k^2 - \frac{a''}{a}\right)v = 0. \tag{2.28}$$

The variance of perturbations is given by

$$\langle \hat{\tilde{h}}^\dagger(\vec{k},\eta)\hat{\tilde{h}}(\vec{k'},\eta)\rangle = |v(k,\eta)|^2\delta^3(\vec{k}-\vec{k'}), \tag{2.29}$$

then, after transforming back $\tilde{h}$ to h, we see

$$\langle \hat{h}^\dagger(\vec{k},\eta)\hat{h}(\vec{k'},\eta)\rangle = \frac{16\pi G}{a^2}|v(k,\eta)|^2\delta^3(\vec{k}-\vec{k'}) \tag{2.30}$$

$$\equiv \frac{2\pi^2}{k^3}P_t(k)\delta^3(\vec{k}-\vec{k'}), \tag{2.31}$$

where the second line defines the power spectrum of the primordial perturbations to the metric. From this definition, the power spectrum of tensor perturbations are given by

$$P_t(k) = 16\pi G \left(\frac{k^3}{2\pi^2}\right) \frac{|v(k,\eta)|^2}{a^2} \tag{2.32}$$

To determine the spectrum of tensor perturbations produced during inflation, we have to solve the second order differential equation, Eq. 2.28, for $v(k,\eta)$. Since $\ddot{a}/a \simeq 2/\eta^2$, the equation for v becomes

$$v'' + \left(k^2 - \frac{2}{\eta^2}\right) v = 0. \tag{2.33}$$

The initial conditions necessary to solve this equation come from considering v at very early times before inflation has done most of its work. At that time, $-\eta$ is large, of order of the primordial comoving horizon, so the k^2 term dominates, and the equation is reduced to the form of SHO. In that case, the proper solution is given by

$$v = \frac{\mathrm{e}^{-ik\eta}}{\sqrt{2k}} \left[1 - \frac{i}{k\eta}\right]. \tag{2.34}$$

The evolution of mode h with wavenumber k according to this solution can be interpreted as follows. When the mode is well within the horizon ($k|\eta| >> 1$), the amplitude of h decays as $h \propto 1/a$. At $k\eta = 1$, the mode leaves the horizon. Well outside of the horizon (-$k\eta \to 0$), h becomes constant:

$$v \sim \frac{\mathrm{e}^{-ik\eta}}{\sqrt{2k}} \frac{i}{k\eta} \qquad (-k\eta \to 0) \tag{2.35}$$

The primordial power spectrum for tensor modes, which scales as $|v|^2/a^2$, is thus constant after the mode exits the horizon. This constant determines the initial conditions with which to start off $h_{\times,+}$ at the time after inflation but before decoupling. The primordial power spectrum for tensor modes is then

$$P_t(k) = \frac{16\pi G}{a^2} \left(\frac{k^3}{2\pi^2}\right) \frac{1}{2k^3\eta^2} \tag{2.36}$$

$$\simeq 16\pi G \left(\frac{H}{2\pi}\right)^2. \tag{2.37}$$

We have assumed H is constant in deriving the second line. In slow-roll inflation, the Hubble rate varies slowly, so we can treat H as a constant, then $\eta \simeq -1/aH$. Since $H \sim$ *constant* during inflation, P_t is nearly scale-invariant and it also follows that the detection of primordial gravitational waves gives us the Hubble rate during inflation. Furthermore, since the Hubble rate is dominated by potential energy during inflation, it also gives us $V(\phi)$ at horizon exit.

Finally, Eq. 2.37 is the power spectrum for h_+ and $h_\times$ separately, and each polarization contributes twice to the metric perturbations; these are uncorrelated, so the power spectrum for all modes must be multiplied by a factor of 4. Thus, we finally obtain the tensor power spectrum for inflation:

$$P_t(k) = 64\pi G \left(\frac{H}{2\pi}\right)^2 \equiv \frac{8}{M_{pl}^2} \left(\frac{H}{2\pi}\right)^2. \tag{2.38}$$

2.1.6 Scalar pertubations

The zero-order scheme ensures that the universe will be uniform on all scales today, but there are pertubations about this zero-order scheme. We decompose the scalar field into a zero-order homogeneous part and a perturbation:

$$\phi(\vec{x},t) = \phi^{(0)}(t) + \delta\phi(\vec{x},t), \tag{2.39}$$

and find an equation governing $\delta\phi$ assuming the smoothly expanding universe with metric ($g_{00} = -1; g_{ij} = \delta_{ij}a^2$). Under this assumption, only first order pieces are perturbations to $T_{\mu\nu}$, and after the usual Einstein equation manipulations, we find

$$\delta\phi'' + 2\left(\frac{a'}{a}\right)\delta\phi' + k^2\delta\phi = 0, \tag{2.40}$$

This equation has the same form as the tensor case Eq. 2.24, and we can copy the solution, dropping the tensor normalization factor $16\pi G$ as we already have a canonical scalar field:

$$P_{\delta\phi} = \left(\frac{H}{2\pi}\right)^2. \tag{2.41}$$

The right-hand side is evaluated when the mode k exits the Hubble radius. Since H varies very slowly during inflation, the scalar power spectrum is also nearly scale-invariant, which is the same as the tensor perturbation case. This is one of the most generic and important observational predictions of inflation.

We want to know how fluctuations in ϕ get transferred to Ψ(Newtonian potential) or Φ(perturbation to the spatial curvature) so that we can relate inflationary perturbations to initial density fluctuations. The trick is to find different gauges which have gauge-invariant variable linking to Φ in one gauge and to $\delta\psi$ in the other gauge. It turns out that the appropriate gauge-invariant combo that translates between the two gauges is the previously-heralded comoving curvature perturbation,

$$\mathcal{R} = -\frac{aH}{\partial_\eta\phi^{(0)}}\delta\psi, \tag{2.42}$$

immediately giving us the power spectrum,

$$P_{\mathcal{R}} = \left(\frac{aH}{\partial_\eta\phi^{(0)}}\right)^2 P_{\delta\psi} \equiv \left(\frac{H}{\partial_t\phi^{(0)}}\right)^2\left(\frac{H}{2\pi}\right)^2 \equiv \left(\frac{H^2}{2\pi\partial_t\phi^{(0)}}\right)^2. \tag{2.43}$$

(The right hand side is evaluated at horizon exit, $k = aH$.)

2.1.7 Spectral index of the primordial power spectrum

As discussed above, slow-roll inflation produces a spectrum of curvature perturbations that is almost scale-invariant. The small departures from the scale-invariance can be quantified by forming the spectral index $n_s(k)$. Generally, this is a scale-dependent quantity defined by

$$n_s - 1 \equiv \frac{d\ln P_{\mathcal{R}}}{d\ln k}, \tag{2.44}$$

where $n_s = 1$ means a scale-free spectrum, and a constant n_s does a power-law spectrum,

$$P_{\mathcal{R}}(k) = A_s(k_*)\left(\frac{k}{k_*}\right)^{n_s-1}, \tag{2.45}$$

where k_* is a pivot scale. We can evaluate n_s by using the Friedmann equations and the slow-roll approximation at $k = aH$, Hubble exit. As a result, the primodial spectral index of scalar perturbations produced by inflation is found to be

$$n_s = 1 - 6\epsilon + 2\eta. \tag{2.46}$$

The running of the spectral index is also defined as

$$\alpha_s \equiv \frac{dn_s}{d\ln k}. \tag{2.47}$$

With the spectral index, n_s, and its running, α_s, the scalar power spectrum is often approximated as

$$P_{\mathcal{R}}(k) = A_s(k_*)\left(\frac{k}{k_*}\right)^{n_s - 1 + \frac{1}{2}\alpha_s(k_*)\ln(k/k_*))}. \tag{2.48}$$

The scale-dependence of the tensor power spectrum is also defined by

$$n_t \equiv \frac{d\ln P_t}{d\ln k} \qquad P_t(k) = A_t(k_*)\left(\frac{k}{k_*}\right)^{n_t}. \tag{2.49}$$

We can evaluate n_t by noting that

$$\frac{d\ln H}{d\ln k}\Big|_{k=aH} = \frac{k}{H}\frac{dH}{d\eta} \times \frac{d\eta}{dk} = -\frac{k}{H}\frac{aH^2\epsilon}{k^2} = -\epsilon \tag{2.50}$$

using $\dot{H} = -aH^2\epsilon$ and $d\eta/dk = -d(aH)^{-1}/dk = 1/k^2$. Therefore, the primodial spectral index of tensor perturbations produced by inflation is found to be

$$n_t = 2 \times \frac{d\ln H}{d\ln k}\Big|_{k=aH} = -2\epsilon. \tag{2.51}$$

The fact that the tensor index n_t is proportional to ϵ leads to one of the robust predictions of inflation. Many inflationary models have been proposed which offer different predictions for ϵ and η. However, almost all of the models maintains the feature that the ratio of tensor to scalar modes is directly related to the tensor spectral index,

$$r \equiv \frac{P_t}{P_{\mathcal{R}}} = \frac{8}{M_{pl}^2}\left(\frac{\dot{\phi}}{H}\right)^2 = 16\epsilon \tag{2.52}$$

$$= -8n_t. \tag{2.53}$$

Models of single-field slow-roll inflation makes definite predictions for the primordial scalar and tensor fluctuation spectra. Under the slow-roll approximation, we can relate the predictions for $P_{\mathcal{R}}(k)$ and $P_t(k)$ to the shape of the inflation potential $V(\phi)$. Measuring the amplitudes of $P_t(\propto V)$, $P_{\mathcal{R}}(\propto V')$, and the scale-dependence of the scalar spectrum $n_s(\propto V'')$, $\alpha_s(\propto V''')$ allows a reconstruction of the inflation potential as a Taylor expansion around ϕ_* (correspoding to the time when fluctuations on CMB scales exited the horison) as

$$V(\phi) = V|_* + V'|_*(\phi - \phi_*) + \frac{1}{2}V''|_*(\phi - \phi_*)^2 + \frac{1}{3!}V'''|_*(\phi - \phi_*)^3 + \cdots. \tag{2.54}$$

Otherwise, if we assume that the primordial perturbations are produced by an inflationary model with a single slowly rolling scalar field, we can fit directly to the slow-roll parameters, bypassing the spectral indices entirely, and then reconstruct the form of the underlying potential.

2.1.8 Energy scale of inflation

First, we set $\bar{\Phi} \equiv \phi^{(0)}$ here, which is proved to be valid. For a slowly-rolling scalar field, we can express $P_{\mathcal{R}}(k)$ directly in terms of the inflaton potential. During the slow roll, the potential energy of the field dominates over the kinetic energy, so Eq. 2.16 and Eq. 2.17 leads to

$$H^2 \simeq \frac{V(\bar{\Phi})}{3M_{pl}^2} \tag{2.55}$$

$$3H\partial_t\bar{\Phi} \simeq -V_{,\bar{\Phi}}(\bar{\Phi}). \tag{2.56}$$

It follows that

$$P_{\mathcal{R}}(k) = \left(\frac{H^2}{2\pi\partial_t\bar{\Phi}}\right)^2 \simeq \left(\frac{3H^3}{2\pi V_{,\bar{\Phi}}}\right)^2 \simeq \frac{(V/M_{pl}^2)^3}{3(2\pi)^2(V_{,\bar{\Phi}})^2} \tag{2.57}$$

$$= \frac{3}{8}\left(\frac{V^{1/4}}{\sqrt{8\pi}M_{pl}}\right)^4 \frac{1}{\epsilon}, \tag{2.58}$$

where $\epsilon = (M_{pl}^2/2)(V'/V)^2$. The large-angle CMB observations constrain $P_{\mathcal{R}}(k) \sim 2 \times 10^{-9}$ on current Hubble scales. It follows that

$$V^{1/4} = 1.06 \times 10^{16} \times \left(\frac{r}{0.01}\right)^{1/4} (\text{GeV}). \tag{2.59}$$

The quantity $V^{1/4}$ describes the energy scale of inflation and, since $\epsilon << 1$, the energy scale is at least two orders of magnitude below the Planck scale ($\sim 10^{19}$ GeV). It is, however, plausible, that inflation occurred around the GUT scale, $\sim 10^{16}$ GeV.

2.2 CMB polarization: Probe of the early universe

2.2.1 CMB polarization

CMB polarization is one of the most important tools to probe inflation because we can access primordial gravitational waves created during the inflation era by measuring the CMB polarization.

The scalar perturbations make density fluctuations via gravitational potential, which induce acoustic oscillations in the cosmic plasma. Acoustic oscillations then create the CMB temperature anisotropy on typical angular scales. The scalar perturbations also induce even-parity scalar "E-mode" (Fig. 2.6) in the CMB polarization via Thomson scattering of the local quadrupole of the temperature anisotropy (Fig. 2.7). On the other hand, primordial gravitational waves (tensor perturbations) induce odd-parity tensor "B-mode" (Fig. 2.6). We can determine the amplitude of primordial gravitational waves by measuring the B-mode signal as well as the tensor-to-scalar ratio. Therefore, the detection of B-mode is a "smoking gun" of tensor modes, and therefore of inflation.

2.2.2 E/B decomposition

The cosmological importance of the E/B decomposition of CMB polarization comes from the remarkable facts: i) scalar (density) perturbations create only E-modes and no B-modes. ii) vector (vorticity) perturbations create mainly B-modes. (But vector modes decay quickly, so negligible.) iii) tensor (gravitational wave) perturbations create both E-modes and B-modes. The fact that scalars do not produce B-modes while tensors do is the basis for the statement

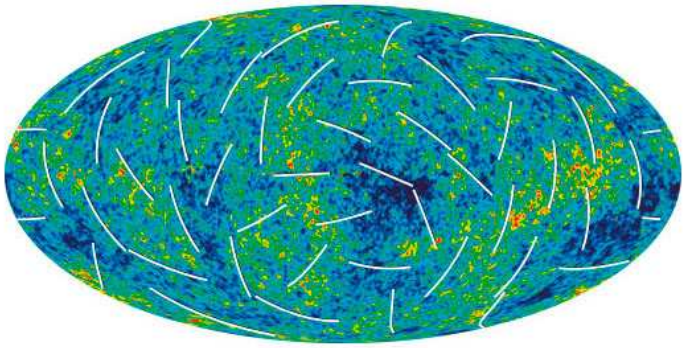

Figure 2.5: CMB Polarization Map by WMAP three year result. Colors indicate "warmer" (red) and "cooler" (blue) spots. The white bars show the "polarization" direction (LAMBDA).

that the search for the primordial B-mode signature in CMB polarization is often considered the "holy grail" of inflationary cosmology.

The details of the mathematical characterization of CMB temperature and polarization anisotropies are as follows. The anisotropy field is defined in terms of a 2×2 intensity tensor $I_{ij}(\hat{n})$, where $\hat{n}$ denotes the direction on the sky. The components of I_{ij} are defined relative to two orthogonal basis vectors $\hat{e_1}$ and $\hat{e_1}$ perpendicular to $\hat{n}$. Linear polarization is then described by the Stokes parameters $Q = \frac{1}{4}(I_{11} - I_{22})$ and $U = \frac{1}{2}I_{12}$, while the temperature anisotropy is $T = \frac{1}{4}(I_{11} + I_{22})$. The polarization magnitude and angle are $P = \sqrt{Q^2 + U^2}$ and $\alpha = \frac{1}{2}\tan^{-1}(U/Q)$. The quantity T is invariant under a rotation in the plane perpendicular to $\hat{n}$ and hence may be expanded in terms of scalar spherical harmonics

$$T(\hat{n}) = \sum_{l,m} a^T_{lm} Y_{lm}(\hat{n}) \tag{2.60}$$

The quantities Q and U, however, transform under rotation by an angle ψ as a spin-2 field $(Q \pm iU)(\hat{n}) \to e^{\mp 2i\psi}(Q \pm iU)(\hat{n})$. The harmonic analysis of $Q \pm iU$ therefore requires expansion on the sphere in terms of tensor (spin-2) spherical harmonics

$$(Q \pm iU)(\hat{n}) = \sum_{l,m} a^{(\pm 2)}_{lm} \, {}_{(\pm 2)}Y_{lm}(\hat{n}) \tag{2.61}$$

where the multipole coefficient $a^{(\pm 2)}_{lm}$ can be evaluated by

$$a^{(\pm 2)}_{lm} = \int d\Omega(\hat{n})(Q \pm iU)(\hat{n}) Y_{lm}(\hat{n}). \tag{2.62}$$

In terms of $a^{(\pm 2)}_{lm}$, the E-mode and B-mode are defined as

$$a^E_{lm} \equiv -\frac{1}{2}(a^{(+2)}_{lm} + a^{(-2)}_{lm}), \qquad a^B_{lm} \equiv -\frac{1}{2i}(a^{(+2)}_{lm} + a^{(-2)}_{lm}). \tag{2.63}$$

Therefore, angular power spectra of the E-mode and B-mode are constructed as follows:

$$C^{EE}_l = \frac{1}{2l+1} \sum_{m=-l}^{+l} < a^E_{lm} a^{E^*}_{lm} >, \qquad C^{BB}_l = \frac{1}{2l+1} \sum_{m=-l}^{+l} < a^B_{lm} a^{B^*}_{lm} > . \tag{2.64}$$

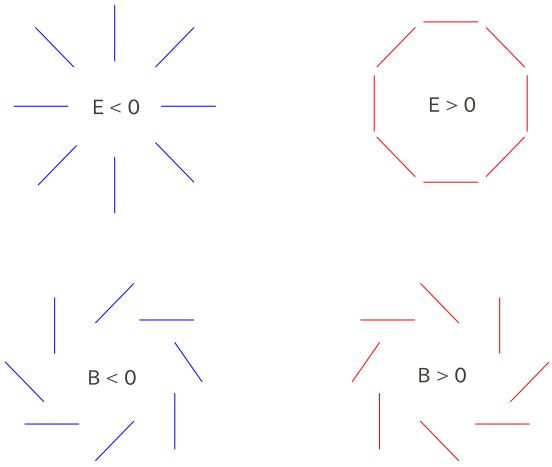

Figure 2.6: E-mode and B-mode patterns of polarization. Note that if reflected across a line going through the center the E-patterns are unchanged, while the positive and negative B-patterns get interchanged (Hu et al., 1997).

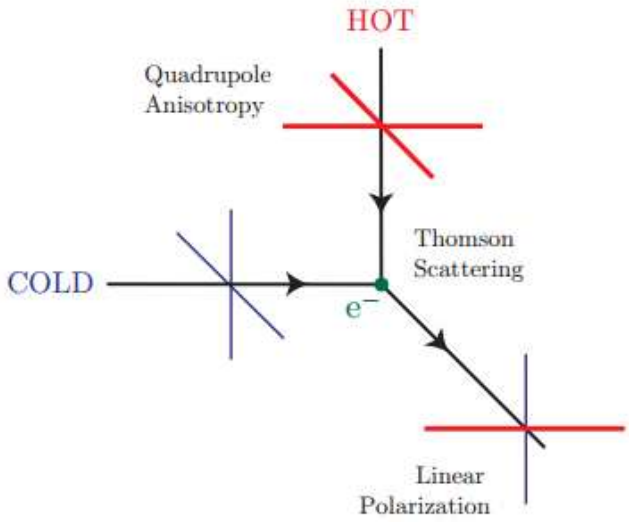

Figure 2.7: Thomson scattering of radiation with a quadrupole anisotropy generates linear polarization. Red colors (thick lines) represent hot radiation, and blue colors (thin lines) cold radiation (Hu et al., 1997).

E-mode and B-mode specify the linear polarization field. E-mode polarization is often characterized as a curl-free mode with polarization vectors that are radial around cold spots and tangential around hot spots on the sky. In contrast, B-mode polarization is divergence-free but has a curl: its polarization vectors have vorticity around any given point on the sky (Fig. 2.6). Although E-mode and B-mode are both invariant under rotations, they behave differently under parity transformations. When reflected about a line going through the center, the E-patterns remain unchanged, while B-patterns change sign. Although there are six power spectra with cross-correlations among the temperature anisotropy, T, E-mode and B-mode of harmonic coefficients, only C_l^{TT}, C_l^{TE}, C_l^{EE}, C_l^{BB} are non-zero because the E-mode has positive parity and the B-mode has negative parity.

Fig. 2.8 shows predicted CMB power spectra for the temperature anisotropy and polarization of the E-mode and B-mode. Adopting the cosmological parameters except the tensor-to-scalar ratio from the concordance ΛCDM model with an assumption of the tensor index $n_t = 0$, the B-mode power spectrum is proportional to the concordance template by the tensor-to-scalar. Many experiments, which have an enough sensitivity to detect the B-mode to r = 0.01 level, are planned, and certain ones are ongoing.

In contrast to CMB polarization experiments, a direct detection of primordial gravitational waves by very large interferometers is another way to test inflation. The interferometers have a potential to detect primordial gravitational waves of higher frequencies. However, the sensitivity of the interferometers today is about seven orders of magnitude worse than that of the CMB experiments (Fig. 2.9) and they probe different wavelengths. Some (mostly spaceborne) interferometer projects, which would have a enough sensitivity to detect primordial gravitational waves as much as the CMB polarization experiments, are planned; however, those instruments also involve massive technological challenges. It will optimistically take decades to be developed and launched.

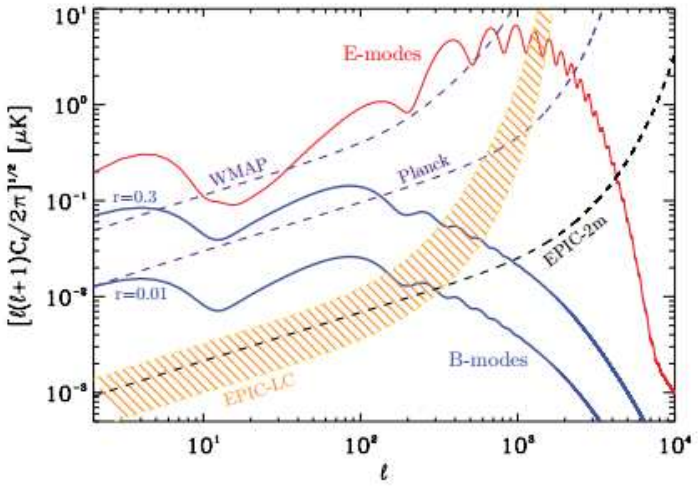

Figure 2.8: E-mode and B-mode power spectra for a tensor-to-scalar ratio saturating current bounds, r = 0:3, and for r = 0:01. Shown are also the experimental sensitivities for WMAP, Planck and two different realizations of a future CMB satellite (CMBPol) (EPIC-LC and EPIC-2m) (Baumann et al., 2009).

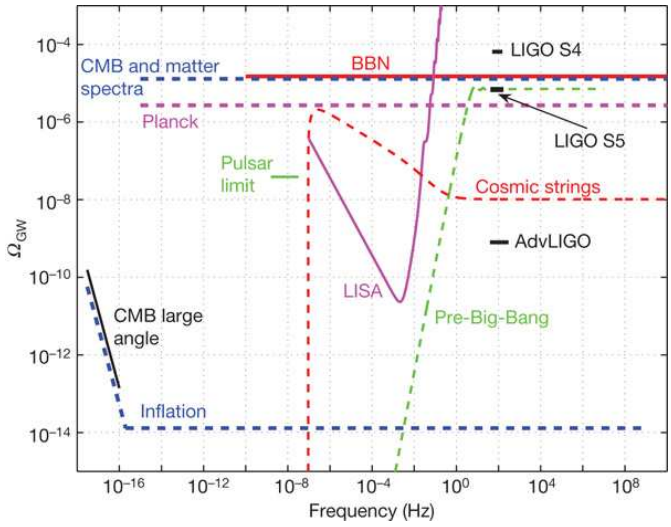

Figure 2.9: Energy density of primordial gravitational waves (Ω_{GW}) as a function of frequency to todays horizon scale. Sensitivity curves of interferometer experiments (LIGO, AdvLIGO, and LISA), CMB experiments and todays limits are also shown on the plot (LIGO Scientific Collaboration & Virgo Collaboration., 2009).

2.2.3 Observable predictions and current observational constraints

Primordial gravitational waves are not discovered yet. We have just upper limits on the tensor-to-scalar ratio. Here, we review the current observational constraints on the primordial power spectra $P_s(k)$ and $P_t(k)$.

Bennett et al. (2012) and Hinshaw et al. (2012) recently released the WMAP 9-year temperature and polarization data combined with eCMB(ACT and SPT), BAO and H_0 observations, and put constraints on the primordial power spectra. That is summarized in Tab. 2.1.

Parameter	9-year WMAP	WMAP+eCMB+BAO+H_0
r	< 0.38 (95% CL)	< 0.13 (95% CL)
n_s	0.992 ± 0.019	0.9636 ± 0.0084
α_s	-0.019 ± 0.025	-0.023 ± 0.011
n_s	1.009 ± 0.049	1.020 ± 0.029
r	< 0.50 (95% CL)	< 0.47 (95% CL)
α_s	-0.032 ± 0.028	-0.040 ± 0.016
n_s	1.058 ± 0.063	1.075 ± 0.046

Table 2.1: 9-year WMAP constraints on the primordial power spectrum. The tensor mode amplitude(r, n_s) and scalar running index parameter (α_s, n_s) are each fit singly, and then jointly (Hinshaw et al., 2012).

A power-law parameterization of the power spectrum is expressed as

$$P_s(k) = A_s(k_*) \left(\frac{k}{k_*}\right)^{n_s - 1 + \frac{1}{2}\alpha_s(k_*)\ln(k/k_*))} . \tag{2.65}$$

The amplitude of scalar fluctuations at $k_* = 0.002$ Mpc^{-1} is found to be

$$A_s = (2.464 \pm 0.072) \times 10^{-9} \quad (\mathrm{WMAP + eCMB + BAO + H_0}). \tag{2.66}$$

Assuming no tensors ($r = 0$), the scale-dependence of the power spectrum is

$$n_s = 0.9636 \pm 0.0084 \quad (\mathrm{WMAP} + \mathrm{eCMB} + \mathrm{BAO} + \mathrm{H}_0). \tag{2.67}$$

The scale-invariant Harrison-Zel'dovich-Peebles spectrum, $n_s = 1$, is disfavored with more than 5 standard deviations away from the mean of the likelihood (Fig. 2.10). Tab. 2.1 also shows the tightest constraint for r

$$r < 0.13 \quad (95\%\mathrm{CL}). \tag{2.68}$$

The constraint on r is driven mainly by the temperature data and the temperature-polarization cross correlation; constraints on B-mode polarization make a negligible contribution to the current limit on r (Fig. 2.11). Since the B-mode limit contributes little to the limit on r, and most of the information essentially comes from the TT and TE measurements, the current limit on r is somewhat degenerate with n_s (Fig. 2.10). Better limits on n_s therefore correlate strongly with better limits on r.

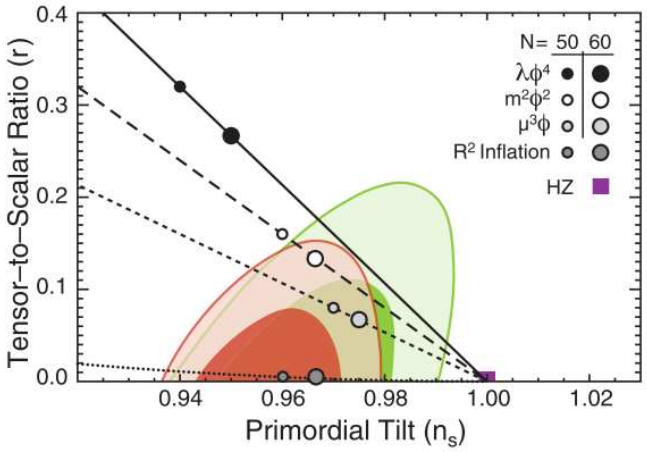

Figure 2.10: Two-dimensional marginalized constraints (68% and 95% CL) on the primordial tilt, n_s, and the tensor-to-scalar ratio, r, derived with the nine-year WMAP in conjunction with: eCMB (green) and eCMB+BAO+H0 (red). The symbols and lines show predictions from single-field inflation models whose potential is given by $V(\phi) \propto \psi^\alpha$ (Linde , 1983), with $\alpha = 4$ (solid), $\alpha = 2$ (long-dashed), and $\alpha = 1$ (short-dashed; McAllister et al. (2010)). Also shown are those from the first inflation model, which is based on an R2 term in the gravitational Lagrangian (dotted; Starobinsky et al. (1980)) (Hinshaw et al., 2012).

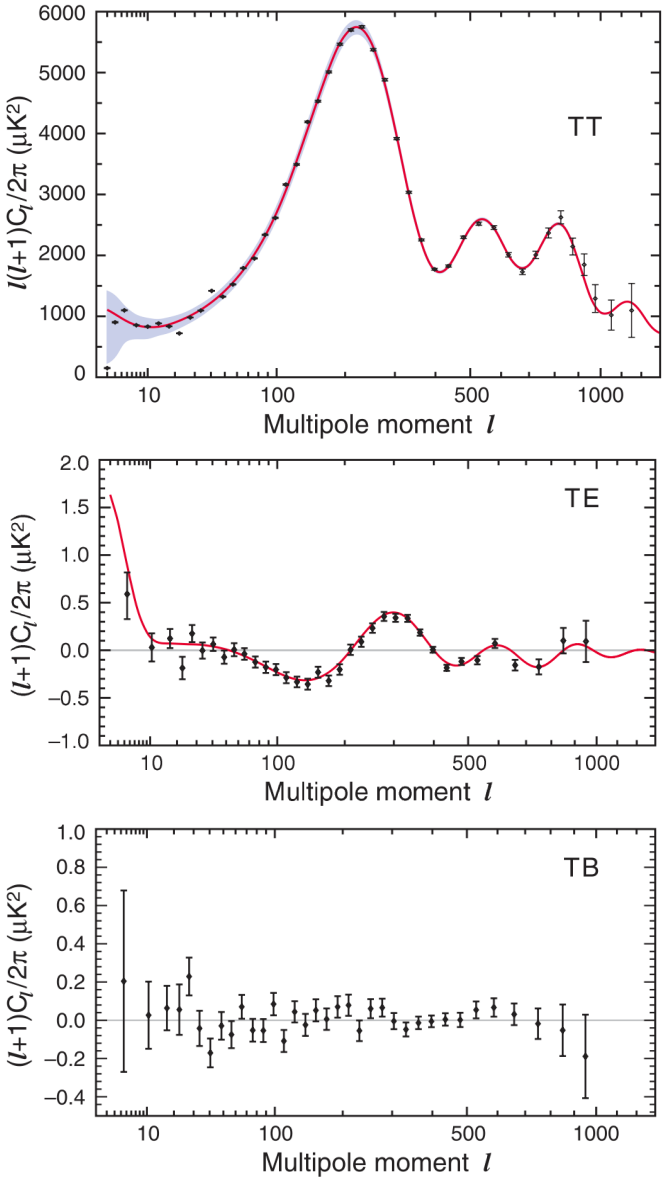

Figure 2.11: TT, TE, TB power spectrum by 9-year WMAP data (Bennett et al., 2012).

Chapter 3

Foreground Emission in the Microwave Band

In the microwave range, four foreground emission components are known besides the CMB signal: synchrotron, free-free, thermal dust, spinning dust emission (Fig. 3.1). Fig. 3.2 shows that EE and BB polarization power spectra are much higher than the polarization spectrum in CMB. In addition, spinning dust emission is very uncertain and prone to confusion with synchrotron and free-free emission. 10 GHz data will provide a wealth of data on these galactic emissions and be useful for polarized foreground subtraction from CMB measurements. In this chapter, we summarize emission mechanisms of the foreground emissions.

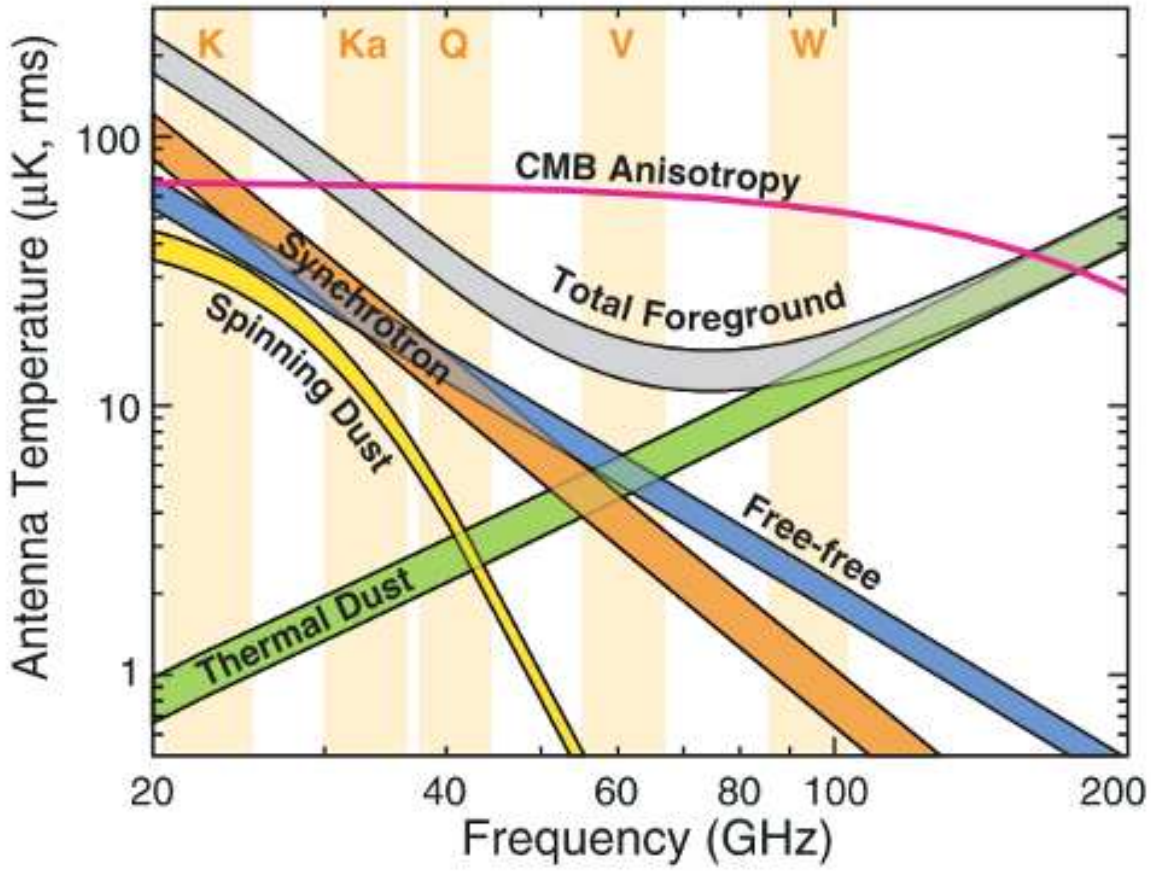

Figure 3.1: CMB vs. foreground anisotropy (Bennett et al., 2012). The rms anisotropy as a function of frequency from the CMB (red line) and four known sources of foreground emission: synchrotron, free-free, thermal dust and spinning dust emission.

3.1 Synchrotron emission

Charged particles moving in the magnetic field are accelerated by the Lorentz force and radiate its energy as photons, which is called synchrotron emission. In the following, we shall estimate the total emission power of the synchrotron emission due to electrons (Rybicki & Lightman, 1979). The relativistic form of the equation of motion for an electron (with charge of e, mass of m and velocity of $\boldsymbol{v}$) is

$$\frac{d}{dt}(\gamma m \boldsymbol{v}) = \frac{e}{c}\boldsymbol{v} \times \boldsymbol{B} \tag{3.1}$$

$$\frac{d}{dt}(\gamma m c^2) = e\boldsymbol{v} \cdot \boldsymbol{E} = 0 \tag{3.2}$$

where γ is Lorentz factor, c is speed of light, and $\boldsymbol{B}$ is magnetic field. Here we assume zero electric field ($\boldsymbol{E} = 0$). The second equation implies that $\gamma =$ constant. Therefore, it follows that

$$m\gamma \frac{d\boldsymbol{v}}{dt} = \frac{e}{c}\boldsymbol{v} \times \boldsymbol{B}. \tag{3.3}$$

We can separate the velocity into two components parallel and perpendicular to $\boldsymbol{B}$ as:

$$\frac{d\boldsymbol{v}_{\parallel}}{dt} = 0, \qquad \frac{d\boldsymbol{v}_{\perp}}{dt} = \frac{q}{\gamma m c}\boldsymbol{v}_{\perp} \times \boldsymbol{B}. \tag{3.4}$$

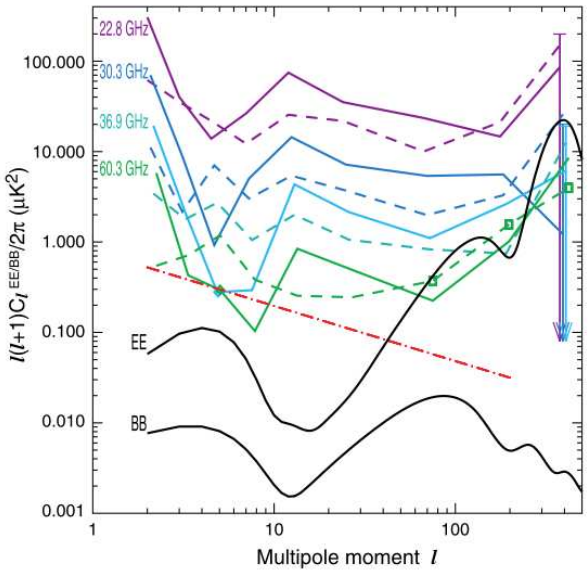

Figure 3.2: EE and BB polarization spectra (Page et al., 2007). Absolute value of the EE (solid lines, violet through green) and BB (dashed lines, violet through green) polarization spectra. The best-fit ΛCDM model to TT, TE, and EE data with $\tau = 0.09$ and an additional tensor contribution with $r = 0.3$ is shown in black.

It follows that $\boldsymbol{v}_{\parallel}$ = constant, and $|\boldsymbol{v}_{\perp}|$ = const since $|\boldsymbol{v}|$ is constant, which describes the linear motion and the circular motion with constant velocities.
The gyration frequency of the rotation is given by

$$\omega_B = \frac{eB}{\gamma mc}. \tag{3.5}$$

The acceleration is perpendicular to the velocity with $a_{\perp} = \omega_B v_{\perp}$, so the total emitted power for a relativistic electron is

$$P = \frac{2e^2\dot{u}^2}{3c^3}\gamma^4 = \frac{2e^2}{3c^3}\gamma^4\frac{e^2B^2}{\gamma^2m^2c^2}v_{\perp}^2 = \frac{2}{3}r_0^2c\beta_{\perp}^2\gamma^2B^2, \tag{3.6}$$

where $r_o = e^2/mc^2$ and $\beta = v/c$.
When we assume an isotropic distribution of v, the average of $\beta_{\perp}$ can be calculated,

$$\langle\beta_{\perp}\rangle = \frac{\beta^2}{4\pi}\int \sin^2\alpha d\Omega = \frac{2}{3}\beta^2. \tag{3.7}$$

where α is an inclination of the velocity vector to the magnetic field, which is called "pitch angle". Finally we obtain the averaged power of the synchrotron emission,

$$\langle P_{\rm sync}\rangle = \frac{4}{3}\sigma_T c\gamma^2\beta^2U_B^2, \tag{3.8}$$

where $\sigma_T = (8\pi/3)(e^4/m^2c^4)$ is the Thomson cross section, and $U_B = B^2/8\pi$ is the energy density of the magnetic field.

The synchrotron emission is strongly beamed to the direction of the motion, perpendicular to the acceleration. Relativistic boosting effect is along the direction of the motion by a factor of γ^2 and the emission is concentrated into an angle of the order of $1/\gamma$. As the electron cycles

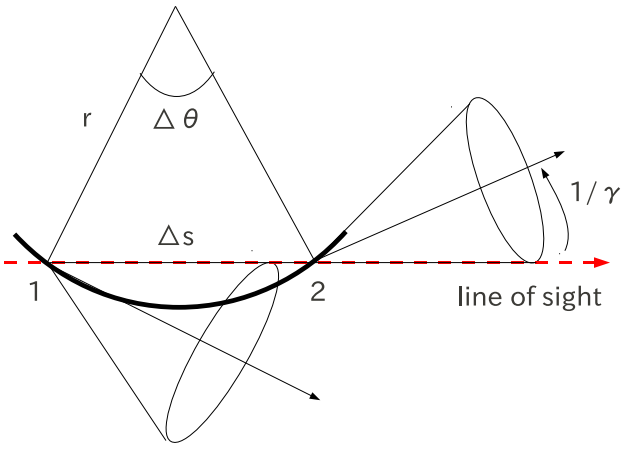

Figure 3.3: Geometry of observable synchrotron emission (Rybicki & Lightman, 1979).

around the helical path along the magnetic field line, a distant observer can see the emission only when the beam is aligned with the line of sight. The period is much shorter than the gyration period. In the case of non-relativistic motion, the observed frequency is given by $\nu = \omega_B/2\pi$. In the case of the relativistic electron, the spectrum is broadened.

Fig. 3.3 shows the geometry of the synchrotron emission. Here $\Delta\theta = 2/\gamma$ and $\Delta s = r\Delta\theta = 2r/\gamma$ can be obtained from the definition in the figure. The radius of curvature of the path follows the equation of motion

$$\gamma m \frac{\Delta \boldsymbol{v}}{\Delta t} = \frac{e}{c}\boldsymbol{v} \times \boldsymbol{B}, \tag{3.9}$$

where $\Delta\boldsymbol{v}$ andΔs can be replaced with $v\Delta\theta$ and $v\Delta t$ respectively. Thus, we obtain Δs,

$$\Delta s = \frac{2v}{\gamma\omega_B \sin\alpha}. \tag{3.10}$$

The interval of the time the electron passes points between 1 and 2, Δt, is written as

$$\Delta t = \frac{\Delta s}{v} = \frac{2}{\gamma\omega_B \sin\alpha}, \tag{3.11}$$

then for the observer, the time interval ΔT is

$$\Delta T = \frac{2}{\gamma\omega_B \sin\alpha}\left(1 - \frac{v}{c}\right) \approx \frac{1}{\gamma^3\omega_B \sin\alpha}, \tag{3.12}$$

where the approximation of $1 - v/c \approx 1/2\gamma^2$ for $\gamma \gg 1$ is used. The so-called critical frequency ω_c,

$$\omega_c = \frac{3}{2}\gamma^3\omega_B \sin\alpha, \tag{3.13}$$

characterises the extent of the synchrotron spectrum. When we define $x \equiv \omega/\omega_c$, the synchrotron power spectrum of a single electron is

$$P(\omega) = \frac{\sqrt{3}e^2 B \sin\alpha}{2\pi mc^2} F(x). \tag{3.14}$$

Here

$$F(x) \equiv x \int_x^\infty K_{5/3}(\xi) d\xi \tag{3.15}$$

and $K(\xi)$ is the modified Bessel function.

The discussion above corresponds to the emissivity of a single electron, while the emission from astrophysical objects are due to electrons with certain energy distributions. Let us assume a power-law distribution of electrons as $N(\gamma)d\gamma \propto \gamma^{-p}d\gamma$, where $N(\gamma)$ is the number of electrons with energies between γ_1 and γ_2, and p is a spectral index of electrons. Then the total power of the synchrotron emission from all the electrons, $P_{\rm tot}(\omega)$, is

$$P_{\rm tot}(\omega) \propto \int_{\gamma_1}^{\gamma_2} P(\omega)\gamma^{-p}d\gamma \propto \int_{\gamma_1}^{\gamma_2} F(x)\gamma^{-p}d\gamma. \tag{3.16}$$

Note that $\omega_c \propto \gamma^2$ yields $\gamma \propto (\omega/x)^{1/2}$ and $d\gamma/dx \propto -(1/2)x^{-3/2}\omega^{1/2}$. The change of the variable from γ to x gives

$$P_{\rm tot} \propto \omega^{-\frac{p-1}{2}} \int_{x_1}^{x_2} F(x)x^{\frac{p-3}{2}}dx. \tag{3.17}$$

When we approximate $x_1 \approx 0$ and $x_2 \approx \infty$, the integration term is a constant, and we obtain

$$P_{\rm tot} \propto \omega^{-\frac{p-1}{2}}. \tag{3.18}$$

Thus, for a power-law distribution of electron energies $N(E) \propto E^{-p}$ propagating in a uniform magnetic field, the synchrotron emission is also a power-law,

$$T_b(\nu) \propto \nu^{-\beta} \quad (\beta = \frac{p+3}{2}) \tag{3.19}$$

where T_b is brightness temperature.

3.2 Free-Free emission

Radiation due to the acceleration of a charge in the Coulomb field of another charge is called bremsstrahlung or free-free emission. In the following, we shall give an approximation of the total emission power of the free-free emission due to electrons in a non-relativistic and classical limit (Rybicki & Lightman, 1979). Here, we assume that the energy lost by an electron is much smaller than the initial electron energy when it interacts with an ion.

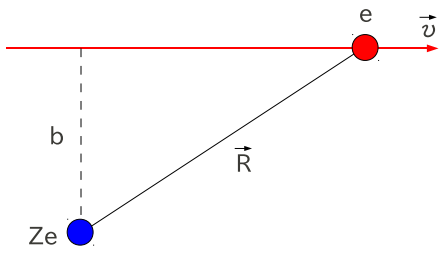

Figure 3.4: Geometry of free-free emission (Rybicki & Lightman, 1979).

We use a dipole approximation, $\boldsymbol{d} = -e\boldsymbol{R}$, and then take its second derivative on both side.

$$\boldsymbol{d} = -e\dot{\boldsymbol{v}} \tag{3.20}$$

Taking the Fourier transform of this equation, we get

$$-\omega^2 \hat{d}(\omega) = -\frac{e}{2\pi}\int_{-\infty}^{\infty} \dot{\boldsymbol{v}} e^{i\omega t} dt. \tag{3.21}$$

Most of the acceleration of the particle occurs during a short time in which R $\sim$ b, which is called collision time.

$$\tau_c = \frac{b}{v} \tag{3.22}$$

For $\omega\tau \gg 1$, the exponential in the integral oscillates rapidly and the integral becomes small. For $\omega\tau \ll 1$, the exponential becomes essentially unity, so

$$\hat{\boldsymbol{d}}(\omega) \sim \begin{cases} \frac{e}{2\pi\omega^2}\Delta\boldsymbol{v} & (\omega\tau \ll 1) \\ 0 & (\omega\tau \gg 1) \end{cases}$$

where $\Delta\boldsymbol{v}$ is the change of velocity during the collision.
The energy spectrum is given by

$$\frac{dW(b)}{d\omega} = \frac{8\pi\omega^4}{3c^3}|\hat{d}(\omega)|^2 = \begin{cases} \frac{2e^2}{3\pi c^3}\Delta\boldsymbol{v} & (\omega\tau \ll 1) \\ 0 & (\omega\tau \gg 1). \end{cases}$$

$\Delta\boldsymbol{v}$ can be estimated by the approximation that the change in velocity is predominantly normal to the path.

$$\Delta\boldsymbol{v} = \int_{-\infty}^{\infty} \frac{b}{R}\frac{1}{m}\frac{Ze^2}{R^2} = \frac{Ze^2}{m}\int_{-\infty}^{\infty} \frac{b}{(b^2+v^2t^2)^{3/2}} dt = \frac{2Ze^2}{mbv} \tag{3.23}$$

Thus, the emission from a single collision is

$$\frac{dW(b)}{d\omega} = \begin{cases} \frac{8Z^2e^6}{3\pi c^3 m^2 v^2 b^2} & (b \ll v/\omega) \\ 0 & (b \gg v/\omega) \end{cases}$$

We can determine the total spectrum with ion density n_i and electron density n_e for a fixed electron speed v by integrating over all impact parameters. The contribution to the spectrum for $b \gg v/\omega$ vanishes, so we set the minimum impact parameter b_{min}. We also set the maximum impact parameter b_{max}. Now that the flux of electrons incident on one ion is simply $n_e v$ and the element of area is $2\pi b db$ about a single ion, the total emission per unit time per unit volume per unit frequency range is then

$$\begin{aligned} \frac{dW}{d\omega dV dt} &= n_e n_i 2\pi v \int_{b_{min}}^{b_{max}} \frac{8Z^2e^6}{3\pi c^3 m^2 v^2 b^2} b db & (3.24) \\ &= \frac{16e^6}{3c^3m^2v} n_e n_i Z^2 \int_{b_{min}}^{b_{max}} \frac{db}{b} & (3.25) \\ &= \frac{16e^6}{3c^3m^2v} n_e n_i Z^2 \ln(\frac{b_{max}}{b_{min}}). & (3.26) \end{aligned}$$

The value of b_{max} is uncertain, but we can take order v/ω because b_{max} is inside the logarithm and its precise value is not very important. The value of b_{min} can be estimated by the value at which the straight-line approximation ceases to be valid, which is $b_{min} = 4Ze^2/\pi m v^2$. Generally, the spectrum is expressed as

$$\frac{dW}{d\omega dV dt} = \frac{16\pi e^6}{3\sqrt{3}c^3m^2v} n_e n_i Z^2 g_{ff}(v,\omega), \tag{3.27}$$

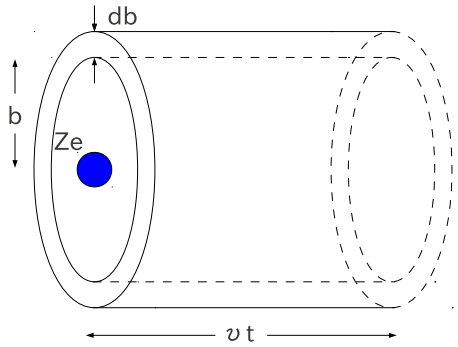

Figure 3.5: The number of electrons with a speed v passing by a stationary ion and having an impact parameter b.

where $g_{ff}(v,\omega)$ is called Gaunt factor:

$$g_{ff}(v,\omega) = \frac{\sqrt{3}}{\pi}\ln(\frac{b_{max}}{b_{min}}). \tag{3.28}$$

Although the speeds of incident electrons are fixed so far, we will consider thermal free-free emission whose velocity has the Maxwell distribution. We average the above single-speed expression over a thermal distribution of velocities. The probability dP of a particle having a particular velocity is

$$dP \propto \mathrm{e}^{-E/kT}d^3\boldsymbol{v} = \exp(\frac{-mv^2}{2kT})d^3\boldsymbol{v} = 4\pi v^2\exp(\frac{-mv^2}{2kT})dv. \tag{3.29}$$

Integrating the emission over all electron speeds gives the total emission per unit volume, but for frequency ν of photon to be emitted, the incident speed must satisfy $mv^2/2 \geq h\nu$, which means the minimum velocity, v_{min}, exists,

$$\frac{dW(T,\omega)}{d\omega dV dt} = \frac{\int_{v_{min}}^{\infty}\frac{dW(v,\omega)}{d\omega dV dt}v^2\exp(-mv^2/2kT)dv}{\int_0^{\infty}v^2\exp(-mv^2/2kT)dv} \tag{3.30}$$

where $v_{min} \equiv (2h\nu/m)^{1/2}$.

The result of the integral is

$$\begin{aligned}
\epsilon_\nu^{ff} &= \frac{dW(T,\omega)}{d\omega dV dt} && (3.31)\\
&= \frac{2^5\pi e^6}{3mc^3}\left(\frac{2\pi}{3km}\right)^{1/2}T^{-1/2}Z^2n_en_i\mathrm{e}^{-h\nu/kT}\overline{g}_{ff} && (3.32)\\
&= 6.8\times10^{-38}Z^2n_en_iT^{-1/2}\mathrm{e}^{-h\nu/kT}\overline{g}_{ff}, && (3.33)
\end{aligned}$$

where $\overline{g}_{ff}$ is a velocity averaged Gaunt factor. By integrating it over frequency, we also obtain the total power per unit volume emitted by thermal free-free emission,

$$\begin{aligned}
\epsilon_\nu^{ff} &= \frac{2^5\pi e^6}{3hmc^3}\left(\frac{2\pi kT}{3m}\right)^{1/2}Z^2n_en_i\overline{g}_B && (3.34)\\
&= 1.4\times10^{-27}Z^2n_en_i\overline{g}_B, && (3.35)
\end{aligned}$$

where $\overline{g}_B$ is a frequency average of the velocity averaged Gaunt factor. The result shows that free-free emission has a rather flat spectrum in a log-log plot up to its cutoff at about $h\nu \sim kT$.

(This is true only for optically thin sources. We have not yet considered absorption of photons by free electrons.)

If we assume that the photon field is in thermal equilibrium with the electrons and ions, we can relate the above result to thermal free-free absorption using Kirchhoff's law as follows,

$$\frac{\epsilon_\nu^{ff}}{4\pi} = j_\nu^{ff} = \alpha_\nu^{ff} B_\nu(T), \tag{3.36}$$

where j_ν^{ff} and α_ν^{ff} are emission and absorption coefficients of free-free emission. With the form of Planck function, we have

$$\alpha_\nu^{ff} = \frac{4e^6}{3mhc}\left(\frac{2\pi}{3km}\right)^{1/2} T^{-1/2} Z^2 n_e n_i \nu^{-3}(1-\mathrm{e}^{-h\nu/kT})\overline{g}_{ff}. \tag{3.37}$$

For $h\nu \gg kT$, the exponential is negligible and $\alpha_\nu \propto \nu^{-3}$. For $h\nu \ll kT$, in the Rayleigh-Jeans regime, we obtain

$$\begin{aligned} \alpha_\nu^{ff} &= \frac{4e^6}{3mkc}\left(\frac{2\pi}{3km}\right)^{1/2} T^{-3/2} Z^2 n_e n_i \nu^{-2}\overline{g}_{ff} & (3.38)\\ &= 0.018 \times T^{-3/2} Z^2 n_e n_i \nu^{-2}\overline{g}_{ff}. & (3.39) \end{aligned}$$

In the R-J regime, $\overline{g}_{ff}(\nu) \propto \nu^{-0.1} T^{0.15}$, so the opacal depth τ_ν is obtained by

$$\tau_\nu = \int \alpha_\nu dl \propto \int T^{-3/2} n_e n_i \nu^{-2}\overline{g}_{ff}(\nu) dl \propto \int T^{-1.35} n_e n_i \nu^{-2.1} dl. \tag{3.40}$$

From the optical depth τ_ν, we can finally obtain the brightness temperature of free-free emission in the R-J regime,

$$T_b = T(1-\mathrm{e}^{-\tau_\nu}) \sim \tau_\nu T \propto \nu^{-2.1}, \tag{3.41}$$

which has a power-law spectrum.

3.3 Thermal dust emission

Thermal dust emission is produced by dust grains absorbing ultra-violet photons from the exciting radiation field of the environment and re-radiating photons thermally. Dust grains are made of silicate and graphite material, coated with ices in cold regions. Thermal emission from dust is common in the ISM of the Milky Way and other galaxies. There is a grain size distribution that has more small grains and fewer large grains with an average size of ~ 0.1 mm. Dust is intermixed with H_2 in molecular clouds, with $M(dust)/M(H_2) \sim 0.01$. The majority of dust emission is from nebulae with ongoing star formation, where the dust is heated by nearby stars. The spectrum of the thermal dust emission is represented by a modified black body function of the form:

$$S_\nu \propto \frac{2h\nu^{3+\beta}}{c^2}\frac{1}{\exp(h\nu/kT_{dust})-1}, \tag{3.42}$$

where β is the dust emissivity spectral index and T_{dust} is the equilibrium temperature of dust grains. In the ISM, the dust temperature varies ranging from ~ 15 K in dense molecular clouds to 25 - 30 K in HII regions. β is also dependent on the physical properties of the dust grains, and it is expected to vary between different environments.

For $h\nu \ll kT_{dust}$, in the Rayleigh-Jeans regime, we obtain

$$S_\nu \propto \nu^{2+\beta}, \tag{3.43}$$

which is a power-law spectrum in this regime.

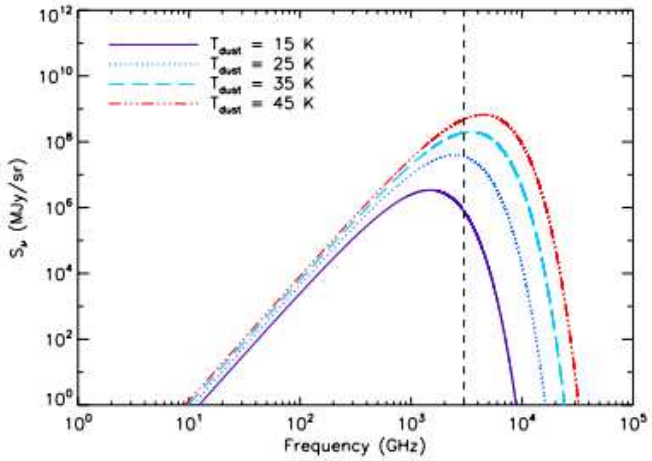

Figure 3.6: The modified black body spectrum representing the thermal dust emission for a range of dust temperatures from 15 to 45 K with a fixed dust emissivity spectral index of 1.8 (Tibbs et al., 2012).

3.4 Spinning dust emission

In some galaxies and our own galaxy, there is recent evidence of so-called anomolous radio emission plausibly from spinning dust. Draine & Lazarian (1998) proposed that very small grains containing 10 - 100 carbon atoms could be spun up to tens of GHz frequencies in the ISM. Electric dipole moments from spinning dust grains implies they are likely to produce radio emission at these freuqencies with the spectrum depending on the conditions in the local ISM. So in addition to free-free, thermal and synchrotron emission, spinning dust emission is a fourth component that is present in radio emission from other external galaxies and our own Milky Way. The spinning dust emission mechanism may be understood by assuming equipartition in

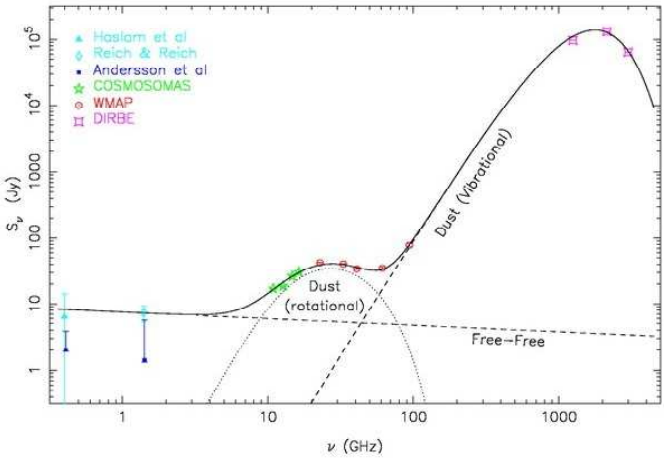

Figure 3.7: Spectrum of G159.6-18.5 (Watson et al., 2005).

the rotational degrees of freedom:

$$\frac{1}{2}I\omega^2 = kT. \tag{3.44}$$

For a spherical and homogeneous grain, with $I = \frac{2}{5}mR^2$, a radius $R = N \times 10^{-10}(m)$, and a mass density $\rho = 1(kgm^{-3})$, the rotation frequency is

$$\nu = 6.5 \times 10^3 \sqrt{\frac{T}{N^5}} \ (GHz). \tag{3.45}$$

A typical dust temperature is $T \sim 10^2(K)$, and a very small grain cannnot be much less than 100 atoms in radius (so $N = 10^2$), therefore $\nu \sim 1GHz$.

According to Ali-Haimoud et al. (2009) and Silsbee et al. (2011), current spinning dust models incorporate a variety of grain rotational excitation and damping processes: collisions with neutral and ionised gas particles, plasma drag (the interaction between the electric field of ions and the electric dipole moment of the dust grains), absorption and emission of a photon, the photoelectric effect, microwave emission and the formation of H_2 on the grain surface. In regard to the emission from these complicated processes, the peak frequency of the spinning dust spectrum is determined by that of the smallest grains, and that the total power follows the same dependence upon environmental parameters as the power emitted by the smallest grains.

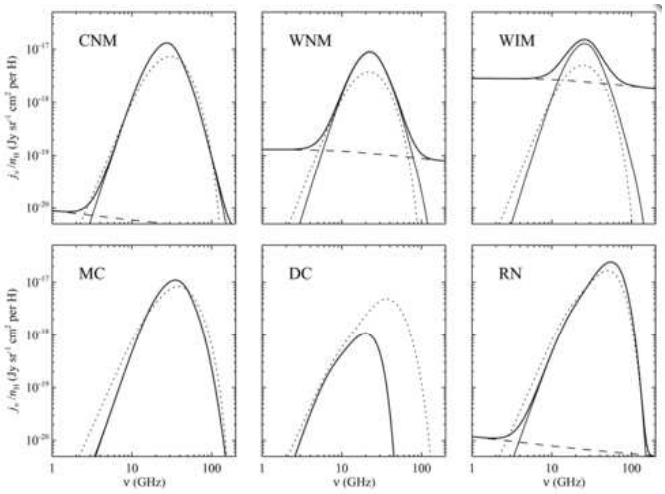

Figure 3.8: Spinning dust spectra for several environmental conditions: cold neutral medium (CNM), warm neutral medium (WNM), warm ionized medium (WIM), molecular cloud (MC), dark cloud (DC) and reflection nebula (RN) (Ali-Haimoud et al., 2009).

Chapter 4

Experiment Simulations

In this chapter, we shall simulate the 10 GHz map using the available template maps of synchrotron, free-free, thermal-dust, spinning dust emission and CMB including an estimated noise. We then simulate observations of the sky with a wide-band 10 GHz receiver taking scanning observation of the sky from Penticton BC. With the simulated 10 GHz map, we will evaluate the efficiency of the foreground removal with other available data such as Haslam 408 MHz map (Haslam et al., 1981) and 5 WMAP maps at 23, 33, 41, 61 and 94 GHz (Bennett et al., 2012).

4.1 Field of view

Here, we will verify the field of view of the telescope in the galactic coordinates. In the project, the telescope is proposed to rotate with an opening angle 40° from the zenith at Penticton at a rotation rate of 1 (rot/min) as see in Fig. 4.1.

First, we will transfer the line of sight from the telescope coordinates to the Penticton coordinates. With the Euler angles, the coordinates are transfered by

$$\begin{pmatrix} x_t \\ y_t \\ z_t \end{pmatrix} = R_z(\psi)R_x(\theta)R_z(\phi) \begin{pmatrix} x_p \\ y_p \\ z_p \end{pmatrix} \tag{4.1}$$

$$= \begin{pmatrix} \cos\psi & \sin\psi & 0 \\ -\sin\psi & \cos\psi & 0 \\ 0 & 0 & 1 \end{pmatrix} \begin{pmatrix} 1 & 0 & 0 \\ 0 & \cos\theta & \sin\theta \\ 0 & -\sin\theta & \cos\theta \end{pmatrix} \begin{pmatrix} \cos\phi & \sin\phi & 0 \\ -\sin\phi & \cos\phi & 0 \\ 0 & 0 & 1 \end{pmatrix} \begin{pmatrix} x_p \\ y_p \\ z_p \end{pmatrix} \tag{4.2}$$

where $(x_t,y_t,z_t) = (0,\ 0,\ 1)$ is in the telescope coordinates and (x_p,y_p,z_p) is in the Penticton coordinates, and where a precession opening angle $\psi = 40°$, a precession angle $\theta = 360° \times t(\text{sec})/60(\text{sec})$ and a spin angle $\phi = 0°$.

Next, we transfer the line of sight from the Penticton coordinates to the earth coordinates. Since Penticton is located at the latitude, 49°29′ N, the direction of the telescope in the earth coordinates is given by

$$\begin{pmatrix} x_p \\ y_p \\ z_p \end{pmatrix} = R_y(90° - \theta) \begin{pmatrix} x_e \\ y_e \\ z_e \end{pmatrix} \tag{4.3}$$

$$= \begin{pmatrix} \cos(90° - \theta) & 0 & -\sin(90° - \theta) \\ 0 & 1 & 0 \\ \sin(90° - \theta) & 0 & \cos(90° - \theta) \end{pmatrix} \begin{pmatrix} x_e \\ y_e \\ x_e \end{pmatrix}, \tag{4.4}$$

where (x_e,y_e,z_e) is in the earth coordinates and $\theta = 49.5°$.

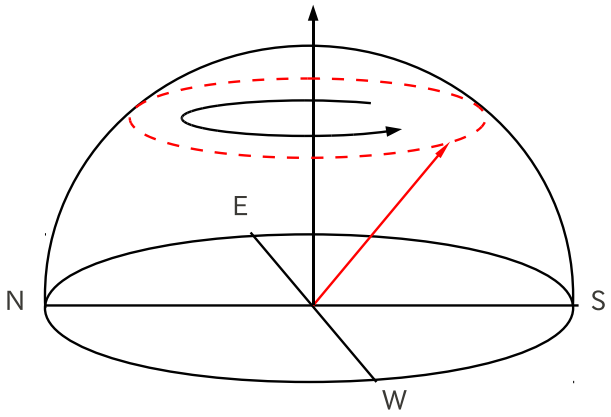

Figure 4.1: The path of the telescope direction in the Penticton coordinates. (Red arrow)The line of sight of the telescope.

The third step is to transfer the line of sight from Earth coordinates to the celestial coordinates. The earth spins around its axis once a day based on the sidereal time, which is the time it takes the earth to make one rotation relative to the vernal equinox. A mean sidereal day is 23 hours, 56 minutes, 4.0916 seconds, a little shorter than the solar time.

$$\begin{pmatrix} x_e \\ y_e \\ z_e \end{pmatrix} = R_z(LST) \begin{pmatrix} x_c \\ y_c \\ z_c \end{pmatrix} \tag{4.5}$$

$$= \begin{pmatrix} \cos(LST) & \sin(LST) & 0 \\ -\sin(LST) & \cos(LST) & 0 \\ 0 & 0 & 1 \end{pmatrix} \begin{pmatrix} x_c \\ y_c \\ x_c \end{pmatrix}, \tag{4.6}$$

where (x_c,y_c,z_c) is in the celestial coordinates, and LST, a local sidereal time, is given by

$$LST(\text{deg}) = 360^\circ \times \text{frac}(0.671262 + 1.00273790935 \times (\text{MJD} - 40000) + \frac{\text{longitude}}{360^\circ}) \tag{4.7}$$

where longitude is -119.6° at Penticton, MJD stands for Modified Julian Date, and "frac" represents the decimal part of the result.

The final step is to transfer the line of sight from the celestial coordinates to the galactic coordinates. The right ascension and declination of the galactic center is 266.40500 deg and -28.93617 deg, so the rotation along the z-axis by 266.40500° and along the y-axis by 28.93617° points the galactic center. In addition, the rotation along the x-axis by 58.59866° determines the angle of the galactic place, so

$$\begin{pmatrix} x_g \\ y_g \\ z_g \end{pmatrix} = R_x(\psi)R_y(\theta)R_z(\phi) \begin{pmatrix} x_c \\ y_c \\ z_c \end{pmatrix} \tag{4.8}$$

$$= \begin{pmatrix} 1 & 0 & 0 \\ 0 & \cos\psi & \sin\psi \\ 0 & -\sin\psi & \cos\psi \end{pmatrix} \begin{pmatrix} \cos\theta & 0 & -\sin\theta \\ 0 & 1 & 0 \\ \sin\theta & 0 & \cos\theta \end{pmatrix} \begin{pmatrix} \cos\phi & \sin\phi & 0 \\ -\sin\phi & \cos\phi & 0 \\ 0 & 0 & 1 \end{pmatrix} \begin{pmatrix} x_c \\ y_c \\ z_c \end{pmatrix} \tag{4.9}$$

where (x_g,y_g,z_g) is in the galactic coordinates, and where $\psi = 58.59866^\circ$, $\theta = 28.93617^\circ$ and $\phi = 266.40500^\circ$.

With this sequence of transformations, we can obtain the direction of the telescope in the galactic coordinates at any time. Fig. 4.2 and Fig. 4.3 show the hit maps of one-day observation in the celestial and galactic coordinates. 42% of all the sky is covered with this strategy.

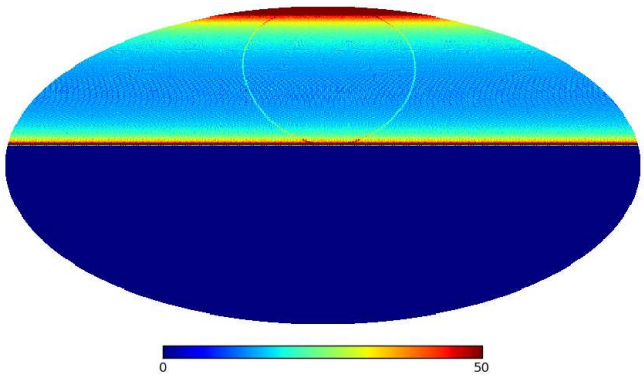

Figure 4.2: The hitmap of one day observation in the celestial coordinates ($N_{side} = 128$).

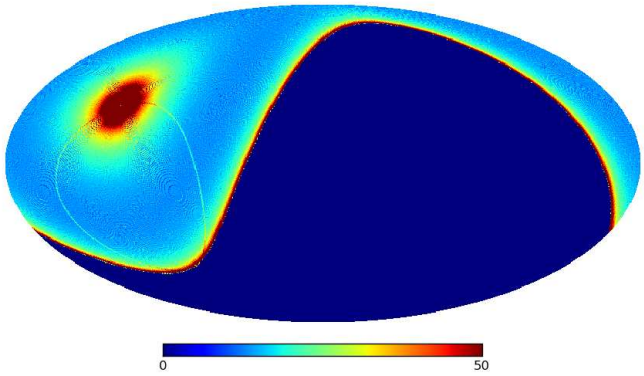

Figure 4.3: The hitmap of one day observation in the galactic coordinates ($N_{side} = 128$).

4.2 Simulated sky map at 10 GHz

Next, we will prepare for the template maps of five known components in the microwave range: synchrotron, free-free, thermal dust, spinning dust emission and CMB to simulate the 10 GHz sky map.

4.2.1 Synchrotron emission map

Synchrotron emission arises from the acceleration of cosmic-ray electrons in magnetic fields. The emission becomes stronger as the energy and the number density of electrons increase as well as the magnetic field. Since the number density of relativistic electrons changes with $N(E) \propto E^{-\gamma}$, the emission is dominant at low frequency as seen in Fig. 3.1. Fig. 4.4 is the radio emission map at 408 MHz by Haslam et al. (1981), which is dominated by synchrotron emission and commonly used as a synchrotron emission template. We adopt this map as a synchrotron emission model map.

The spectral index of synchrotron emission has a complicated feature. It has a steeper value at higher frequencies, $\beta_s \sim 2.4 - 2.55$ between 22 and 408 MHz (Roger et al., 1999) to $\beta_s \sim 2.8$ between 1.4 and 7.5 GHz (Platania et al., 1998). It also has a dependance on galactic latitudes, which is flatter in the plane ($\beta_s \sim -2.5$) and steeper off the plane ($\beta_s \sim -3.0$) (Bennett et al., 2003). The spectral index map between 408 MHz and 23 GHz provided by Bennett et al. (2003) can be used as a synchrotron spectral index map(Fig. 4.5), but the contamination level of other components such as free-free emission and spinning dust emission in the WMAP 23 GHz map is not accounted for.

Therefore, we adopt the HI column density map (Dickey & Lockman, 1990; Hartmann & Burton, 1997) to simulate the synchrotron spectral index map that is independent of the WMAP data (Fig. 4.6). This map has a similar distribution to the map provided by Bennett et al. (2003). We adjust the scale by a factor of $\beta_s = (\frac{\log_{10}|HI(p)|}{6} - 6.25)$ so that its range becomes between -3.0 and -2.5, where $|HI(p)|$ is a absolute value of each pixel in the HI column density map. We assume that the synchrotron spectral index is constant in the frequency range that we target, in a given pixel. While this model is not perfect, it does resemble the known spectral variations.

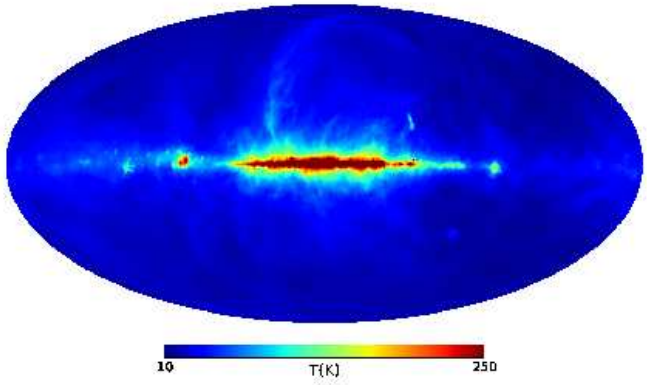

Figure 4.4: Haslam 408 MHz map (Haslam et al., 1981), largely dominated by synchrotron emission.

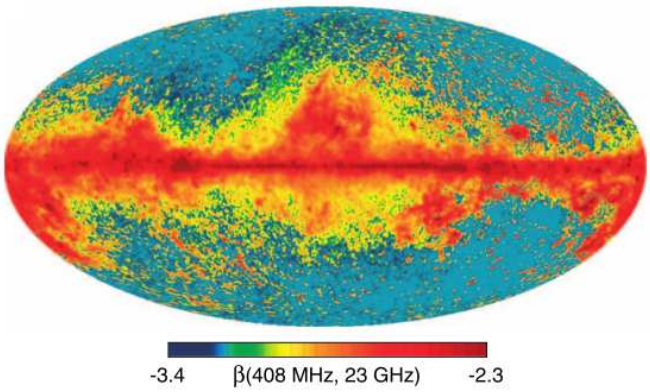

Figure 4.5: Spectral index map of β_s made from 408 MHz and 23 GHz map, showing the flatter spectral index ($\beta_s \sim$ -2.5) regions of active star formation in the plane, where the cosmic-ray electrons are generated. The steeper spectral index regions ($\beta_s \sim$ -3) off the plane suggest the energy losses suffered by the cosmic-ray electrons during the period of time required for their diffusion away from the star formation regions of their origin. This spectral index map is dominated by synchrotron emission but still contains free-free emission (Bennett et al., 2003).

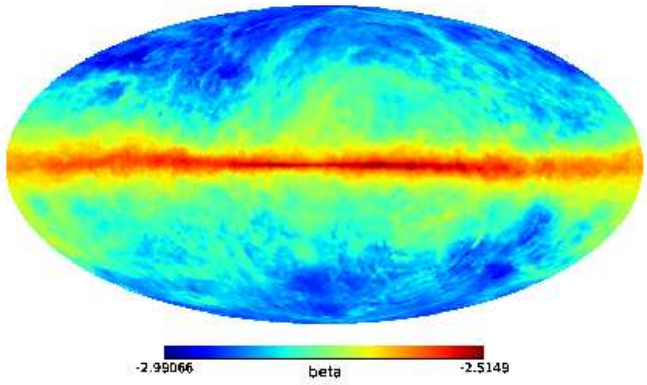

Figure 4.6: HI column density map for varying β_s. The scale is changed by $\beta_s = (\log_{10}|HI(p)|)/6-6.25)$ to use as a spectral index distribution map.

4.2.2 Free-free emission map

Free-free emission arises from electron-iron scattering. Free-free thermal emission has $T_b \sim \nu^{\beta_f}$ with β_f = -2.15 at high frequency ($\nu > 1$ GHz) and $T_b \sim \nu^2$ at low frequency.

Radio astronomy does not have a free-free emission model map because free-free is not dominant at any radio frequency. Since free-free thermal emission is produced by free electrons scattering off ions in HII clouds, it should have a strong correlation with the optical map of Hα emission. The full-sky Hα map (hydrogen $n = 3 \rightarrow 2$) is provided by Finkbeiner et al. (2003), but the intensity of the Hα has to be transformed into the brightness temperature of the free-free emission. Its conversion factor is discussed in Bennett et al. (2003), and we adopt this value to make a free-free emission model map. This model does not account for optical extinction of Hα in the plane, which does not affect the free-free emission.

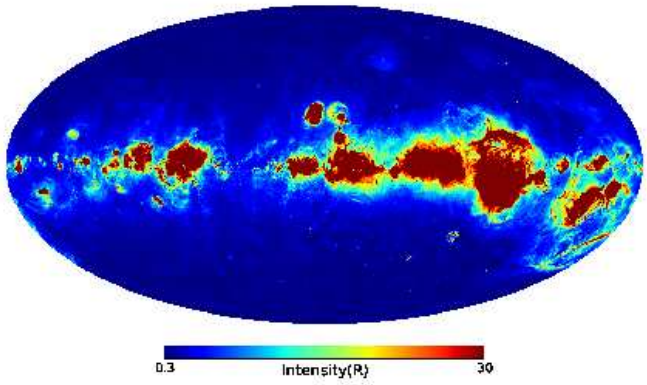

Figure 4.7: Hα map (Finkbeiner et al., 2003). The unit of the map is rayleighs ($1R = 2.42 \times 10^{-7} ergs\ cm^{-2} s^{-1} sr^{-1} at\ 0.6563 \mu m$).

4.2.3 Thermal dust emission map

Thermal dust emission has been mapped over the full sky in several infrared band by IRAS and COBE missions. Finkbeiner, Davis & Schlegel (D. Finkbeiner , 1999) developed models to predict submillimeter and microwave dust emission, based on fits to data from their earlier 100μm and 100/240μm maps and extension to COBE/FIRAS frequencies. We adopt this map as a thermal dust emission model map.

Measurements of the thermal dust spectral index generally lie in the range $1.5 \leq \beta_d \leq 2.0$. Planck Collaboration. (2011) constructed an all sky map of the the apparent temperature and optical depth of thermal dust emission using the Planck-HFI (350 μm to 2 mm) and IRAS(100 μm) data. They indicate that a thermal dust has a power law distribution with a mean emissivity spectral index of 1.8, which is the value derived from the galactic solar neighbourhood. We utilize this value as a spectral index of the thermal dust emission.

4.2.4 Spinning dust emission map

There is no reliable measurement of spinning dust emission over the full sky, but the detail emission mechanism has been studied in Ali-Haimoud et al. (2009) and Silsbee et al. (2011). A code to calculate spinning dust spectra for the nominal physical conditions that they adopted for different ISM environments (cold neutral medium (CNM), warm neutral medium (WNM), warm ionized medium (WIM), molecular cloud (MC), photodissociation region (PDR), reflection

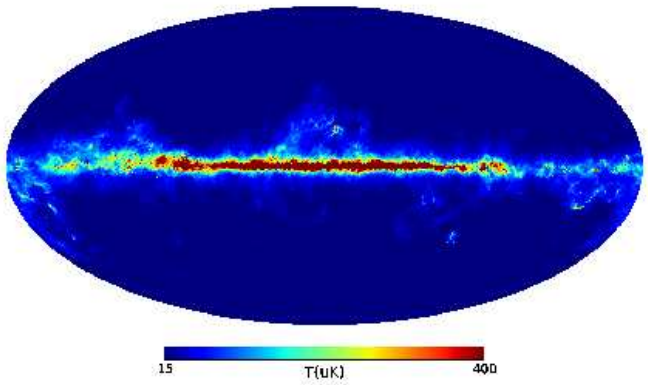

Figure 4.8: FDS dust map at 94 GHz based on data from IRAS and COBE (D. Finkbeiner , 1999).

nebula (RN), and dark cloud (DC)) is provided by the authors. With the theoretical model, Bennett et al. (2012) has shown the spinning dust emissivity spectra and the same spectra normalized to a peak of unity and scaled to a common peak frequency (that of the CNM spectrum, 17.8 GHz).

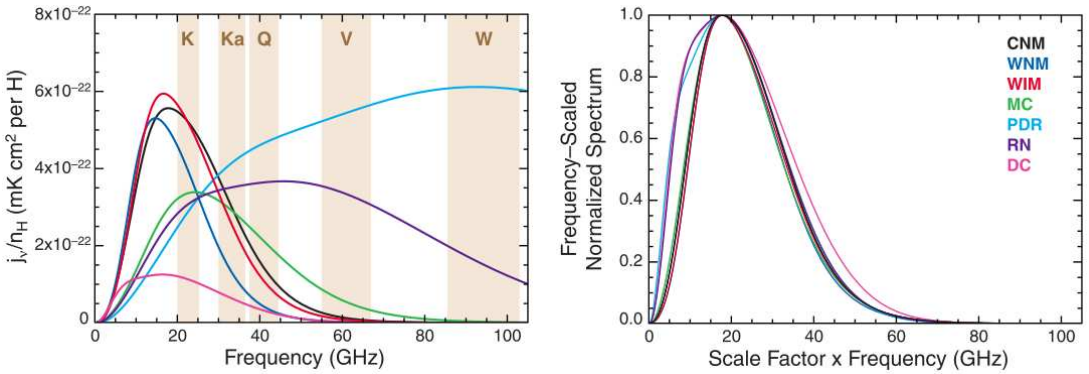

Figure 4.9: Spinning dust emissivity spectra predicted by the model by Ali-Haimoud et al. (2009) and Silsbee et al. (2011) (Bennett et al., 2012).

We assume that the spinning dust spectrum has a simple gaussian distribution,

$$T_b(\nu) = A_{sd} \times \exp\left[-\frac{1}{2}\left(\frac{a_{sd}\cdot\nu - \nu_{sd}}{\sigma_{sd}}\right)^2\right], \tag{4.10}$$

where the center and the width of the spectra, ν_{sd} and σ_{sd}, are 18 GHz and 10 GHz. We also assume that the amplitude, A_{sd}, is 50 % of the total emission at 23 GHz and a_{sd} has the value between 0.5 and 1.0, which shifts the emission peak to $18/a_{sd}$ (GHz) and the width to $10/\sigma sd$ (GHz) as seen in Fig. 4.10.

4.2.5 Cosmic Microwave Background map

The code to make a CMB anisotropy map given a set of input cosmological parameters is provided by the LAMBDA website (http://lambda.gsfc.nasa.gov/toolbox/tb_cmb_form.cfm). We simulate a model CMB anisotropy map by the default cosmological parameters set in the website.

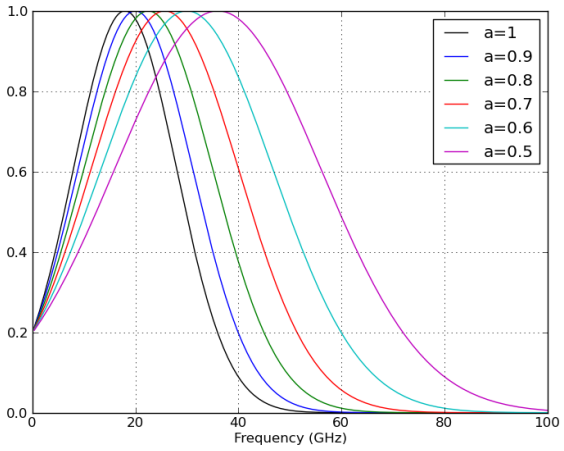

Figure 4.10: Spinning dust normalized model spectra.

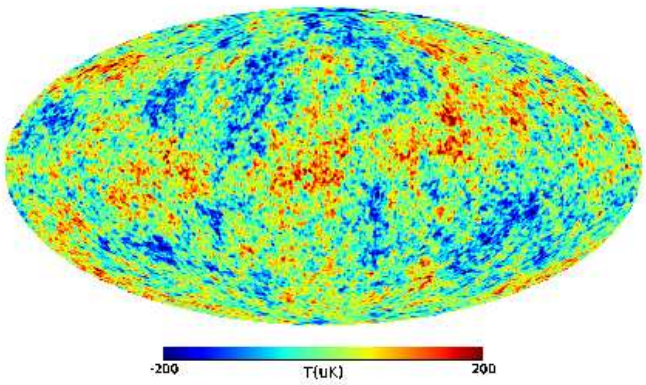

Figure 4.11: Cosmic Microwave Background Anisotropy map (LAMBDA).

4.2.6 Simulated sky maps

Now we have all the model maps, spectral indexes of five known components in the microwave range: synchrotron, free-free, thermal dust, spinning dust emission and CMB. Using all these components, we simulate sky maps at 0.408, 10, 23, 33, 41, 61, and 94 GHz.

$$T_{model}(\nu,p) = T_s(p) * \left(\frac{\nu}{0.408}\right)^{\beta_s(p)} + T_{ff}(p) * \left(\frac{\nu}{23}\right)^{-2.15} + T_d(p) * \left(\frac{\nu}{94}\right)^{1.8} + A_{sd}(p) \times \exp\left[-\frac{1}{2}\left(\frac{a_{sd}(p)\cdot\nu - 18}{10}\right)^2\right] + T_{CMB}(p), \tag{4.11}$$

where $T_{ff} = I_{H\alpha}(p) * 11.4$ (conversion factor), and subscripts s, ff, d, sd and CMB represent the synchrotronn, free-free, thermal dust, spinning dust and CMB respectively in pixel p. (At first, we do not include the spinning dust emission because the emission is negligible in most of the frequencies we simulate.)

We use this map to generate simulated observation with a 10 GHz receiver to evaluate calibration and de-striping algorithms as part of the proposed data reduction pipeline.

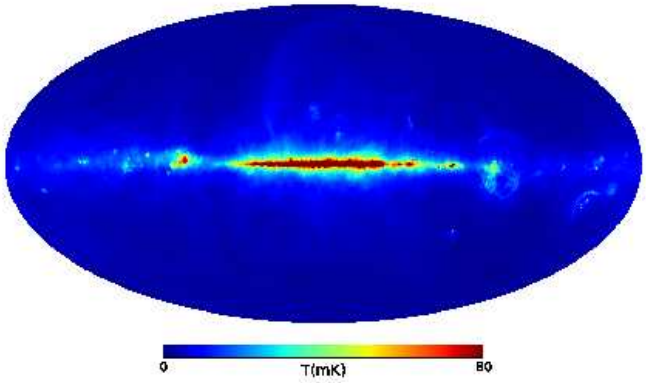

Figure 4.12: Simulated 10 GHz sky map.

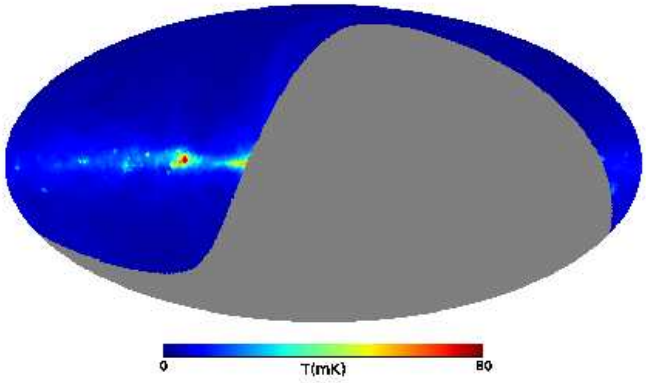

Figure 4.13: Simulated 10 GHz sky map in the field of view.

4.3 Calibration

Raw data obtained by the detector is in volts(V), so it has to be transformed to a sky temperature(K) to analyze the physical condition of each emission component. To obtain the correct gain[V/K] of the detector, we can utilize a radio emission whose property is well known. One way is to observe a well-known radio point source at the same time and the other way is to utilize the CMB dipole anisotropy included in the raw data.

The CMB dipole anisotropy is the result of the Doppler shift caused by the earth's 627 ± 22 (km/s) motion relative to the CMB rest frame in the direction of galactic longitude ($l = 276 \pm 3°, b = 30 \pm 3°$) with amplitude 3.346 ± 0.017 (mK) (Scott & Smoot et al., 2004). This method is favorable because we do not need an extra observation only to obtain the detector's gain.

In this chapter, we will check whether the CMB dipole can be utilized for the calibration or not. Here, for the calibration test, we simulate that the true gain is 1V/1K and check whether this true gain can be recovered from the raw data including an expected white noise,

$$\Delta T = \frac{T_{sys}}{\sqrt{\Delta\nu\tau}} = \frac{50}{\sqrt{2 \times 10^9 * 0.05}} = 5(\text{mK}) \ \ (\text{per 50 ms sample}), \tag{4.12}$$

where $T_{sys} = 50$ (K), $\Delta\nu = 2 \times 10^9$ (Hz) and $\tau = 0.05$ (sec).
(Here, 1/f noise is not included. The reduction of the 1/f noise will be described in Sec. 4.4.

Now, we know the direction of the telescope at any time, the brightness temperature of the direction, and the gain of the detector, so we can simulate a time-ordered data when the

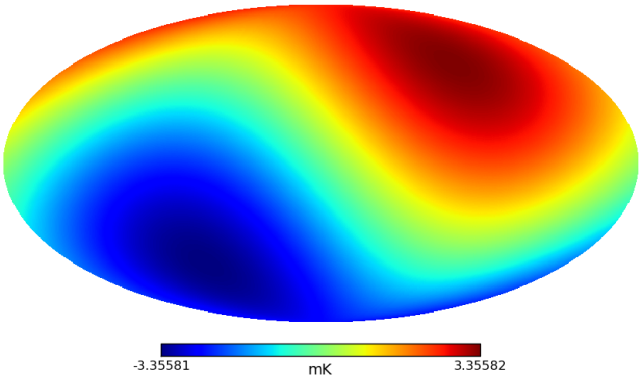

Figure 4.14: Simulated CMB Dipole map.

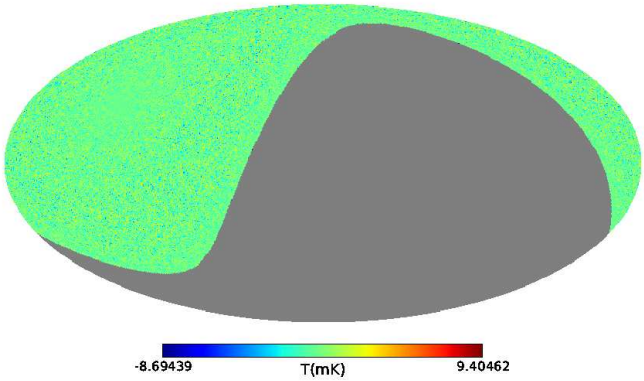

Figure 4.15: Simulated white noise map with amplitude 5 mK.

telescope observes the 10 GHz sky at the time inverval 0.05 sec (Fig. 4.16). Here, the raw data includes

$$T_{model}(\nu,p) = T_s(p) * \left(\frac{\nu}{0.408}\right)^{\beta_s(p)} + T_{ff}(p) * \left(\frac{\nu}{23}\right)^{-2.15} + T_d(p) * \left(\frac{\nu}{94}\right)^{1.8} + T_{CMB}(p) + T_{CMB\_dip}(p) + T_{wnoise}(p). \tag{4.13}$$

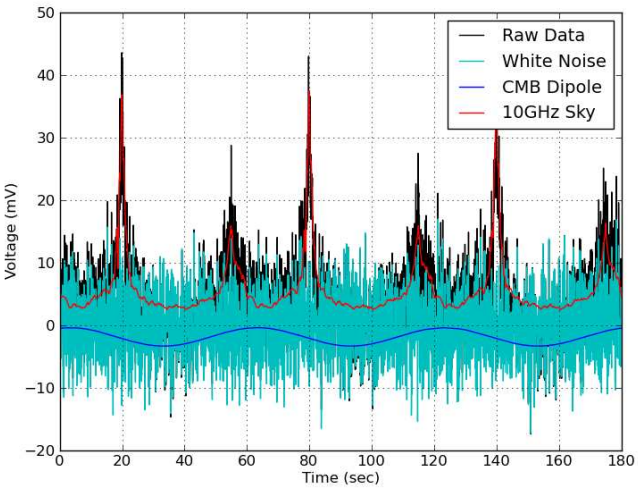

Figure 4.16: Time-ordered data at 10 GHz (The data is taken at the 0.05 sec interval).

4.3.1 The method to obtain a gain with CMB dipole and raw data

We can utilize the relationship between the raw data and the CMB dipole to obtain the true gain from the raw data. A point which has higher CMB dipole would have higher temperature by its amplitude and vice versa. Therefore, 2D plot of the CMB dipole and raw data should give us the true gain as a slope (Fig. 4.17).

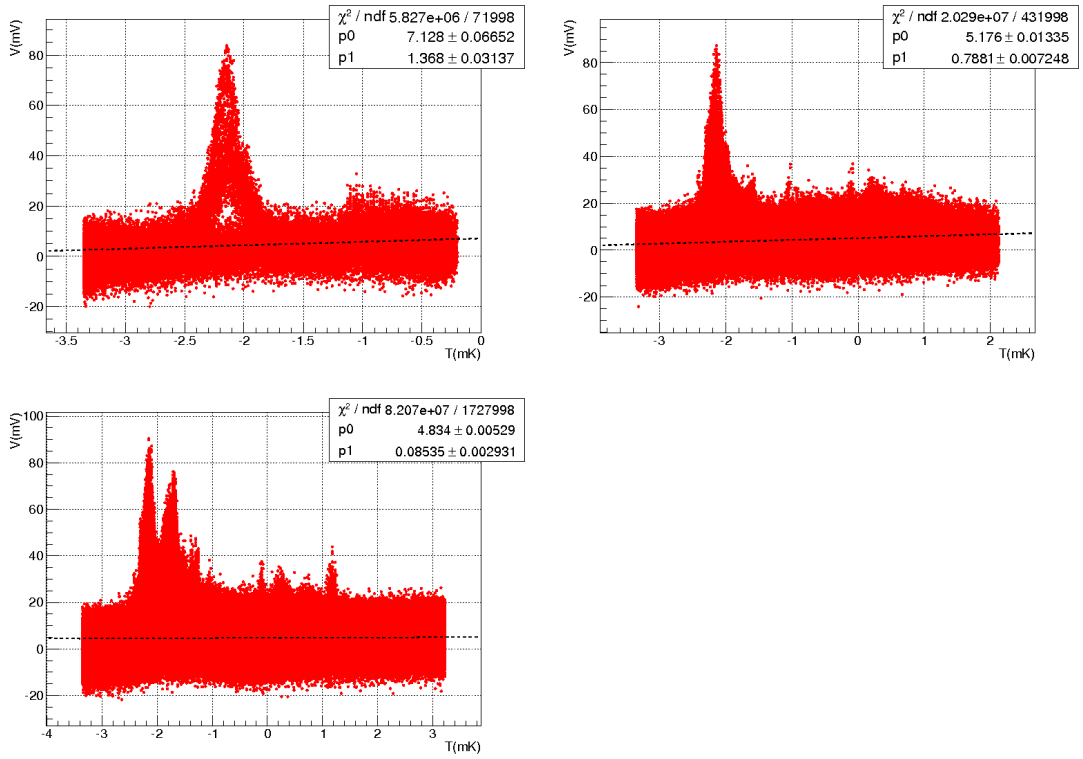

Figure 4.17: 2D plot of CMB Dipole vs Raw data. (Upper left: 1 hour data, Upper right: 6 hour data, Lower left: 24 hour data)

Data period	Gain (slope) [V/K]
1 hour	1.38 ± 0.031
6 hours	0.788 ± 0.007
24 hours	0.085 ± 0.003

Table 4.1: Fit gain(slope) by the linear fit for the true gain 1.0.

The fit gain by the linear fit of the 2D plot for the different period (1 hour, 6 hours and 24 hours) of data is summarized in Tab. 4.1. The data along the galactic plane has a stronger signal and it has an effect to get a smaller slope than the expected one. This effect is more clear in the longer period of data. To avoid the effect, we will cut the data along the galactic plane within the galactic latitude 15°.

After the galactic plane cut, the fit gain by the linear fit is summarized in Tab. 4.2. The effect of the strong signal from the galactic plane has dissapeared (Fig. 4.18), but the correct gain can not be obtained. We will try to utilize the CMB dipole more effectively by using the CMB dipole map as a correction as follows.

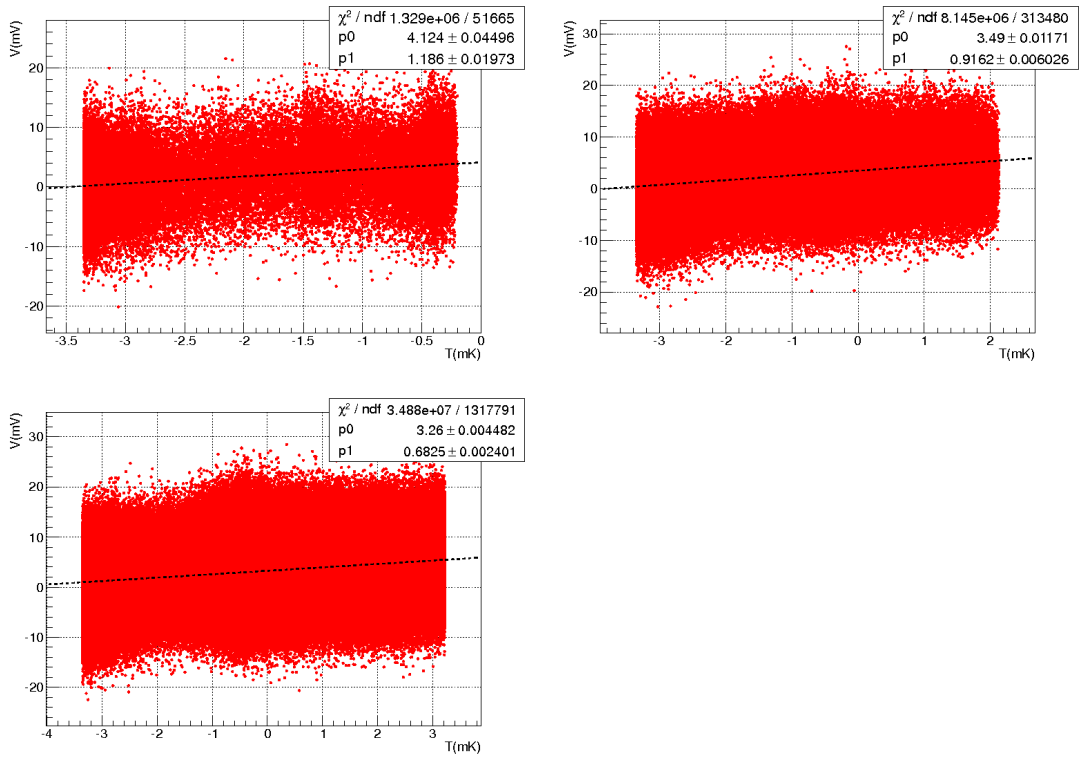

Figure 4.18: 2D plot of CMB Dipole vs Raw data with with the galactic cut within the 15° latitude. (Upper left: 1 hour data, Upper right: 6 hour data, Lower left: 24 hour data)

Data period	Gain [V/K]
1 hour	1.186 ± 0.020
6 hours	0.916 ± 0.006
24 hours	0.683 ± 0.002

Table 4.2: Fit gain by the linear fit with the galactic cut within the 15° latitude.

Raw data includes the galactic emission and CMB dipole,

$$V = g_{true} \times T_{all} \tag{4.14}$$
$$= g_{true} \times (T_{gal} + T_{CMB\_dip}). \tag{4.15}$$

where g_{true} is a true gain, which follows that T_{all}, T_{gal} and T_{CMB_dip} are all true.
From the linear fit of the CMB dipole and raw data, we obtain the gain, g_1, which might be incorrect.

$$V = g_1 \times T_1, \tag{4.16}$$

where $T_1 = T_{gal1} + T_{CMB\_dip1}$.
With the fit gain, g_1, we produce a temperature map, T_1 map,

$$T_1 = \frac{V}{g_1}. \tag{4.17}$$

The dipole component in the T_1 map can be extracted by projecting it to the unit CMB dipole vector,

$$T_{dip1} = |d| \times \hat{d}, \tag{4.18}$$

where $|d| = (T_1 \cdot \vec{d})/(\vec{d} \cdot \vec{d})$ ($\vec{d}$: unit CMB dipole vector).
We replace the extracted dipole component in T_1 map with the correct CMB dipole map.

$$T_1' = T_1 - T_{dip1} + T_{CMB\_dip} \tag{4.19}$$

With the T_1' map that has the correct CMB dipole, we simulate another raw data, V_1, and then acquire another gain, g_2, from the 2D plot of CMB Dipole and V_1.

$$V_1 = g_2 \times T_1' \tag{4.20}$$

By repeating the steps, the CMB dipole component is corrected at every iteration and the gain should approach to the true value.

In case of 1 hour, 6 hours, and 24 hours data, the acquired gain and $|d|$ value after each iteration are summarized in Fig. 4.19. In all the cases, the correct gain can not be acquired. It is considered that the reason is caused by the asymmetric field of view in our project. It is clearly seen from the fact that $|d|$ has a negative value in a shorter period of data. When we try to extract the CMB dipole from the T_1 map, we also extract the dipole component by the galactic emission that comes from the asymmetic field of view.

In conclusion, the CMB dipole can not be utilized for the reliable calibration in our project. We will need to employ another, external calibration source such as a noise diode that is switched into the signal path. This will let us determine relative calibration as a function of time. Absolute calibration may be set by observing a known bright radio source, such as Cas A or perhaps the CMB dipole.

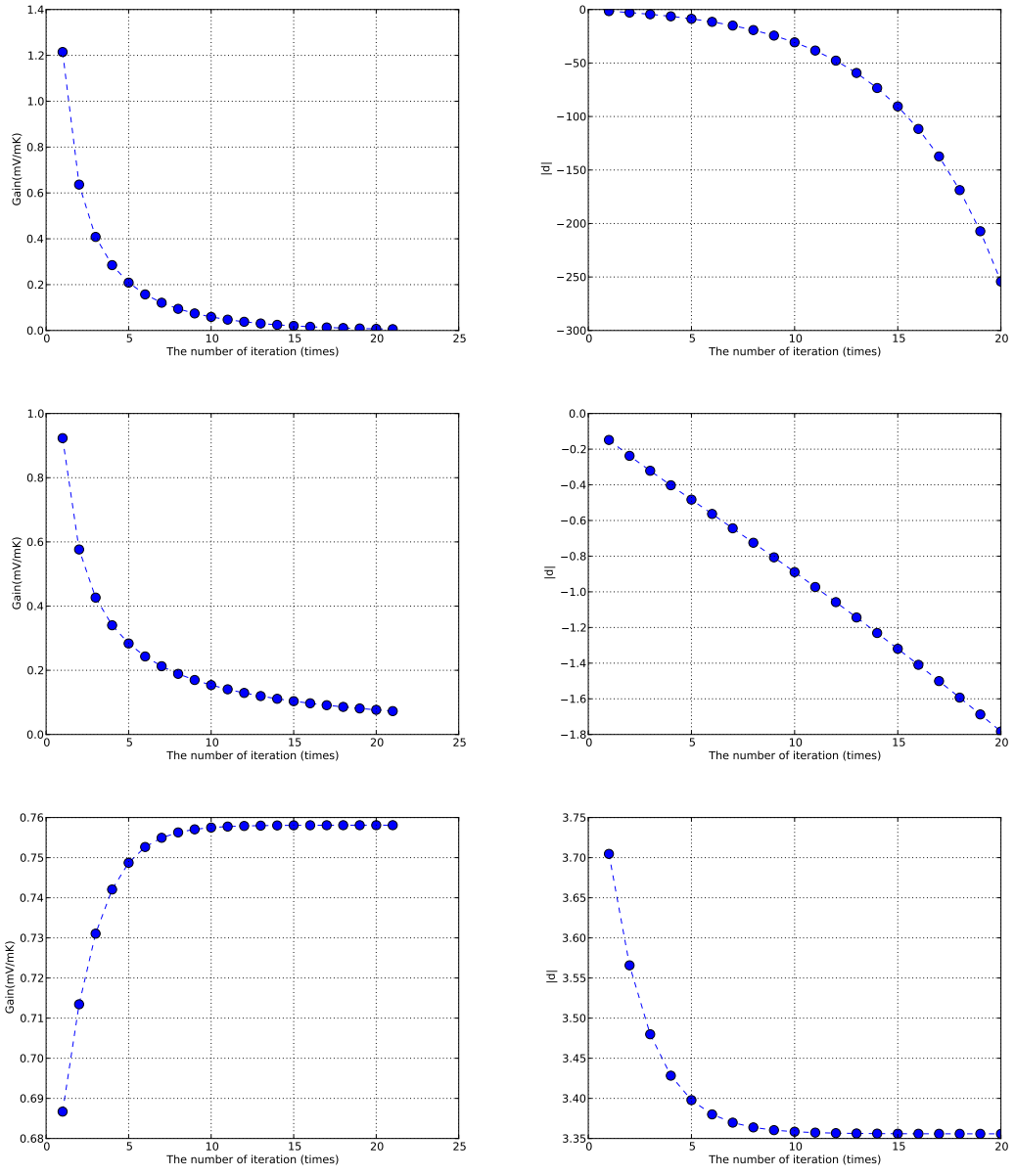

Figure 4.19: Acquired gain(left column) and $|d|$ value(left column) after each iteration. (Top row: 1 hour data, Middle row: 6 hour data, Bottom row: 24 hour data)

4.4 Reduction of 1/f noise

Only white noise was considered so far, but there is also correlated 1/f noise in the raw data. We shall introduce the method to reduce the 1/f noise from the raw data. Here we study a de-striping algorithm to help reduce 1/f noise stripes in the sky map.

4.4.1 1/f noise

A noise level of white noise is still set 5 mK. The amplitude of 1/f noise is adjusted so that the powers of both noises match at 10^{-1} Hz, a typical value for a 10 GHz HEMT-based receiver.

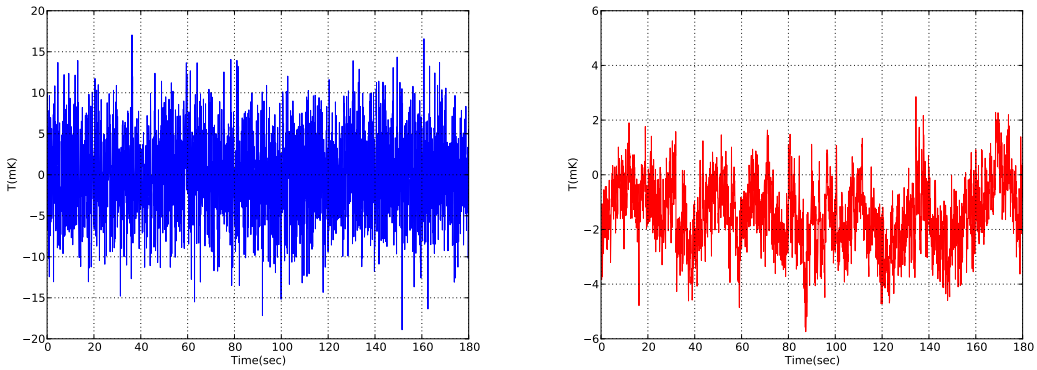

Figure 4.20: Time-ordered white noise(left) and 1/f noise(right).

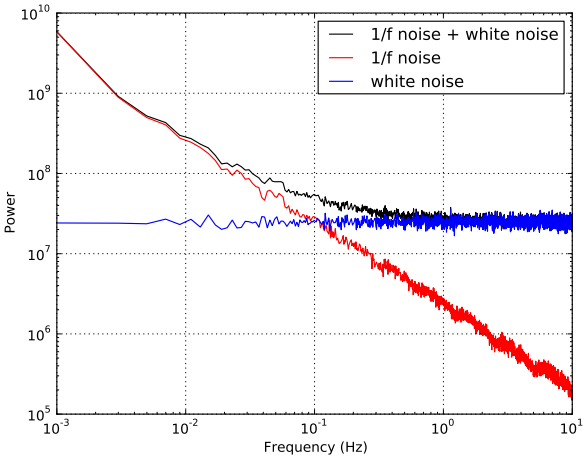

Figure 4.21: Power of white noise and 1/f noise.

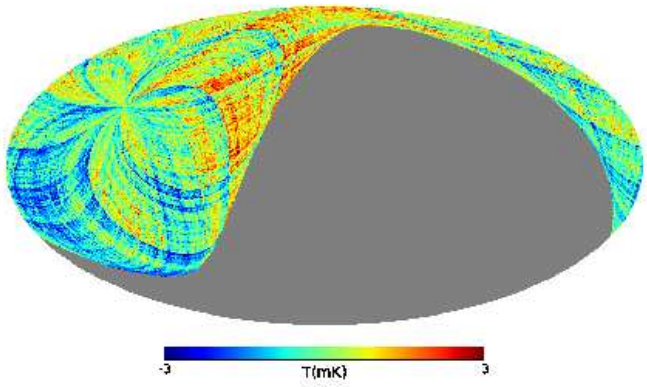

Figure 4.22: 1/f noise map in the galactic coordinates.

4.4.2 Baseline reduction method of 1/f noise

As seen in Fig. 4.2 and Fig. 4.3, the telescope passes through the north celestial pole and the corresponding galactic region every minute. This property can be exploited to reduce 1/f noise. Since the sky temperature around the north celestial pole is fixed, the difference in the amplitude between successive passes should come from noise. If there is a trend in the NCP(North celestial pole) passes, it should be caused by 1/f noise because white noise has no temporal correlation (Fig. 4.23).

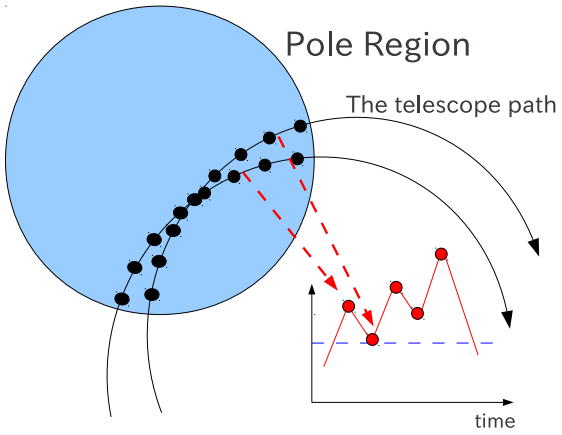

Figure 4.23: The method to reduce 1/f noise map.

Here, we use the raw data including

$$T_{model}(\nu,p) = T_s(p) * \left(\frac{\nu}{0.408}\right)^{\beta_s(p)} + T_{ff}(p) * \left(\frac{\nu}{23}\right)^{-2.15} + T_d(p) * \left(\frac{\nu}{94}\right)^{1.8} + T_{CMB}(p) + T_{wnoise}(p) + T_{fnoise}(p), \tag{4.21}$$

and set the region in 3° radius from the north celestial pole as the pole region.

First, to extract 1/f noise from the raw data, we pick up the time-ordered data when the telescope passes through the celestial pole region every minute, (blue data in Fig. 4.24), then take the average (red points in Fig. 4.24), and interpolate the data between each averaged data

by linear line (red line in Fig. 4.24). Lastly, we subtract the constant pole temperature from the linear line and can obtain the red line in Fig. 4.25. We call it "baseline", which estimates the 1/f noise component in the raw data.

We compare the baseline derived from the raw data with the one from the input 1/f noise (Fig. 4.25). The deviation between these baselines is 0.883 (mK) compared to the rms of the input 1/f noise, 1.732 (mK). The correlation in the 1/f noise is extracted within the rms error.

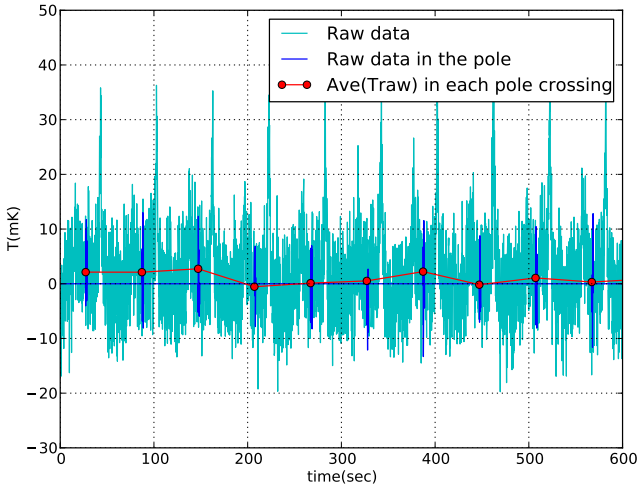

Figure 4.24: Time-ordered raw data and the data in the pole region. (cyan)Time-ordered raw data, (blue)The data in the pole region, and (red)Each average temperature in the pole region

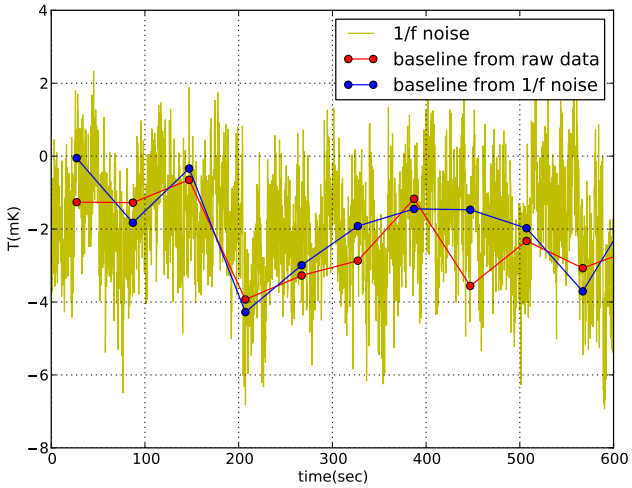

Figure 4.25: Time-ordered input 1/f noise and the baselines from the raw data and the input 1/f noise.

We apply the baseline reduction to the input 1/f noise for one day data. It is clearly seen that the correlation in the input 1/f noise is reduced after the baseline reduction as seen in Fig. 4.26.

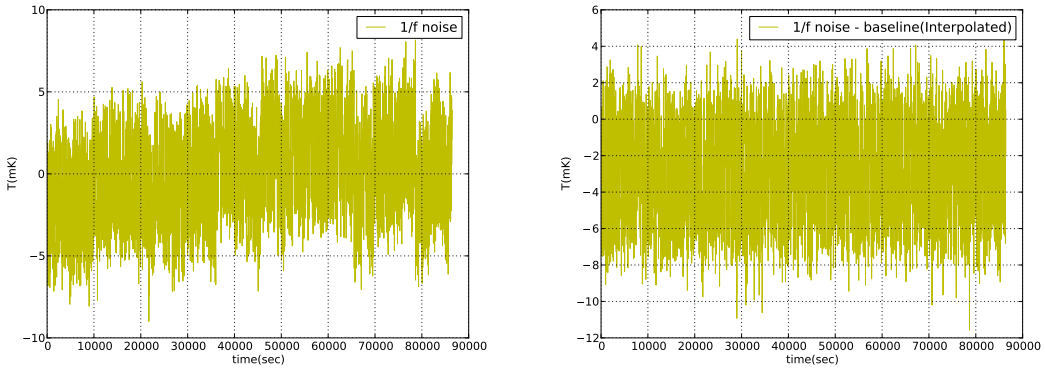

Figure 4.26: Time-ordered input 1/f noise in one day(left) and the 1/f noise after the baseline reduction(right).

The effectiveness of the baseline reduction depends on the size of the pole region. If a smaller area is taken as a pole region, the signal fluctuaion from the white noise still remains, although the fluctuaion in the pole region is small. On the other hand, if a larger area is taken as a pole region, the signal fluctuaion in the pole region become larger, while the fluctuation from the white noise becomes smaller by $\sigma_{wnoise} = 5(\mathrm{mK})/\sqrt{\mathrm{N}}$. We will check this effect by changing the radius of the pole region away from 3°.

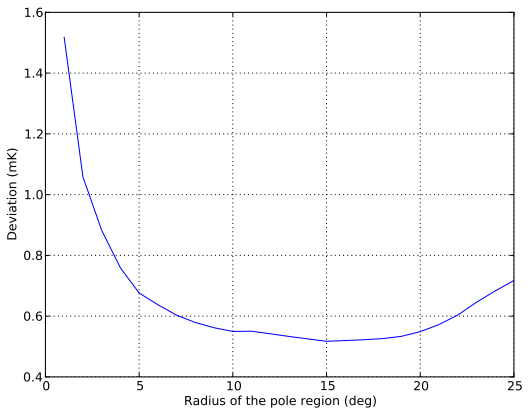

Figure 4.27: RMS deviation between the baseline from the raw data and the one from the input 1/f noise.

Fig. 4.27 shows that the rms deviation between the baseline from the raw data and the one from the input 1/f noise is minimized when the pole region is about 15°. The reduction of the white noise outweighs the increasing fluctuation in the pole region. However, when the radius is set larger than 15°, the fluctuation in the pole region gets larger and it affects our assumption that the temperature in the celestial pole region is constant.

We set the best value of the pole radius as 15° and apply the baseline reduction to the 1/f noise map (Fig. 4.22). The left panel of Fig. 4.28 is the residual map. The pattern of the original

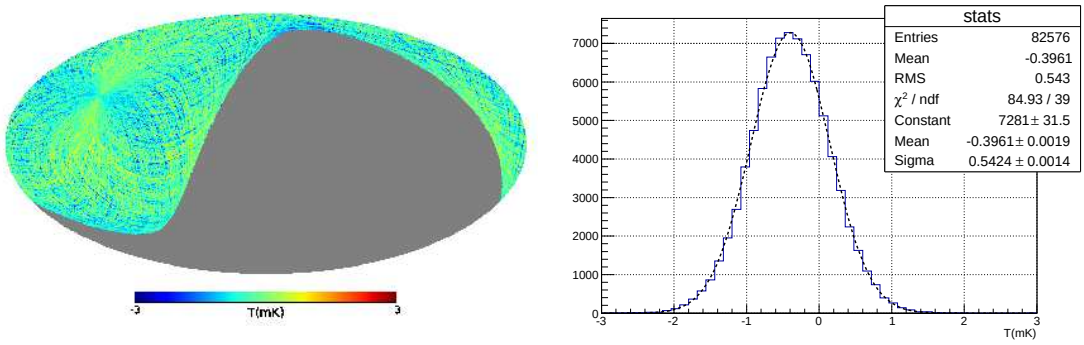

Figure 4.28: Residual map and histogram.

1/f noise map almost dissapears and the distribution of the residual amplitude has a random gaussian distribution, though the baseline is shifted ~ 0.4 (mK) by the polar signal subtracted from the data. This changes the zero-point of the map, but does not affect structure in the map and can be accounted for in subsequent analysis.

It is possible to reduce the correlation from the 1/f noise more by rotating the telescope faster than once per minute so that the telescope passes through the pole region more often. However, it also means that the interval of data taking has to be less, and it make the data rate larger. This will be an open trade as the instrument gets fielded.

4.5 Fitting CMB and galactic emissions

In this section, we evaluate the ability of a 10 GHz survey in separating galactic signals from CMB signals. We do so by combining this data with the Haslam and WMAP data, and compare results with and without the 10 GHz data.

4.5.1 Simulated sky maps at 7 bands

Here, we simulate 7 band maps by

$$T_{model}(\nu,p) = T_s(p) * \left(\frac{\nu}{0.408}\right)^{\beta_s(p)} + T_{ff}(p) * \left(\frac{\nu}{23}\right)^{-2.15} + T_d(p) * \left(\frac{\nu}{94}\right)^{1.8} + T_{CMB}(p), \tag{4.22}$$

where $\nu = 0.408, 10, 23, 33, 41, 61$ and 94 (GHz) as seen in Fig. 4.29.

4.5.2 Fitting data without noise

First, we attempt to extract CMB and 4 other galactic emissons using the 7-band maps without noise. To separate each emission from the sum, we fit each pixel to a model of the form given in Eq. 4.23. We use the Levenberg-Marquardt algorithm (LMA) in the Python implementation (scipy.optimize.leastsq) to perform a nonlinear least-square fit to the data. The routine returns the optimized values for a given model function with variables.

The model function has the same form as the input data,

$$y(x) = p_0 * \left(\frac{x}{0.408}\right)^{p_1} + p_2 * \left(\frac{x}{23}\right)^{-2.15} + p_3 * \left(\frac{x}{94}\right)^{1.8} + p_4, \tag{4.23}$$

where p_i is parameters to be optimized by "leastsq" function, y(x) is raw data at each frequency, x = (0.408, 10, 23, 33, 41, 61, 94)[GHz] in case of 7-band data and x = (0.408, 23, 33, 41, 61,

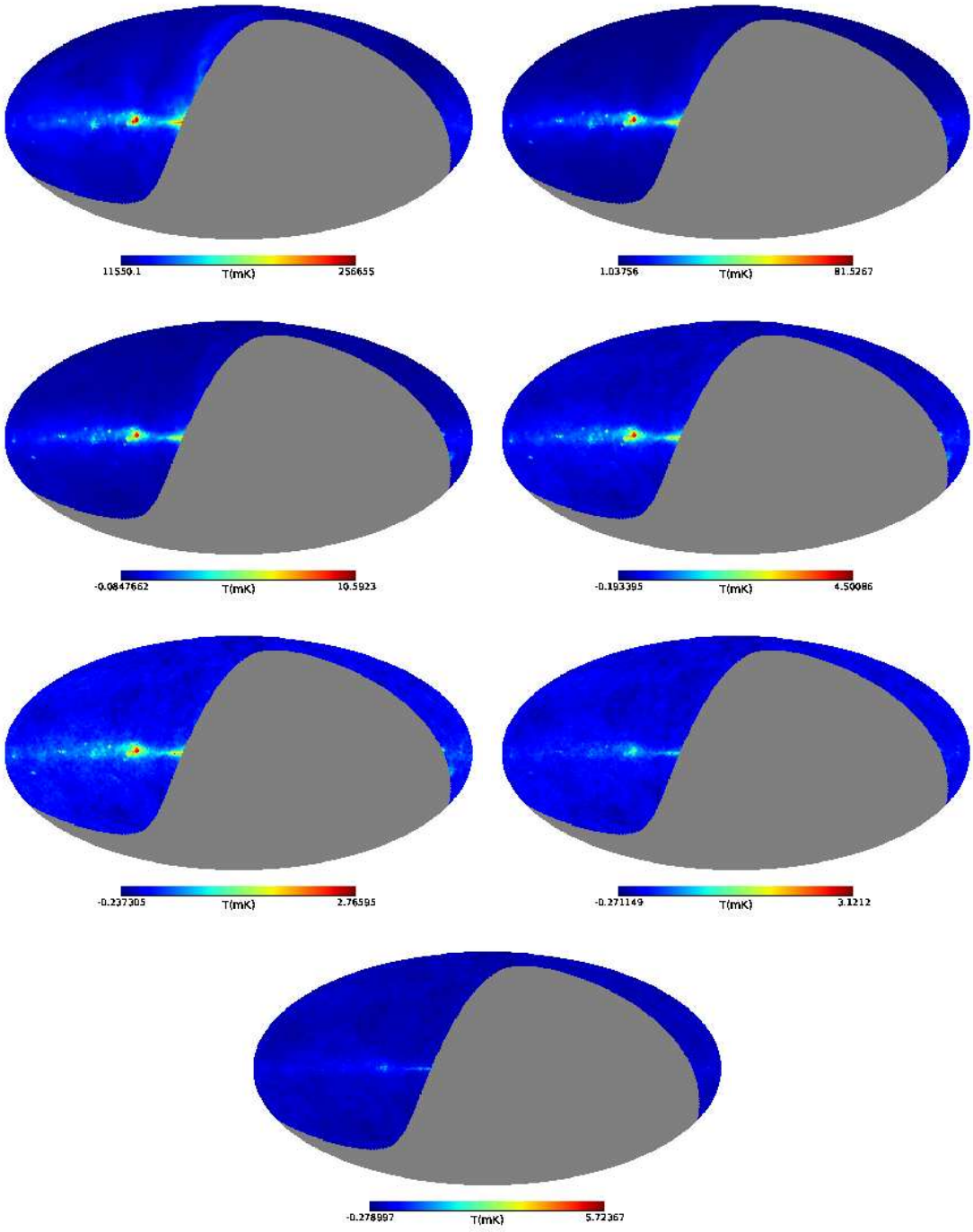

Figure 4.29: Simulated 7 band maps. (left top: 0.408 GHz, left middle: 10 GHz, left bottom: 23 GHz, right top: 33 GHz, right middle: 41 GHz, right bottom: 61 GHz, bottom: 94 GHz)

94)[GHz] in case of 6-band data (where we omit the 10 GHz channel). For the fitting, we use one initial value for all the pixels as in Tab. 4.3.

	p_0	p_1	p_2	p_3	p_4
Initial value	200000.0	-2.7	0.1	0.01	0.1

Table 4.3: Initial value for fitting.

Tab. 4.4 gives the true values and fit values for the 7-band and 6-band fitting. Fig. 4.30 shows the comparison between the spectrum with the true values and best fit values. In both cases, the input values are correctly recovered for all the pixels,

	p_0	p_1	p_2	p_3	p_4
True value	1.510e+04	-2.921e+00	2.425e-03	5.558e-04	9.914e-02
Fit value (7-band)	1.510e+04	-2.921e+00	2.425e-03	5.558e-04	9.914e-02
Fit value (6-band)	1.510e+04	-2.921e+00	2.425e-03	5.558e-04	9.914e-02

Table 4.4: True values and fit values by 7-band and 6-band fitting at a selected pixel (without noise). The residual error in all pixels is consistent with numerical noise.

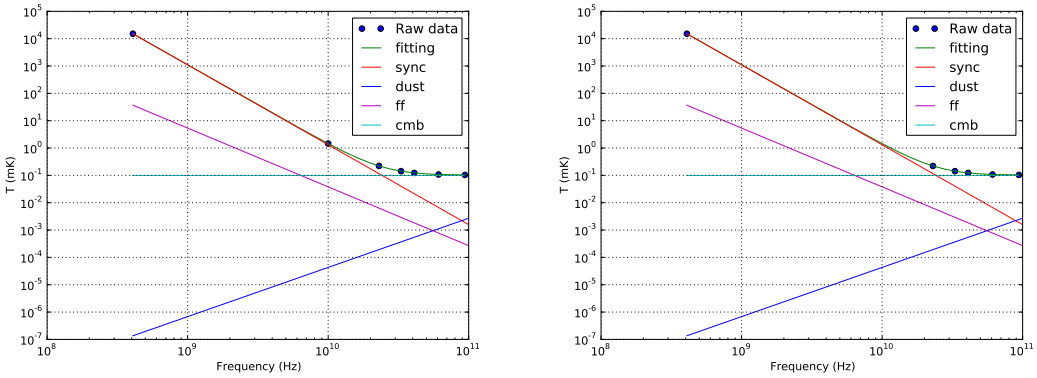

Figure 4.30: Raw data and Spectrum with fit values from data without noise. (Left: 7-band data case, right: 6-band data case. Data point: input data, green: total emission, red: synchrotron, purple: free-free, blue: thermal dust, cyan: CMB. Solid line: spectrum with true parameters, dashed line: spectrum with fit values. All the dashed lines can not be seen because the fit values match with the input values.)

4.5.3 Adding noise

We next add noise to the raw data and attempt to extract CMB and 4 other galactic emissons using the same procedure.

For the WMAP data, the noise amplitude for each frequency is provided in the LAMBDA website (http://lambda.gsfc.nasa.gov/product/map/dr4/skymap_info.cfm) as shown in Tab. 4.5. The pixel noise is $\sigma = \sigma_0/\sqrt{N_{obs}}$, where σ_0 is the noise per observation and N_{obs} is the number of observations per pixel. We add the noise to the WMAP maps using the random number generator, $N(0,1) * \sigma_0/\sqrt{N_{obs}}$.

Frequency (GHz)	23	33	41	61	94
Pixel noise(σ_0) (mK)	1.437	1.470	2.197	3.137	6.549

Table 4.5: Pixel noise of WMAP data (LAMBDA).

For the Haslam data at 0.408 GHz, we do not have the correct noise amplitude, but assume $\sigma_0 = 100$(mK) and $N_{obs} = 1$ for all the pixels. For the 10 GHz data, we assumed $\sigma_0 = 5$(mK) and N_{obs} is obtained from the hit map in Fig. 4.3 scaled to 1 year of observations. We also add the noise to each map by $N(0,1) * \sigma_0/\sqrt{N_{obs}}$. Fig. 4.31 shows the noise maps produced by the above procedure.

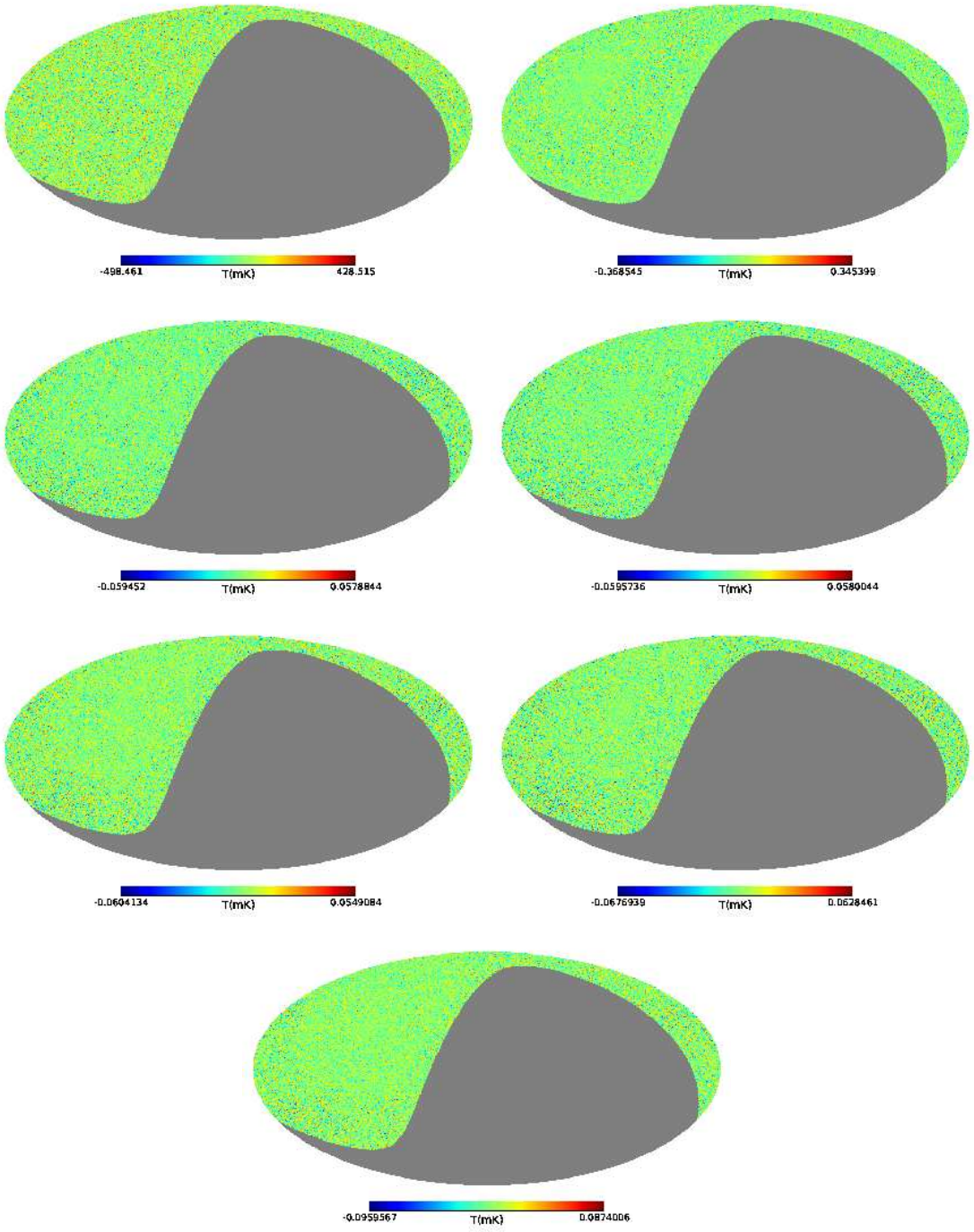

Figure 4.31: Simulated Noise maps at each frequency. (left top: 0.408 GHz, left middle: 10 GHz, left bottom: 23 GHz, right top: 33 GHz, right middle: 41 GHz, right bottom: 61 GHz, bottom: 94 GHz)

4.5.4 Fitting data with noise

Next, we attempt to extract CMB and 4 other galactic emissons from the data including noise. Here, the maps are produced by

$$T_{model}(\nu, p) = T_s(p) * \left(\frac{\nu}{0.408}\right)^{\beta_s(p)} + T_{ff}(p) * \left(\frac{\nu}{23}\right)^{-2.15} + T_d(p) * \left(\frac{\nu}{94}\right)^{1.8} + T_{CMB}(p) + T_{wnoise}(p), \tag{4.24}$$

where $\nu = 0.408, 10, 23, 33, 41, 61$ and 94 (GHz), with the model function,

$$y(x) = p_0 * \left(\frac{x}{0.408}\right)^{p_1} + p_2 * \left(\frac{x}{23}\right)^{-2.15} + p_3 * \left(\frac{x}{94}\right)^{1.8} + p_4. \tag{4.25}$$

where p_i is parameters to be optimized in the fitting process, y(x) is raw data at each frequency, x = (0.408, 10, 23, 33, 41, 61, 94)[GHz] in case of 7-band data and x = (0.408, 23, 33, 41, 61, 94)[GHz] in case of 6-band data. We use the same initial value as in Tab. 4.3.

Tab. 4.6 gives the input values and fit values for the 7-band and 6-band fitting. Fig. 4.32 compares the input and fit spectra, by component. The input values are not exactly obtained by the 7-band fitting for every pixel, but they are better for the 7-band fitting than for the 6-band fitting.

	p_0	p_1	p_2	p_3	p_4
True value	1.510e+04	-2.921e+00	2.425e-03	5.558e-04	9.914e-02
Fit value (7-band)	1.500e+04	-2.941e+00	3.383e-03	1.091e-03	9.590e-02
Fit value (6-band)	1.429e+04	-1.223e+01	1.876e-02	1.172e-02	7.731e-02

Table 4.6: Input and fit values from the 7-band and 6-band fitting (with noise).

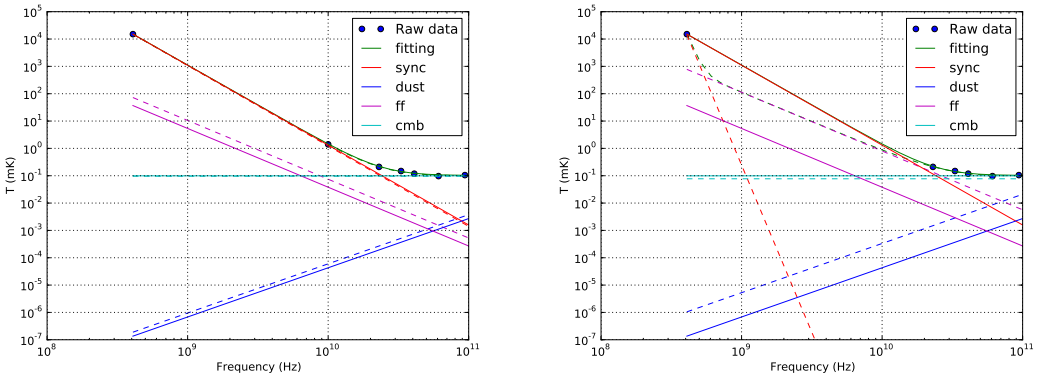

Figure 4.32: Input and recovered spectra obtained for data with noise in a selected pixel. (Left: 7-band data case, right: 6-band data case. Data point: raw data, green: total emission, red: synchrotron, purple: free-free, blue: thermal dust, cyan: CMB. Solid line: spectrum with true parameters, dashed line: spectrum with fit values.)

4.5.5 Covariance between different components

Fig. 4.33 shows the covariance between different parameters in the fit. The correlation is clearly seen in the 7-band fitting result. In higher frequencies, the main emissions are thermal dust and CMB emission, so lower T_{dust} leads to higher T_{cmb} in the fitting, which has a negative correlation. In lower frequencies, the main emissions are synchrotron and free-free emission, so lower T_{sync} leads to higher T_{ff}, which also has a negative correlation.

However, the correlation is distorted in the 6-band fit as shown in Fig. 4.34 because the fitting fails for some pixels as seen, for example, in the right panel of Fig. 4.32.

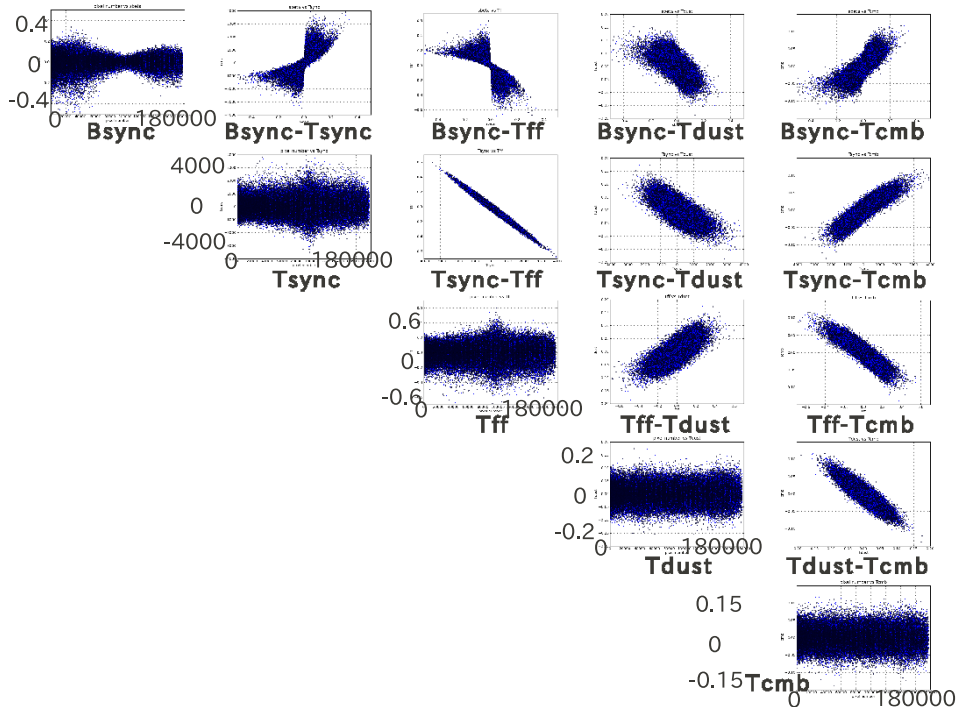

Figure 4.33: Correlation in 7-band fitting between each fit parameter.
The diagonal panels show Δp vs pixel number, where Δp is the fit paramter error (as indicated in the plot axes). The off-diagonal panels show the covariance between pair of parameter errors.

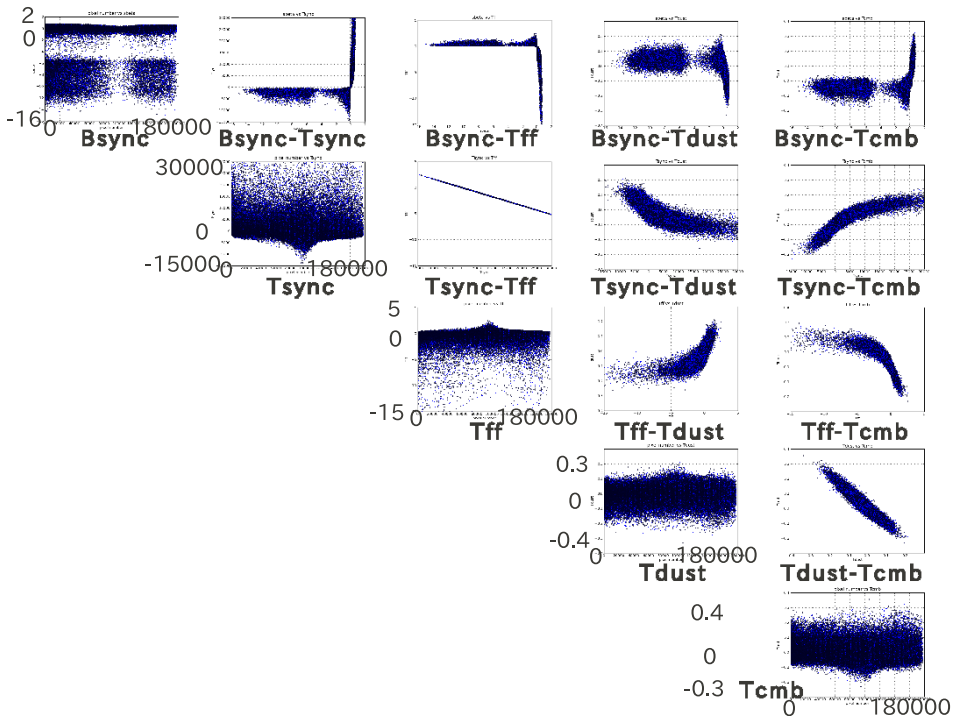

Figure 4.34: Correlation in 6-band fitting between each fit parameter.
The diagonal panels show Δp vs pixel number, where Δp is the fit paramter error (as indicated in the plot axes). The off-diagonal panels show the covariance between pair of parameter errors.

4.5.6 Output maps by component

We make output maps by using the paramters obtained by the fit, and compare the input map with the output maps in the case of 7-band and 6-band fitting. Fig. 4.35 - Fig. 4.37 show maps of synchrotron emission scaled to 94 GHz. Fig. 4.38 - Fig. 4.40 show free-free emission, Fig. 4.41 - Fig. 4.43 show thermal dust emission, and Fig. 4.44 - Fig. 4.46 show CMB all at 94 GHz.

Comparing Fig. 4.36 and Fig. 4.37, the output map by the 7-band fitting looks much better than the output map by the 6-band fitting. In detail, the rms of the residual map from 7-band fitting and 6-band fitting are summaried in Tab. 4.7. The 7-band data clearly has a better ability to extract each emission component than the 6-band data.

	STD of Input	RMS of Resi (7-band)	RMS of Resi (6-band)
Synchrotron	0.0139	0.0024	9.4455
Free-free	0.0081	0.0056	9.4492
Thermal dust	0.0774	0.0336	0.0579
CMB	0.0675	0.0260	0.0649

Table 4.7: Standard deviation of input map and residual maps for the 7-band and 6-band fits (unit is mK, frequency is 94 GHz).

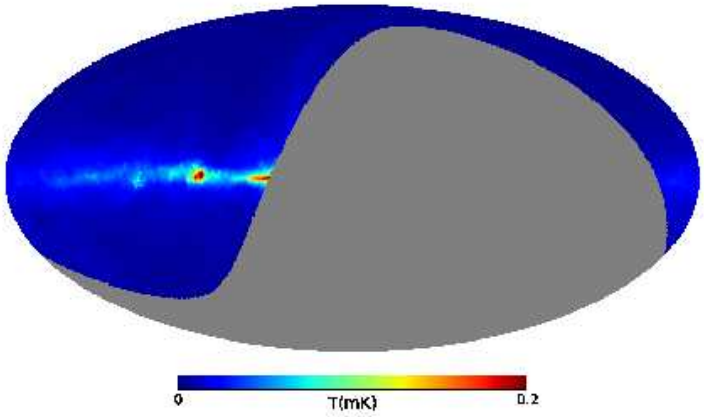

Figure 4.35: Input synchrotron map.

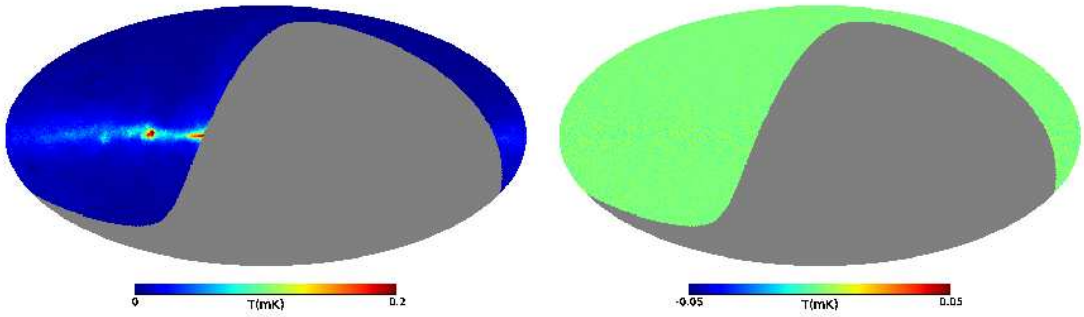

Figure 4.36: Output and residual synchrotron map from 7-band fitting.

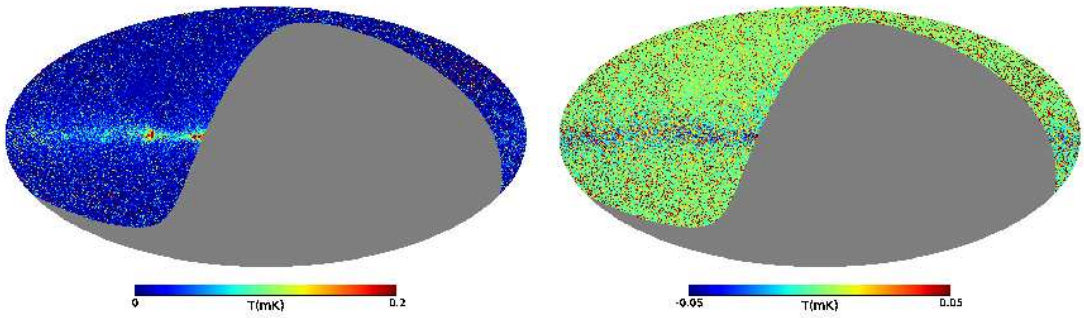

Figure 4.37: Output and residual synchrotron map from 6-band fitting.

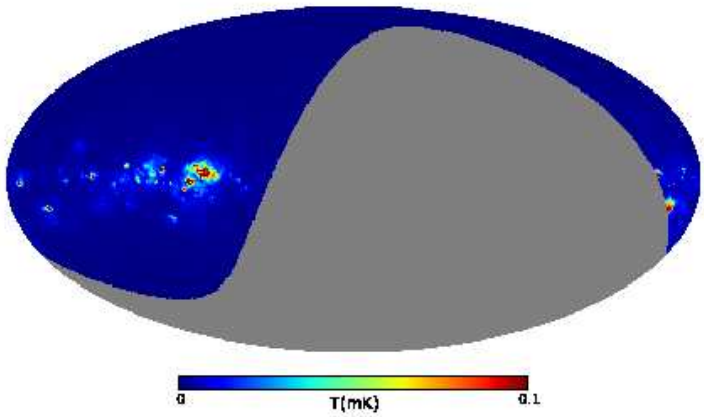

Figure 4.38: Input free-free map.

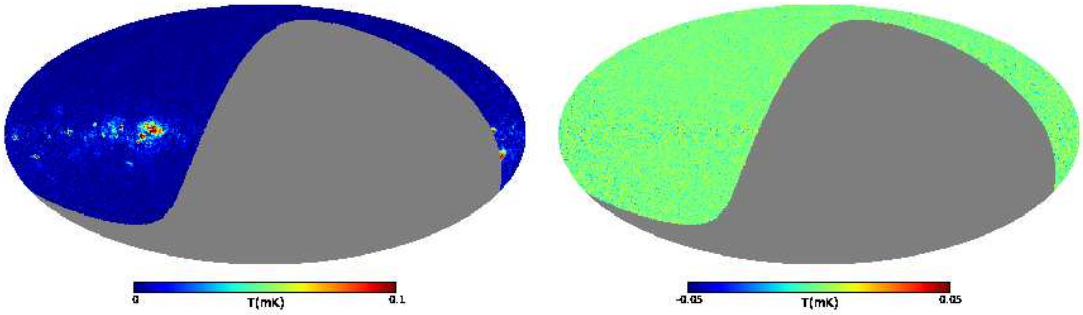

Figure 4.39: Output and residual free-free map from 7-band fitting.

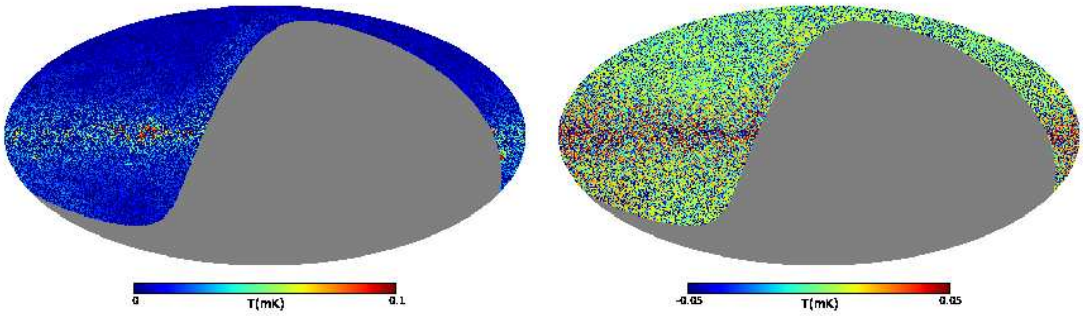

Figure 4.40: Output and residual free-free map from 6-band fitting.

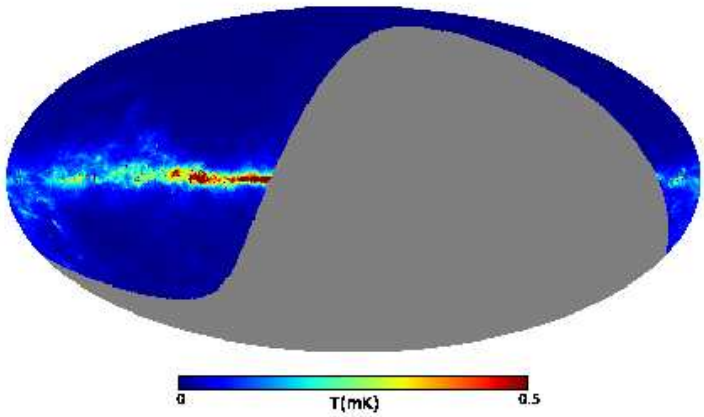

Figure 4.41: Input thermal dust map.

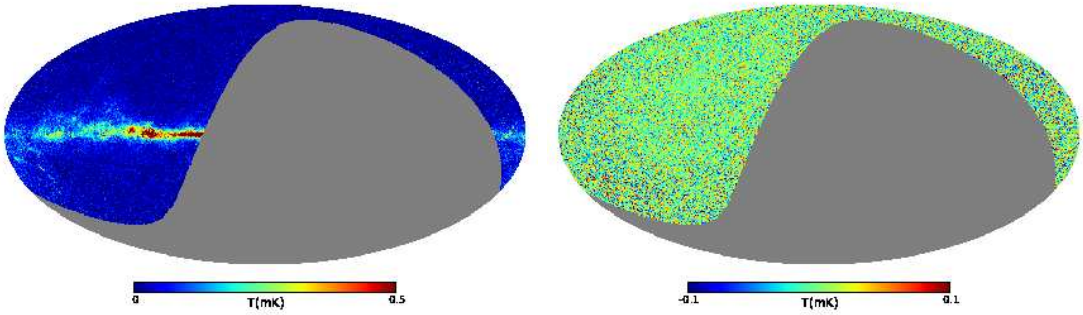

Figure 4.42: Output and residual thermal dust map from 7-band fitting.

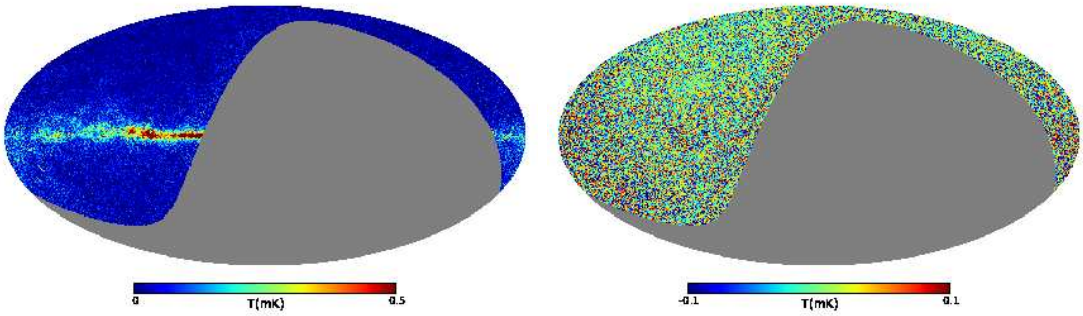

Figure 4.43: Output and residual thermal dust map from 6-band fitting.

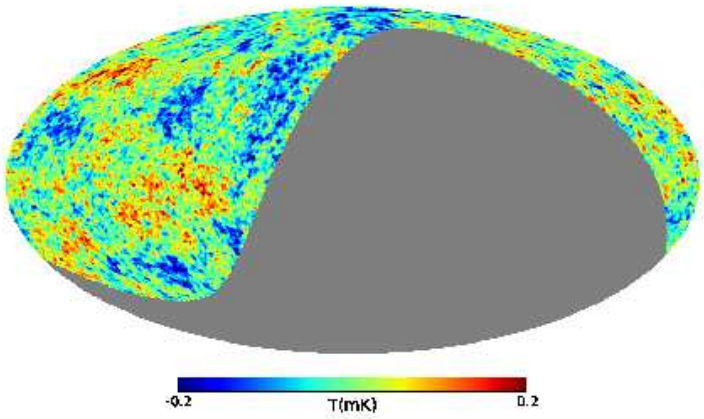

Figure 4.44: Input CMB map.

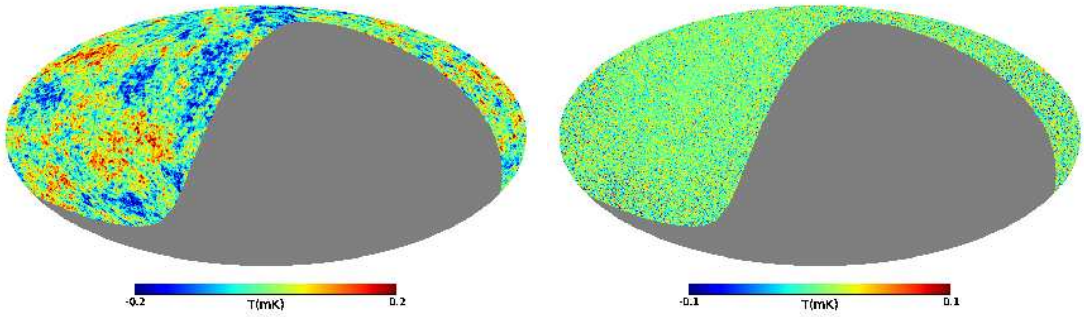

Figure 4.45: Output and residual CMB map from 7 band fitting.

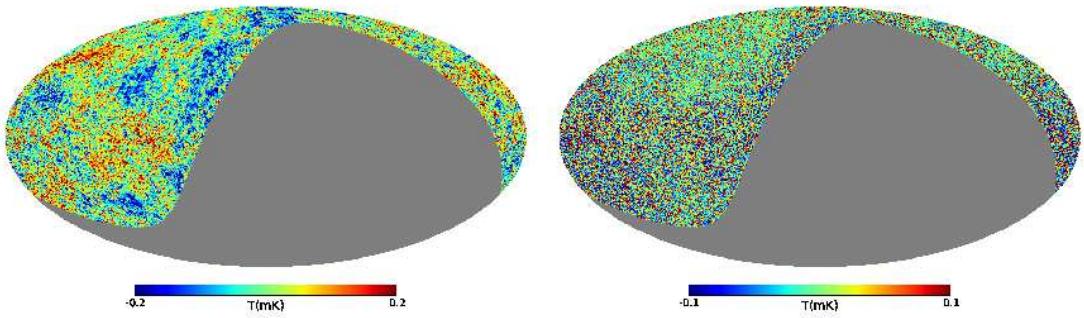

Figure 4.46: Output and residual CMB map from 6 band fitting.

Chapter 5

Conclusions

We simulate observations required for a 10 GHz sky survey with estimated noise appropriate to one year year observations at Penticton. We combine this with simulated maps at 408 MHz and the WMAP frequencies, where the input emission components are known. With these simulated maps, we fit for foreground emission and the CMB. For all of the components, the recovery is much better when 10 GHz data are included, which demonstrates the effectiveness of the 10 GHz data. In particular, it is found that 10 GHz data help to constrain synchrotron emission, which is the main component of foreground polarization, and the CMB is recovered with nearly 3 times better precision when 10 GHz data are included as shown in Tab. 4.7.

We did not include spinning dust emission in this simulation because it is a weak emission compared to the other foreground emissions. However, 10 GHz data also should be sensitive to the spinning dust emission. We are currently working on this task. The following is the list of the future work necessary to do before starting actual observations.

1. Simulations including spinning dust emission: In the theory, there are at least two degrees of freedom for the emission: the central position and the amplitude of the emission.

2. Polarization: The simulation here is focused on the temperature case. However, our goal is to detect B-mode polarization in CMB by subtracting the dominant polarized foreground emission. We need to analyze the sensitivity of foreground polarization subtraction, but the temperature results are generally applicable.

3. Optimization of hardware: The rotation speed of the telescope and the data collection interval are related to the noise reduction. If the speed is set higher and the data interval is set lower, we can de-stripe the 1/f noise more effectively. However, it makes the telescope more difficult.

4. Sensitivity to B-mode polarization: Our goal is to detect B-mode polarization in CMB at the level of r=0.01 in the tensor-to-scalar ratio. We need to determine the noise level required (and hence intergration time required).

After checking all of these, we will develop actual instrumentation. There are similar experiments trying to detect B-mode polariztion in CMB, but our experiment is much simpler where the signal is stronger than other experiments. Because our goal is aimed at lower frequency, for the 10 GHz data to be useful in combination with higher frequency data from other experiments, this experiment will help advance cosmology.

Bibliography

Ali-Haimoud, Y., et al. 2009, *Monthly Notices Roy. Astron. Soc.*, 395, 1055

Baumann, D., et al. 2009, arXiv:0811.3919

Bennett, C. L., et al. 2003, *Astrophys. J. Suppl.*, 148, 97

Bennett, C. L., et al. 2012, arXiv:1212.5225

Burles, S. & Nollett, K. M. & Turner, M. S. 1999, astro-ph/9903300

Dickey, J. M. & Lockman, F. J. 1990 *Ann. Rev. Astron. Astrophys.*, 28, 115

S.Dodelson 2003, Modern Cosmology, Academic Press

Draine, B. T. & Lazarian, A. 1998 *Astrophys. J.*, 508, 157

Finkbeiner, D. P., Davis, M., & Schlegel, D. J. 1999, *Astrophys. J.*, 524, 867

Finkbeiner, D. P. 2003, *Astrophys. J. Suppl.*, 146, 407

Fixsen, D. J., et al. 2009, arXiv:0911.1955

Freedman, W. L. 2003, *Astrophys. J.*, 553, 47

Guth, A. H. 1981, *Phys. Rev. D.*, 23, 347

Hamuy, M., et al. 1995, *Astron. J.*, 109, 1

Hartmann, D., et al. 1996, *Astron. Astrophys. Suppl.*, 119, 115

Hartmann & Burton 1997, Cambridge University Press

Haslam, C. G. T., et al. 1981, *Astron. Astrophys.*, 100, 209

Hinshaw, G., et al. 2012, arXiv:1212.5226

Hiranya, V. P. cosmology course text, *Cosmology Part II: The Perturbed Universe*, University College London, UK

Hu, W., et al. 1996, *Astrophys. J.*, 471, 30

Hu, W., et al. 1997, arXiv:astro-ph/9706147

Hu, W. & Dodelson, S., et al. 2002, *Ann. Rev. Astron. Astrophys.*, 40, 171

Hubble, E. P., et al. 1929, *Publ. Nat. Acad. Sci.*, 15, 168

Kamionkowski, M. & Kosowsky, A., et al. 1999, *Ann. Rev. Nucl. Part. Sci.*, 49, 77

LIGO Scientific Collaboration & Virgo Collaboration. 2009, *Nature*, 460:990994

Linde, A. D., 1983, *Phys. Lett.*, B129, 177

Mather, J. C., et al. 1994, *Astrophys. J.*, 420, 439

McAllister, A., 2010, *Phys. Rev. D.*, 82, 046003

Page, L., et al. 2007, *Astrophys. J. Suppl.*:170, 335

Paolo de Bernardis et al. 2009, arXiv:0808.1881

Perlmutter, S., et al. 1999, *Astrophys. J.*, 517, 565

S. Perlmutter & B. Schmidt 2003 *in Supernovae and Gamma Ray Bursters*, K. Weiler, ed., Springer-Verlag, New York

Planck Collaboration. 2011, *Astron. Astrophys.*, 536, A19

Platania, P., et al. 1998, *Astrophys. J.*, 505, 473

Riess, A. G., et al. 1998, *Astron. J.*, 116, 1009

Roger, R. S., et al. 1999, *Astron. Astrophys. Suppl.*, 137, 7

Rybicki, G. B. & Linghtman, A. P. 1979, *Radiative Processed in Astrophysics*, Wiley-interscience, New York

Sarkar, S., et al. 2006, *Phys. J.*, G31, 1

Schlegel, D. J., et al. 1998, *Astrophys. J.*, 500, 525

Scott, B. & Smoot, G. 2004 *Phys. Lett.*, B592, 1

Silsbee, K., et al. 2011, *Monthly Notices Roy. Astron. Soc.*, 411, 2750

Spergel, D. N., et al. 2003, *Astrophys. J. Suppl.*, 148, 1755

Starobinsky, A. A., et al. 1980, *Phys. Lett.*B, 91, 99

Tibbs, C. T., et al. 2012, arXiv:1212.3269

Watson, G. S., et al. 2000, arXiv:astro-ph/0005003

Watson, R. A., et al. 2005, *Astrophys. J.*, 624, L89